THE g-FACTOR OF THE $19/2^-$ STATE in ^{115}Sb AND HIGH SPIN STRUCTURE OF ^{180}W

By

Steven Ray Faber

AN ABSTRACT OF A DISSERTATION

Submitted to

Michigan State University

in partial fulfillment of the requirements

for the degree of

DOCTOR OF PHILOSOPHY

Department of Chemistry

1979

ABSTRACT

THE g-FACTOR OF THE $19/2^-$ STATE IN ^{115}Sb AND HIGH SPIN STRUCTURE OF ^{180}W

By

Steven Ray Faber

A magnet for measuring g-factors by the time differential perturbed angular distribution (TDPAD) technique has been constructed. It was used to measure the g-factor of the $19/2^-$ state in ^{115}Sb by means of the $^{115}In(\alpha,4n\gamma)^{115}Sb$ reaction. The measured value confirmed the suspected $\{\pi d_{5/2} \otimes \nu h_{11/2} \otimes \nu d_{3/2}\}$ configuration. The effect of core polarization is discussed in relation to the measured value ($g = 0.287(4)$). The g-factor of the $11/2^-$ state was obtained as a by-product and was found to be 1.06(10).

The g-factor of the 12^+ state in ^{202}Pb was also measured using a liquid Hg target in a $Hg(\alpha,xn)^{199-204}Pb$ experiment with a 48 MeV α beam. The g-factor was found to be $g = -0.14(2)$, consistent with the suspected $(i_{13/2})_n^{-2}$ configuration. The $21/2^+$ state of ^{203}Pb was shown to have a positive g-factor contrary to what was expected.

Steven Ray Faber

The high spin structure of ^{180}W was studied by means of the $^{180}Hf(\alpha,4n)^{180}W$ reaction. Three 4-quasiparticle isomers were discovered ($K^{\pi} = 14^{-}$, 15^{+} and 16^{+}) consistent with configurations and spin assignments from calculated Nilsson orbitals. Four rotational bands have been identified based on $K^{\pi} = 2^{-}$, 8^{-}, $5^{(-)}$, and 16^{+} isomers. The configurations of these are determined from branching ratios and angular distribution data. The perturbed nature of the ground band and $K^{\pi} = 2^{-}$ band is discussed in terms of Coriolis interactions.

THE g-FACTOR OF THE $19/2^-$ STATE in ^{115}Sb AND HIGH SPIN STRUCTURE OF ^{180}W

By

Steven Ray Faber

A DISSERTATION

Submitted to

Michigan State University

in partial fulfillment of the requirements

for the degree of

DOCTOR OF PHILOSOPHY

Department of Chemistry

1979

ACKNOWLEDGMENTS

I would like to thank most of all my Advisor, Fred Bernthal, for all his help and keen insight in suggesting these research projects, as well as for his friendship and support during my stay.

Special thanks to T. L. Khoo, L. E. Young, P. Walker, C. Dors, and R. Warner, for their help in experiments and for teaching me much of what I have learned. Thanks also to office mates, W. Bentley and P. Deason for the same.

Thanks to C. Morgan and B. Jeltema for their programming help and M. Edmiston and B. Melin for their expertise; and all four for their help in "special effects" at the lab.

Thanks to all members of Nuclear Beer, especially Patricia who managed our wedding at the same time I managed this thesis.

Acknowledgments also go to P. Miller, H. Hilbert, N. Mercer, B. Welton, and H. Blosser for their help in obtaining and constructing equipment including help with the cyclotron.

I also wish to thank P. Warstler for typing this thesis and the N.S.F. for financial support.

TABLE OF CONTENTS

Chapter

Page

LIST OF TABLES

LIST OF FIGURES

PART 1

g-FACTORS

I. INTRODUCTION

One of the goals of nuclear physics is to learn about the structure of nuclei and determine an appropriate model to explain the observed energy levels and transitions. Ideally all the properties of an excited state should be predictable from the wavefunction of the state, the wavefunction being a not too complicated mixture of convenient basis states. The energy and static moments of a level practically determine the wavefunction and many properties of the system such as the decay transition rates. The measurement of the magnetic dipole moment of nuclear energy levels is and has been of value in determining the validity of nuclear models such as the shell model, since it is very sensitive to impurity configurations and can be accurately measured in many cases. For this reason many measurements have been done near closed shells where impurity admixtures are low. There are many instances, however, where the magnetic moment measurement of a level would be of value in determining its configuration, particularly if one needs only to omit certain possibilities from a list of possible configurations. This makes magnetic moment or g-factor ($\vec{\mu} = g\vec{J}$) measurements of value even on deformed nuclei. There

are many new isomers that have been found by the MSU and Purdue collaboration in W, Pt, Hg and Pb nuclei that were accessible through in-beam (α,xn) reactions [He77], [Sa77], [Pt75].

The method of perturbed angular distributions is particularly suited for in-beam measurements, so this method was chosen for use with the MSU cyclotron. A magnet for measuring g-factors was constructed and the results of some measurements are discussed in the following sections.

II. THEORY

2.1. Shell Model

In the simplest model, the single particle shell model, the nucleus is viewed as a collection of paired nucleons with only the last unpaired nucleon contributing to the magnetic moment of the nucleus. The spin and orbital angular momentum of each pair of nucleons is coupled to zero. The odd particle has spin angular momentum $\vec{s}$ and orbital angular momentum $\vec{\ell}$ that couple to total angular momentum $\vec{J}$. The respective angular momentum components $\vec{\mu}_\ell$, $\vec{\mu}_s$ of the total magnetic moment $\vec{\mu}_T$ are related to the angular momentum by the following equations that define the g factors $\vec{\mu}_\ell = g_\ell \vec{\ell}$, $\vec{\mu}_s = g_s \vec{s}$, and $\vec{\mu}_T = g\vec{J}$. g-Factors are given in units of the nuclear magnetons

$$\mu_N = \frac{e\hbar}{2M_n c} \qquad (1)$$

Classically for a particle charge e, mass m, velocity v, traveling in an orbit radius r, the current $i = \frac{e}{c\tau}$ where

τ is the period of rotation

$$i = \frac{e}{c\tau} = \frac{e}{c\,\frac{2\pi r}{v}} = \frac{ev}{c2\pi r}$$

The magnetic moment

$$\mu = iA = \frac{ev}{c2\pi r}\,\pi r^2 = \frac{evr}{2c}$$

$$|\vec{L}| = |\vec{r}x\vec{p}| = rmv$$

the magnitude of $\mu = \frac{eL}{2mc}$. It follows then for a quantum mechanical system that

$$L_z = m_\ell \hbar \text{ and } \mu_z = \frac{m_\ell}{2mc}\,.$$

The magnetic moment is defined in terms of the largest magnetic substate so we obtain the defining equation

$$\mu_L = gL\,\frac{\mu_N}{\hbar}$$

where g = 1 for the orbital component of the magnetic moment. Elementary particles also have a spin component associated with them giving μ_s. Table 2-1 gives the g-factors for the proton, neutron and electron, and the theoretical predictions by relativistic Dirac theory. Note that the electron and positron are accurately predicted but the magnetic moment of the proton and neutron are quite different than expected. This is due presumably because the proton and neutron are not fundamental particles but are composed of quarks or at least mesons. Quark and meson exchange effects are discussed later.

Now let us consider some odd A nucleus and assume that our nucleons are nicely paired in their respective shell model orbits. The magnetic-moment of the nucleus taken as a first approximation to be that due to the free odd nucleon, the paired up "core" nucleons contributing nothing. The total magnetic moment of the nucleus will be the vector sum of the orbital moment μ_ℓ and the spin moment μ_s of the particle.

It is useful to have an equation for the sum of two magnetic moment vectors. If $\vec{\mu}_1 = g_1\vec{j}_1$, and $\vec{\mu}_2 = g_2\vec{j}_2$, $\vec{\mu}_J = g\vec{J} = (\vec{\mu}_1 + \vec{\mu}_2)\cdot\frac{\vec{J}}{|\vec{J}|}$ where $\vec{J} = \vec{j}_1 + \vec{j}_2$. $\vec{\mu}_J$ is the sum of the projection of μ_1 and μ_2 on J.

$$\vec{\mu}_J = g\vec{J} = \frac{g_1(\vec{j}_1\cdot\vec{J})\vec{J}}{J^2} + \frac{g_2(\vec{j}_2\cdot\vec{J})\vec{J}}{J^2}$$

Table 2-1. g-factors of Elementary Particles.

	Proton	Neutron	Electron
g_ℓ	1	0	-1
Experimental g_s	5.586	-3.826	-2
Theory g_s	2	0	-2

Substituting $J^2 = j_1^2 + j_2^2 + 2\vec{j}_1 \cdot \vec{j}_2$ and simplifying we obtain the generalized Landé formula

$$g_J = \frac{g_1+g_2}{2} + \frac{(g_1-g_2)j_1(j_1+1) + (g_2-g_1)j_2(j_2+1)}{2J(J+1)} \qquad (3)$$

If we substitute $\ell = j_1$, $s = j_2$, $g_1 = g_\ell$, $g_2 = g_s$, we obtain an expression for g_J the g-factor of the nucleus of spin $J = \ell \pm \frac{1}{2}$. This is the Schmidt estimate [Sc37].

$$g = g_\ell \pm \frac{g_s-g_\ell}{2\ell+1} \, . \qquad (4)$$

If one plots μ as a function of J, $J = \ell \pm \frac{1}{2}$, one obtains the so called Schmidt lines. Most of the magnetic moments of the ground state of odd A nuclei fall between these lines suggesting a "quenched" g_s value is more appropriate for a nucleon in a nucleus over that for a free nucleon. The general trend is predicted well, however, and the Schmidt formula is useful in predicting g-factors of certain configurations roughly, especially near closed shells where perturbations are smaller.

2.2. Core Polarization and Configuration Mixing

In most cases the largest error in the single particle shell model estimate for magnetic moments is the assumption that the single particle has no effect on the core. The odd particle can "polarize" the core, however, or induce excitation in the core of the type $(j_1^{-1}, j_2)I_c = 1$ where $j_1 = \ell + \frac{1}{2}$, $j_2 = \ell - \frac{1}{2}$. In other words there is a nonzero matrix element connecting the ground core state $I_c = 0$ and an excited $I_c = 1$ core state. Figure 2-1a shows shell model levels near closed shells, and possible core excitations. Note that near the N = 8 and N = 20, ^{16}O, ^{40}Ca closed shells the orbitals available are not of the same ℓ and therefore no core polarization can occur, but near the N = 50, 80, Sn + ^{208}Pb closed shells the orbitals are available and core polarization can occur. It is for this reason that the heavier elements deviate more from the Schmidt lines than the lighter elements near ^{16}O + ^{40}Ca. The sign of the core polarization magnetic moment correction is such that it accounts for the inward deviation from the Schmidt lines. A simplified explanation of core polarization can be given which predicts the lowering of the magnetic moment. Assume a proton is traveling around a nuclear core (Figure 2-1b), spin direction as shown. The core protons will want to align antiparallel and the neutrons parallel since like nucleons prefer a singlet state and

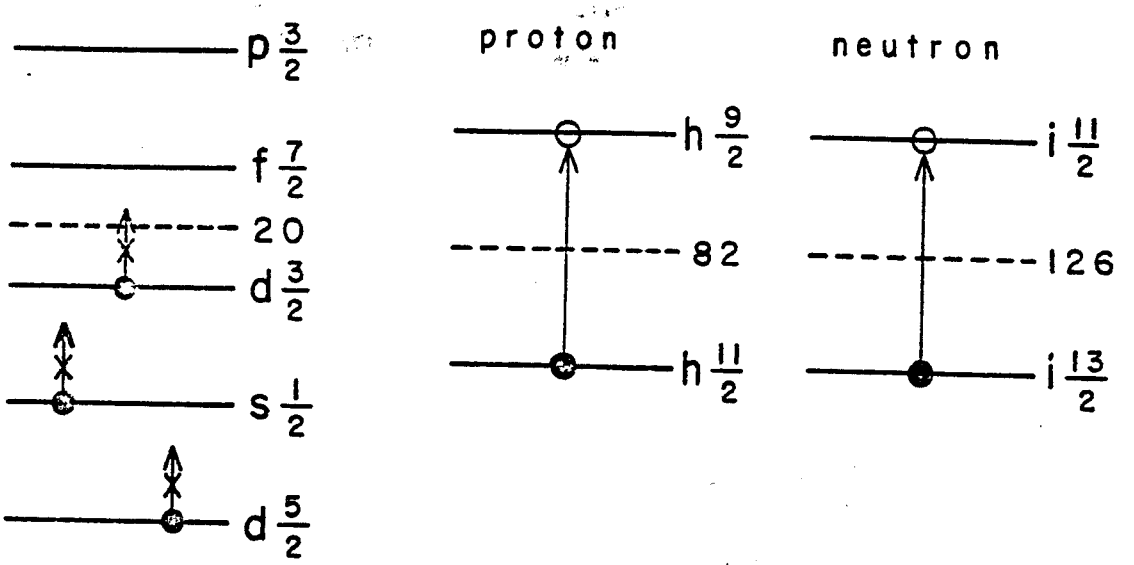

Figure 2-1a. Core polarization excitations near closed shells.

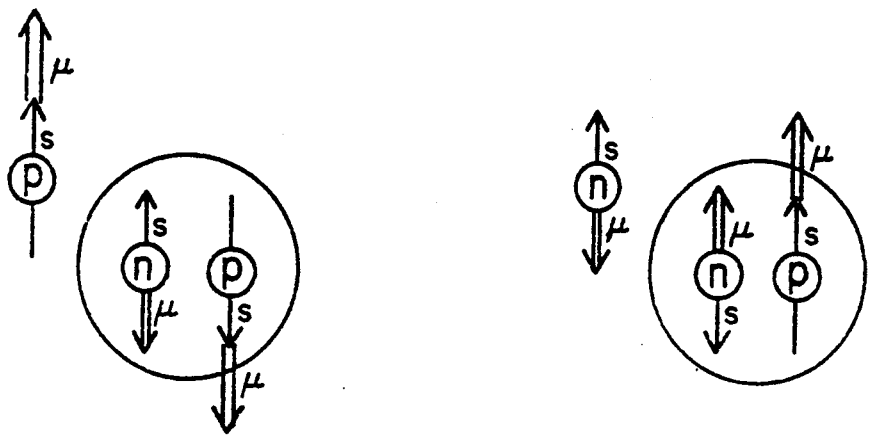

Figure 2-1b. Core polarization and spin alignment.

unlike nucleons a triplet state. The result is the generation of an oppositely oriented core magnetic moment from both core neutrons and protons since the direction of $\vec{\mu}$ is opposite the spin for a neutron.

Core polarization is just another name for configuration mixing though, since the admixture of these core excited states to the wavefunction as mentioned before is core polarization. Arima and Horie have done calculations to estimate the first order core polarization correction $\delta\mu_{1st}$ [Ar54],[No58]. The value depends on the spin and occupation numbers of the orbitals involved as well as the energy gap between orbitals, the radial integrals of the wavefunctions and the strength of triplet and singlet nucleon-nucleon interaction. Some simple assumptions have been made such as $|V_t| = 1.5|V_s|$ that allow one to easily estimate with reasonable accuracy the $\delta\mu_{1st}$ [Ar54].

2.3. Higher Order Effects

If one considers some single particle wavefunction ψ as a mixture of ψ° shell model states and α_i amounts of some impurity states ψ_i, one could write the wavefunction as

$$\psi = \sqrt{1-\Sigma\alpha_i^2}\,\psi^{\circ}_{(j,I_c=0)} + \sum_i \alpha_i \psi^i(j,I_c) \qquad (5)$$

[Mo76] where ψ^i can contain the appropriate $I_c = 1$ $\delta_{\mu lst}$ components. We could then write

$$\mu = (1-\Sigma_i|\alpha_i|^2)\mu_{sp} + \delta_{\mu lst} + \Sigma_i \alpha_i^2 \mu_i$$

where μ_{sp} is the single particle estimate and μ_i is the magnetic moment of impurity state i. If we consider the μ_i's as being due to random excitations of the core causing an average magnetic moment $\mu_R = j \cdot gR$ we can write the last term as $\mu_R \sum_i \alpha_i^2$. This random magnetic moment μ_R is also referred to as the rotational magnetic moment or rotational g-factor g_R and is expected to obey the following relation $g_R \approx \frac{Z}{A}$. We then have

$$\mu = \mu_{sp} + \delta_{\mu lst} - (\mu_{sp}-\mu_R)\Sigma\alpha_i^2 \qquad (6)$$

The third term is called the higher order correction $\delta_{\mu HO}$. The effect of $\delta_{\mu HO}$ is the same as if the g_ℓ factor in the Schmidt formula were reduced for the proton and increased for the neutron. Calculations of this are complicated and show that it is not always small.

Sometimes $\delta_{\mu HO}$ tends to cancel $\delta_{\mu lst}$. Some theories [Mi64] take care of $\delta_{\mu HO}$ by way of "renormalized operators" which assume some δg_ℓ caused by a nucleon-nucleon interaction time [Be68].

2.4. Quarks and Mesonic Effects

It isn't too surprising that the magnetic moments of isolated neutrons and protons don't match those predicted for Dirac particles, since these nucleons are considered to be composed of quarks and, more assurably, contain mesons as exchange particles as these equations demonstrate:

$$p \rightleftarrows n + \pi^+$$
$$n \rightleftarrows p + \pi^-$$

Since the π meson has no spin the magnetic moment is due to the orbital part ($\ell_\pi = 1$). The π meson being lighter than p or n will give rise to a higher moment

(formula 1) so by simple calculation a dissociation probability of ∿30% will reproduce the observed free nucleon moments. This value is consistent to the expected theoretical dissociation probability calculated from the pion-nucleon interaction [Mi56].

A more elegant and simple theory claims that nucleons are made of three quarks, a combination of "up" quarks charge + $\frac{2}{3}$ and "down" quarks charge - $\frac{1}{3}$. A proton is ↑↑↓ and a neutron is ↓↓↑. Quarks are spin 1/2 fermions with a Dirac g-factor. Assuming the ↑↑ and ↓↓ pairs couple to spin 1, we find by using the Landé formula (Equation 3) and the definition of nuclear magneton (Equation 1) that the g-factors are:

$$g_p = 2\frac{M_n}{M_q} \qquad g_n = -\frac{4}{3}\frac{M_n}{M_q} .$$

Since the mass of the quarks haven't been measured, the g-factors of the nucleons can't be predicted, but the ratio $\frac{g_p}{g_n} = -1.5$ is close to the measured $\frac{g_{p(free)}}{g_{n(free)}} = -1.46$. Also if one assumes $M_q \approx \frac{1}{3} M_n$ the g-factors are predicted quite accurately.

2.5. g-Factors and the Rotational Model

In the rotational model the nucleus is viewed as being deformed and rotating. The deformation thus introduced remove the degeneracies of the shell model orbits yielding orbitals designated by a new quantum number K, the projection of the spin on the symmetry axis. (See Section 6.1 and Figure 6-1 for a more extensive explanation.) Particles residing in these orbitals in excited states couple together under the influence of pairing forces giving rise to multi-quasiparticle states. These intrinsic states are frequently the basis for rotational bands that is a series of excited levels resulting from increasing rotational angular momentum added to the system in this particular particle configuration. These quasiparticle states are also often isomeric, allowing a measurement of the g-factor which can be of use in determining the exact configuration of the state.

To obtain an estimate of the g-factor of such a state theoretically we would start with the basic defining equation [Ho59]

$$\mu_{eff} = \frac{\langle \vec{\mu}_{op} \cdot \vec{I} \rangle}{|I|} \cdot \frac{\vec{I}}{|I|} = \frac{\langle \vec{\mu}_{op} \cdot \vec{I} \rangle}{(I+1)} \qquad (7)$$

That is the effective magnetic moment is the expectation value of the magnetic moment operator parallel to the spin I [B152]. For two quasiparticle states, following the arguments of Hooke and Khoo [Kh73]:

$$\mu_{op} = g_{s_1} S_1 + g_{\ell_1} \ell_1 + g_{s_2} S_2 + g_{\ell_2} \ell_2 + g_R R \qquad (8)$$

where S_1, S_2, ℓ_1, ℓ_2, g_{s_1}, g_{ℓ_1}, etc. are the spin angular momentum of particle 1 and 2, orbital angular momentum of 1 and 2, and the corresponding g-factors. R and g_R are the rotational angular momentum and its g factor. Assuming no interaction between the two quasiparticles,

$$\Omega = K \neq \frac{1}{2}, \text{ and for } I = \Omega = K.$$

$$\mu = \frac{I}{I+1}\{g_s \langle S_{z1} \rangle + g_\ell \langle \ell_{z1} \rangle \pm [g_{s2} \langle S_{z2} \rangle + g_\ell \langle \ell_{z2} \rangle] + g_R\}. \qquad (9)$$

In the asymptotic limit (of high deformation) $\langle S_z \rangle = \Sigma$ and $\langle \ell_z \rangle = \Lambda$ (see Figure 6-1). So

$$\mu = \frac{I}{I+1}\{g_s(\Sigma_1 \pm \Sigma_2) + g_\ell(\Lambda_1 \pm \Lambda_2) + g_R\} \qquad (10)$$

we can also write the magnetic moment in terms of the rotational and intrinsic g-factors g_R and g_K

$$\mu = \frac{I}{I+1}\{Kg_K + g_R\} \qquad (11)$$

Comparing Equations 10 and 11 we see

$$Kg_K = g_s(\Sigma_1 \pm \Sigma_2) + g_\ell(\Lambda_1 \pm \Lambda_2) \qquad (12)$$

Since

$$K = |\Omega_1 \pm \Omega_2| = |(\Sigma_1 + \Lambda_1) \pm (\Sigma_2 + \Lambda_2)| \qquad (13)$$

and for singlet spin states (by definition)

$$\Sigma_1 \pm \Sigma_2 = 0, \qquad K = \Lambda_1 \pm \Lambda_2$$

so $g_K = g_\ell$. For singlet two-quasiparticle states then

$$g_K = 0 \text{ for two neutrons}$$
$$= 1 \text{ for two protons} \qquad (14)$$

For triplet spin states $\Sigma_1 \pm \Sigma_2 = 1$ from Equation (13)

$$g_K = \frac{1}{K}\{g_s + g_\ell(K-1)\} \qquad (15)$$

These equations apply in the asymptotic limit of infinite deformation only but are a good approximation for real highly deformed nuclei. For intermediate cases one can use formulas incorporating parameters of the Nilsson wavefunction to obtain the g-factor [Kh72].

III. EXPERIMENTAL

3.1. Methods for Measuring g-Factors

To measure the magnetic moment of a nucleus or g-factor one must measure the magnitude of the Zeeman splitting of the nuclear or hyperfine states. The splitting between two magnetic substates in the simple case of a nucleus in a magnetic field will be $\Delta E = gH\mu_N$ which gives the g-factor directly. In some experiments the multiplicity of substates can be determined which allows the nuclear spin I to be determined and thus the magnetic moment $\mu = gI$. Atomic beam experiments similar to the original Stern-Gerlach experiment have been done to determine spins and moments of many stable elements. Nuclear magnetic resonance (NMR) is the application of rf radiation of the energy equal to the difference in energy of the magnetic substates, which induces transitions between them. NMR is frequently used in conjunction with atomic beams and optical spectroscopy to increase the accuracy. Optical spectroscopy can be used to view directly the splitting of the hyperfine structure or to detect NMR resonances. Mössbauer spectroscopy looks directly at the nuclear states by recoil free resonance emission-

absorption of Doppler shifted low energy γ-rays. A moving source provides the Doppler shifted γ's which are passed through a cooled absorber where the γ's are selectively absorbed. A plot of absorption vs. source velocity gives a pattern similar to an optical interferomery experiment. The splitting between absorption peaks gives the energy difference between substates and thus the g-factor.

The above methods are suitable for determining g-factors of stable isotopes or unstable ones with a long half life that can be obtained in sizable quantities. To determine g-factors of short lived states, for example nuclear isomers populated in in-beam nuclear reactions, one must use the radiation depopulating the isomer as a probe of what's happening. Luckily, γ's and β's are emitted with an asymmetric angular distribution with respect to the nuclear spin axis and this can be used to determine the orientation of the nucleus. NMR can be used then exploiting the change in the angular distribution to indicate occurrance of substate transitions. There is another way to obtain g-factors and that is to measure the rate of precession of the nucleus in a magnetic field. The Larmour frequency (precession frequency) ω_L is equal to the NMR rf resonant frequency $\hbar\nu_{rf} = \hbar\omega_L = \Delta E_{substates} = gH\mu_N$.

Since the angular distribution of γ-rays depopulating

some isomer will follow the precession of the nuclear spin-magnetic moment axis, one can obtain ω_L from the frequency of precession of the angular distribution. One can't observe the precession of a single nucleus only, since once a nucleus deexcites, it no longer exists in that state and has given up its signature for detection, the γ-ray. So in order to plot distribution position vs. time one must have a group of nuclei all aligned the same or nearly the same relative to each other.

There are several methods for obtaining nuclear spin alignment. One method is to cool the source to a point where thermal energy is lower than the nuclear and electron spin-spin interactions allowing alignment to occur. Another method makes use of the alignment provided in an in-beam nuclear reaction, the perturbed angular distribution technique (PAD). In this method the arrival of a beam pulse at the target creates a group of oriented nuclei which precess in an external magnetic field. The precession frequency is determined from an oscillation in the count rate as a function of time in a detector observing radiation deexciting the state of interest.

3.2. The Time Differential Perturbed Angular Distribution Method (TDPAD)

3.2.1. Nuclear Reactions and Alignment

In a typical in-beam γ-ray experiment a thin ∿1 mg/cm^2 foil is bombarded by the cyclotron beam. Fusion of the projectile with the target nucleus yields a compound nucleus of high energy. The compound nucleus very rapidly emits neutrons (of low angular momentum due to the centrifugal barrier). The recoiling nucleus comes to rest in about a picosecond for heavier nuclei, whereafter most of the discrete γ-rays are emitted. The compound nucleus is formed with the spin axis perpendicular to the beam (Figure 3-1) similar to what one would expect from hitting a billiard ball off center with a projectile. The neutrons cause little disturbance of the alignment because of their low angular momentum and the stopping process with its many collisions over a very short time doesn't precess the nucleus very far either. The cascade of γ-rays can cause some loss of orientation but most spin dealignment comes from nanosecond time scale interactions between the nuclear moment and the electrons and field gradients in the lattice of the stopping material.

3.2.2. Angular Distributions

According to the theory worked out by Frauenfelder and Steffen [St68] the angular distribution of γ-rays from aligned (Gaussian distribution about m = 0, beam being z axis) states is

$$W(\theta) = \sum_{\substack{k \\ \text{even}}}^{2\lambda} A_k P_k(\cos\theta) \qquad (16)$$

where P_k are the Legendre polynomials and A_k are the expansion coefficients, and λ the multipolarity of the γ-ray. A_2 is positive for stretched quadrupole (λ = 2) and negative for stretched dipole transitions. The result is a peanut shaped distribution about the beam axis (Figure 3-1). In the time differential perturbed angular distribution method a magnetic field is applied perpendicular to the beam, Figure 3-1, causing the nuclei to precess at angular frequency ω_L around H. The oscillation of count rate as a function of time in a γ detector placed at a fixed angle is used to determine ω_L. Figure 4-1 shows a typical time spectrum of an isomer decaying in a magnetic field. It is an exponential decay modulated by a sine function. The equation for the time spectrum would be

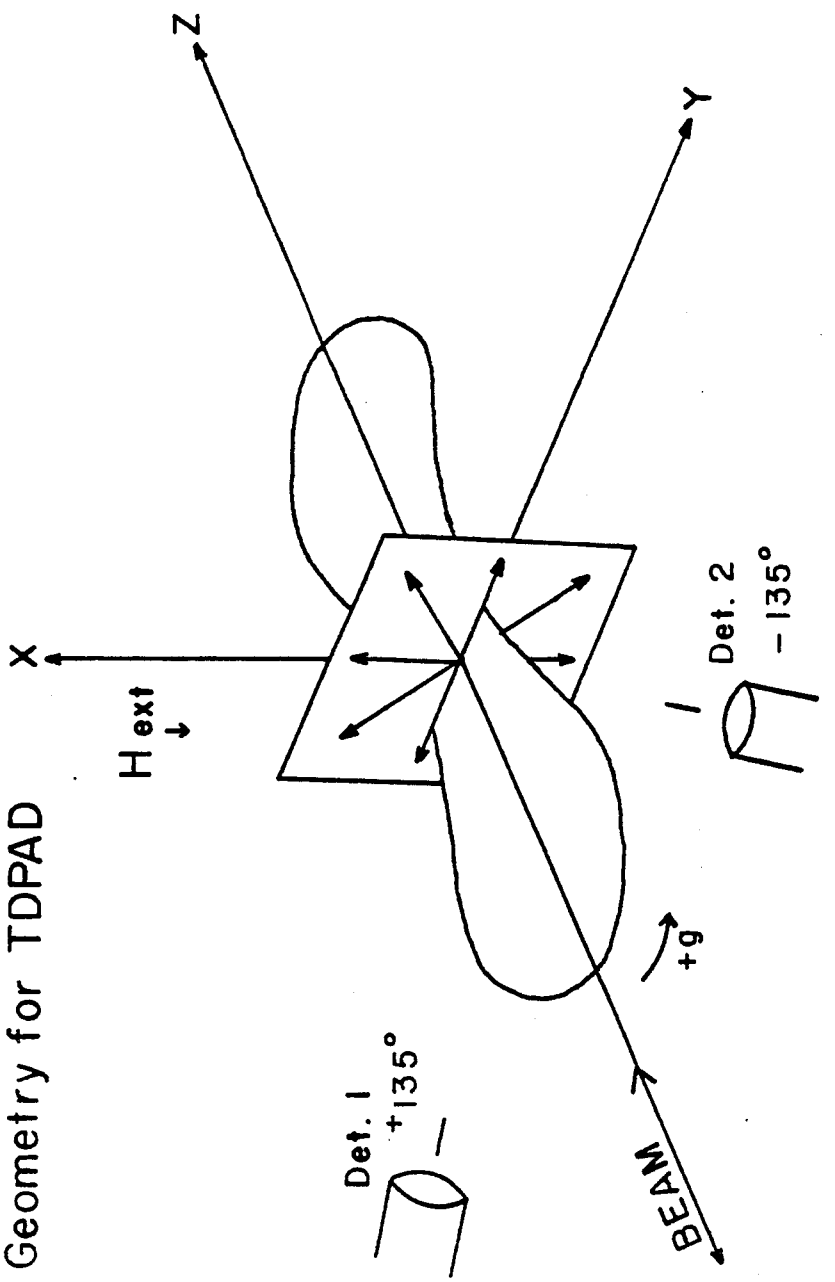

Figure 3-1. Angular distribution (quadrupole) and spin alignment in-beam.

$$N = N_o e^{-\lambda t} W(\theta) \qquad (17)$$

where $\theta = \theta_o - \omega_L t$, and λ is the decay constant of the isomer. Taking the expansion for W to k = 2 at $\theta_o = 135°$, we have

$$N = N_o e^{-\lambda t}[1 + \tfrac{1}{4} A_2 + \tfrac{3}{4} A_2 \sin(2\omega_L t)] \qquad (18)$$

In the time integral method one obtains the angular distribution by recording count rate as a function of angle with field on and off. The shift in the angular distribution θ observed would be $\theta = \omega_L \tau$ where τ is the mean lifetime of the state. This method would be of use when τ is too short for a differential measurement. Equations 17 and 18 assume the alignment is retained throughout the observed lifetime. This is not always the case, however. Many times it is difficult to maintain alignment for a sufficiently long time. The electric quadrupole effect plays a large part in causing a relaxation of the alignment [Ab53]. Electric field gradients created by beam-induced lattice-defects surrounding the nucleus interact with its quadrupole moment causing a disorientation of the spin [Be70]. Nuclei coming to rest in interstitial

lattice sites experience a similar effect due to inherent field gradients at these sites as well as nuclei stopping in a substitutional position in some lattices of non-cubic symmetry. The relaxation is not spatially symmetric with time due to the presence of the magnetic field. Two relaxation times are defined as commonly used in NMR theory; T_1 the longitudinal relaxation time, involves magnetic substate (spin orientation) changes with respect to the magnetic field, and T_2 the transverse relaxation time involves a randomization of the alignment in the x-y plane. Clearly a non-homogeneity in the magnetic field could cause differences in precession frequencies between nuclei causing this T_2 type randomization. Due to these inhomogenieties in field strength (including quadrupole interactions) T_2 is less than T_1. After a time governed by T_2 the angular distribution in the x-y plane would be isotropic whereas in planes containing the z axis it would still be non-isotropic until after a time governed by T_1. For the TDPAD method where detectors are placed in the x-y plane, T_2 would be the limiting factor.

Gabriel treats the PAC for the general case including relaxation and introduces the formulas [Ga69]

$$W(\theta,\phi) = \frac{4\pi}{2k+1} \sum_{k,q} A_k \, Y_k^q \, G_{kk}^{qq} \, Y_k^{q\,*} \qquad (19)$$

$$G_{kk}^{qq} = e^{-it\nu_{kq}-\lambda_{kq}t}$$

$$\lambda_{kq} = \frac{k(k+1)}{2T_1} + q^2 \left(\frac{1}{T_2} - \frac{1}{T_1}\right)$$

$$\nu_{kq} = q\,\omega_L + M_{kk}^{qq}$$

G_{kk}^{qq} is the perturbation factor introduced, A_k is the usual anisotropy coefficient as before, Y_k^q are the spherical harmonic functions, k goes from 0 to 2λ or $2I$ as in the previous eqution, and q the "multipole orientation" goes from $-k$ to $+k$ and is an even function. M_{kk}^{qq} is a second order frequency perturbation which might be important only when $\omega_L\tau_c \approx 1$, where τ_c is the correlation time of the time dependent perturbation. The magnitude of M_{kk}^{qq} cannot be estimated without knowing the correlation mechanism, but the effect of this term has been shown to be suitably insignificant in most experiments. Expanding this equation to $k = 2$, $\theta = 90°$ and $\phi = 135°$ (typical) and taking only the real part of G_{kk}^{qq}:

$$W = 1 + \frac{1}{4} A_2 e^{-\lambda_{20} t} + \frac{3}{4} A_2 e^{-\lambda_{22} t} \cos(2\omega_L) \qquad (20)$$

Note the exponential decay of the first and second A_2 term. The first decays with constant λ_{20} depending only on T_1, whereas the second term decays with constant λ_{22} dependent on both T_1 and T_2. Most experiments are not precise enough to measure T_1 and T_2, accurately, but a detector placed out of the x-y plane would be able to measure T_1.

3.2.3. Asymmetry Ratio, R(t), Formation

In a TDPAD experiment it is useful to get rid of the exponential decay factor from the time spectrum and obtain a pure sine function that can be fit to obtain the frequency. To do this one can use two detectors in the experiment placed 90° apart. The time spectra for each detector will be out of phase by 1/2 a period, enabling a ratio

$$R(t) = \frac{N(45°) - N(-45°)}{N(45°) + N(-45°)} \qquad (21)$$

to be formed, resulting in first order in a regular sine

function. Taking Equation (19) to be k = 2, $\theta = 135°$ and substituting in Equation (21), one sees

$$R(t) = \frac{\frac{3}{4} A_2 \sin(2\omega_L t)}{1 + \frac{1}{4} A_2} \tag{22}$$

If one expands Equation (19) to k = 4, one obtains

$$R(t) = \frac{\beta_2 \sin 2\omega_L t}{1 + \beta_0 - \beta_4 \cos 4\omega_L t} . \tag{23}$$

where

$$\beta_0 = \frac{1}{4} A_2 e^{-\lambda_{20} t} + \frac{9}{64} A_4 e^{-\lambda_{40} t}$$

$$\beta_2 = \frac{3}{4} A_2 e^{-\lambda_{22} t} + \frac{5}{16} A_4 e^{-\lambda_{42} t}$$

$$\beta_4 = \frac{35}{64} A_4 e^{-\lambda_{44} t}$$

Even if A_4 is not insignificant the effect on R(t) as seen from the equation is pretty small.

3.3. Magnet Construction

3.3.1. Experimental Design and Considerations

The main factors to consider in attempting to measure a g-factor of some isomer with this method are: the lifetime of the isomer, the magnitude of the expected g-factor, the relaxation time (suitable host lattice), the magnetic field strengths, the maximum beam pulsing interval, and the population intensity of the isomer. For good accuracy one would like to observe at least one full cycle of the sine function which is half the Larmour period so

$$N\tau \geq \frac{\hbar\pi}{H\mu_N g} \quad \text{or} \quad N\tau_{(nsec)} \geq \frac{656}{H(kg)g} \tag{24}$$

where $N\tau$ is the number of lifetimes the radiation is-servable. This means that in general a high magnetic field and high g-factor are more desirable although there is an upper limit to the observable Larmour frequency set by the time resolution of the system, 4-10 nsec. It is also important that the alignment be preserved over a significant portion of the observable lifetime of the radiation. One must choose a suitable target or target

backing to host the recoils such as a metal with a cubic lattice structure like Pb. Use of a target heater may be necessary to allow the fast annealing of lattice dislocations in the case of some high melting point materials, in order to extend the relaxation time. The beam pulsing period may be an important factor. At the MSU cyclotron the system used to provide microscopic pulses (those that don't have a finer structure) of varied duration is an electrostatic beam sweeper. A sinusoidal voltage is applied to a set of deflecting plates that sweeps the beam past a slit. The frequency of the sweeper is some lower harmonic of the cyclotron frequency allowing one to separate up to one out of 11 natural beam pulses (period $\sim$50 nsec). The maximum pulse period attainable is about 1 sec. For isomers with lifetimes greater than about 200 nsec the radiation produced by previous beam bursts has a time overlap with radiation from later beam bursts, thus affecting the time spectrum. The effect of this overlay should be taken into account in the analysis, although for a simple system the frequency of the oscillation of the R(t) spectrum won't be affected, only the amplitude. For the case when the half life is not much less than the beam pulsing interval a stroboscopic resonance experiment can be done [Ch68]. It is still important that the relaxation time be greater than the half life or the spectrum would be washed out by isotropic background.

The time required to take data with sufficient statistics is determined by the intensity of the line(s) depopulating the isomer in the delayed spectrum, the magnitude of A_2 and ω_L, and the relaxation time.

3.3.2. Data Taking Method and Electronics

There are a few different ways to take data depending on the data taking programs available. One method is to do two separate timing experiments, one with each detector (Figure 3-2a). One can then use the program TOOTSIE setting bands on the γ-rays and collecting the time spectra (see Appendix for notes on TOOTSIE). Another method is to OR the two detectors and strobe 3 ADC's whenever either detector fires, two of which contain the information for the event. This method was used in conjunction with a program written by Brian Jeltema (GFACTOR) on the PDP-11/45. The PDP is count rate limited to $\sim$5 K cps rate with the Camac ADC's so one must gate out or scale down the prompt events in order to take data efficiently (Figure 3-2b).

3.3.3. Design and Construction of the g-Factor Magnet

To do the TDPAD experiments the target must be held in a magnetic field perpendicular to the beam. A magnet had to be constructed that would contain a vacuum-target

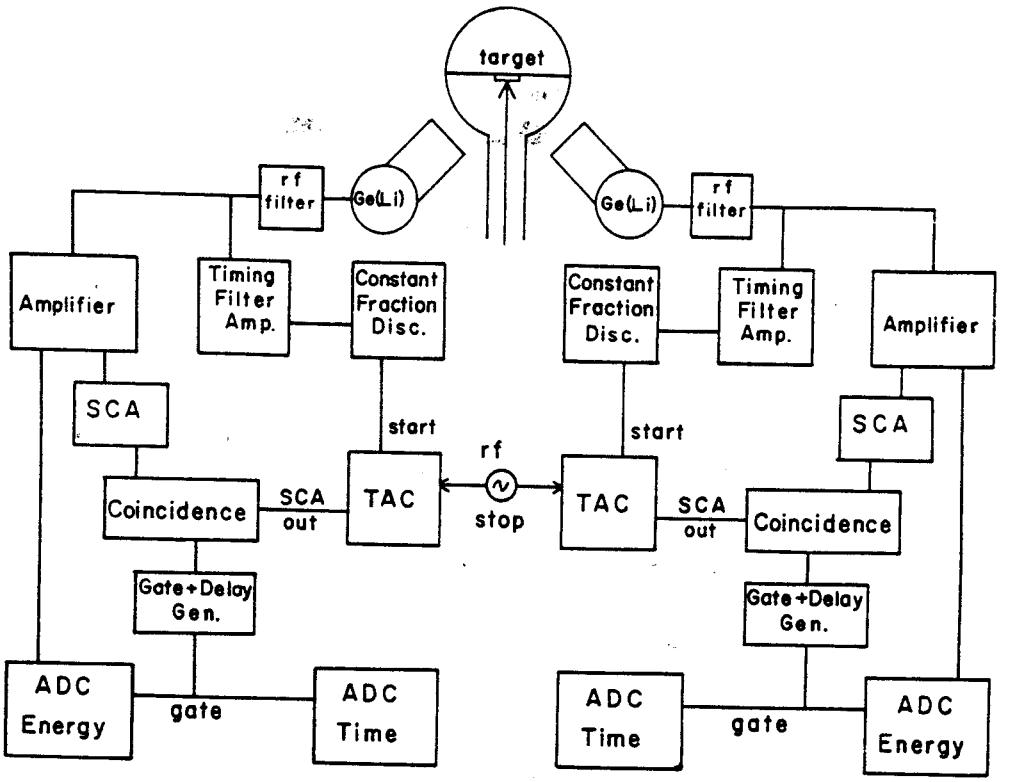

Figure 3-2a. Electronics for a g-factor experiment, separate timing.

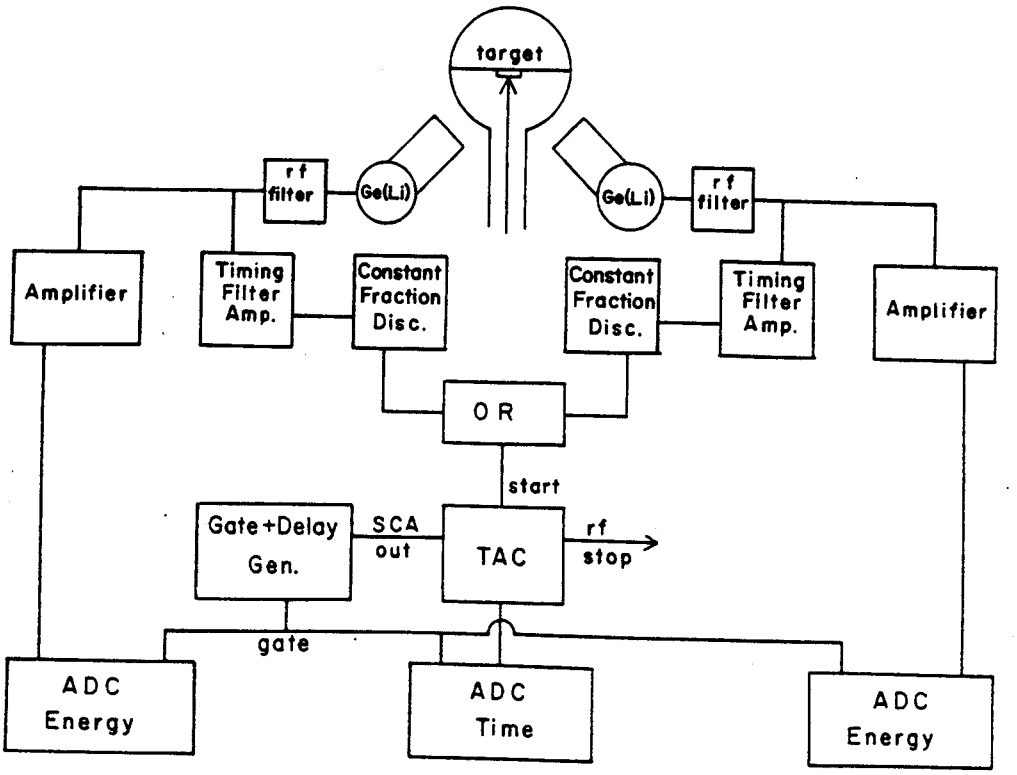

Figure 3-2b. Electronics for a g-factor experiment, combined timing.

chamber between its pole tips. The pole tips and thus the area of the magnetic field were kept small so the beam would be bent as little as possible before reaching the target. A high magnetic field was desired so the pole tip gap was made fairly small. The maximum field attainable with a non-superconducting iron magnet with reasonable currents is around the saturation field for iron, 22 kgauss. It has been found that the optimum pole tip shape is a truncated cone with 45° slope [K165]. This is true when the coils are placed around the sloping portion of the pole tip, since the field lines get pinched together in the coil area, thus assisting in achieving high flux density (field) at the tips. The magnet that was used was a small beam line magnet that was modified by adding yoke extensions and new pole tips. The 45° pole tip design was used although the coils were left at the top of the poles rather than the middle. The pole tips were machined from castings generously supplied by the Bay City Foundry maker of the iron for the MSU K=500 superconducting cyclotron magnet. A diagram of the magnet is given in Figure 3-3. The top pole tip is an inch smaller in diameter than shown due to an error by the shop. The coils consist of 4 layers top and bottom of 36 turns each 1/4" square hollow conductor copper encased in epoxy. For greater cooling the water supply was remade to deliver parallel feeding of all 8 coils. Field calculations were done before

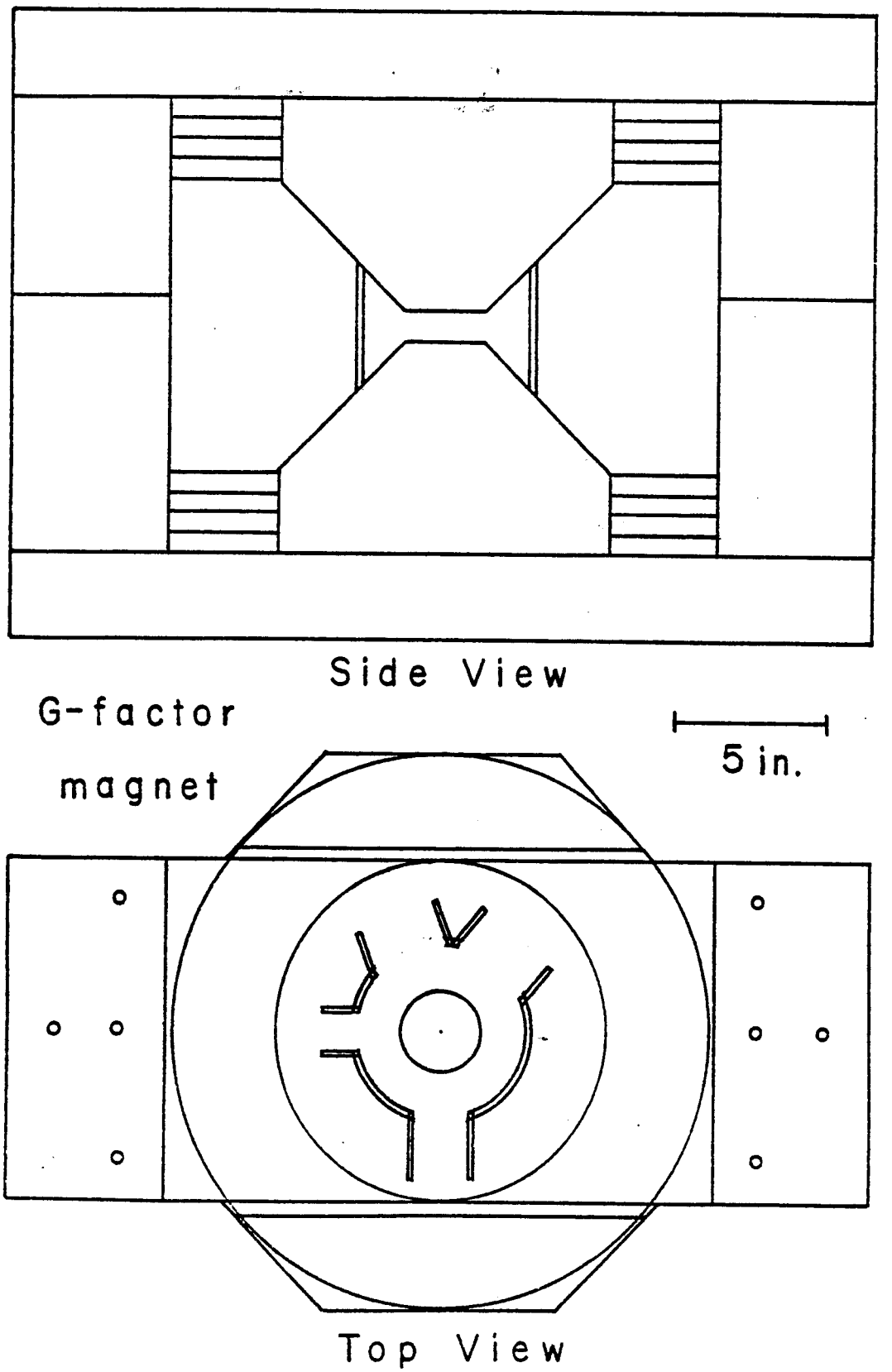

Figure 3-3. The g-factor magnet.

construction. It is possible to do a magnetic circuit calculation by hand. A magnetic circuit is analogous to a DC electrical circuit; EMF is equivalent to magneto motive force = NI (ampere turns), resistance is reluctance $R = \int \frac{d\ell}{\mu A}$ where A is cross sectional area, $d\ell$ length, μ is the permeability, and current is the flux Φ [K165]. The equivalent Ohm's Law is $NI = R\Phi$. In this case, however, resistance varies with flux density (field) since μ varies with field. One can start with a desired field strength at the gap and estimated flux loss to fringing fields and determine total flux, the reluctance of each section of the magnet and determine total NI needed. It is difficult to estimate the fringing field due to the sloped pole tips, however. Another method is to start with the NI available and calculate the final field. An iterative calculation is necessary here, however, since the reluctance depends on the flux density. A program called TRIM adapted by Dave Johnson for the Σ-7 computer was used to estimate the field by this iterative method. A grid is made of the magnet dimensions assuming cylindrical symmetry including material and coil data. The program estimated that at 308 amps a 22.8 kgauss field could be achieved and at 500 amps 24.7 kgauss. A four inch diffusion pump setup from an old Veeco leak detector was used for a pumping station. A "Spectro Magnetic" DC power supply shared with the

neutron time of flight set up was used to power the magnet. The supply delivered more than enough current at good regulation. A field calibration test was done first with a Hall probe and then using a flip coil which had been calibrated with NMR. The results are in Figure 3-4. The measured field was about 10% smaller than the prediction from TRIM. A thermal switch placed on the outlet side of each coil guarded against overheating. The maximum continuous current before trip-off was around 430 amps. The water flow rate was about 3 cu ft/min, the voltage across the magnet at 400 amps was around 50 volts, thus dissipating around 20 kwatts. As seen from the graph, 400 amps is about the saturation point of the magnet. The reproducability of the magnetic field with dial setting was tested and found good to 1%.

A field profile was also done as a function of distance from the center of the gap along the beam entrance line using a Hall probe (current = 300 amps). This is shown in Figure 3-5. The amount of beam bending can be calculated from this curve. A ray tracing code gives a bending angle of 7.4° at the target, with 48 MeV alpha particles. A simple geometrical calculation can be done by assuming an effective gap radius so as to give the same area under the curve as that in Figure 3-5. The effective gap radius turns out to be 3.03 in a 20.5 kgauss field. The radius of curvature of the beam (non-relativistic)

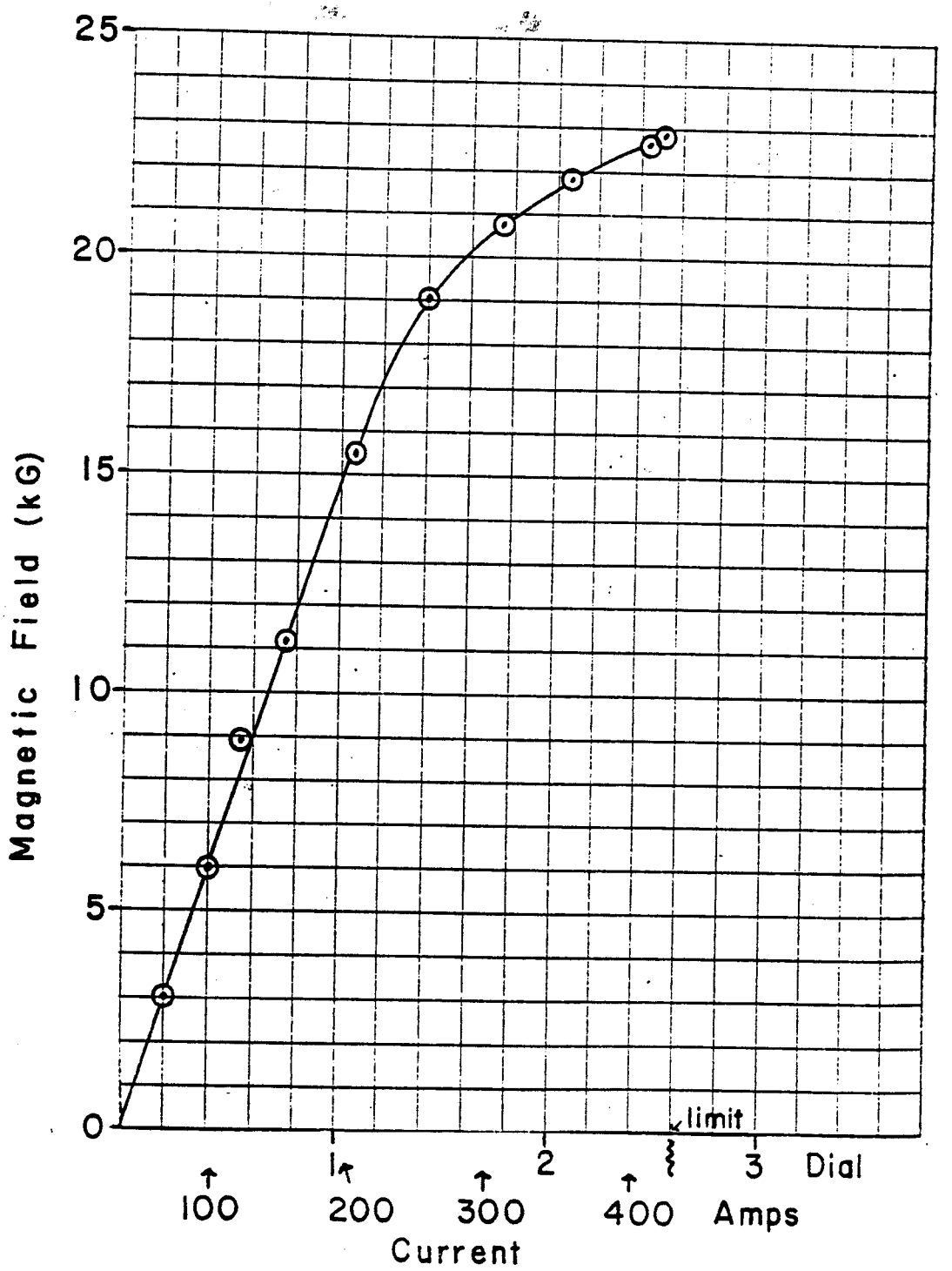

Figure 3-4. Magnet calibration: field as a function of current.

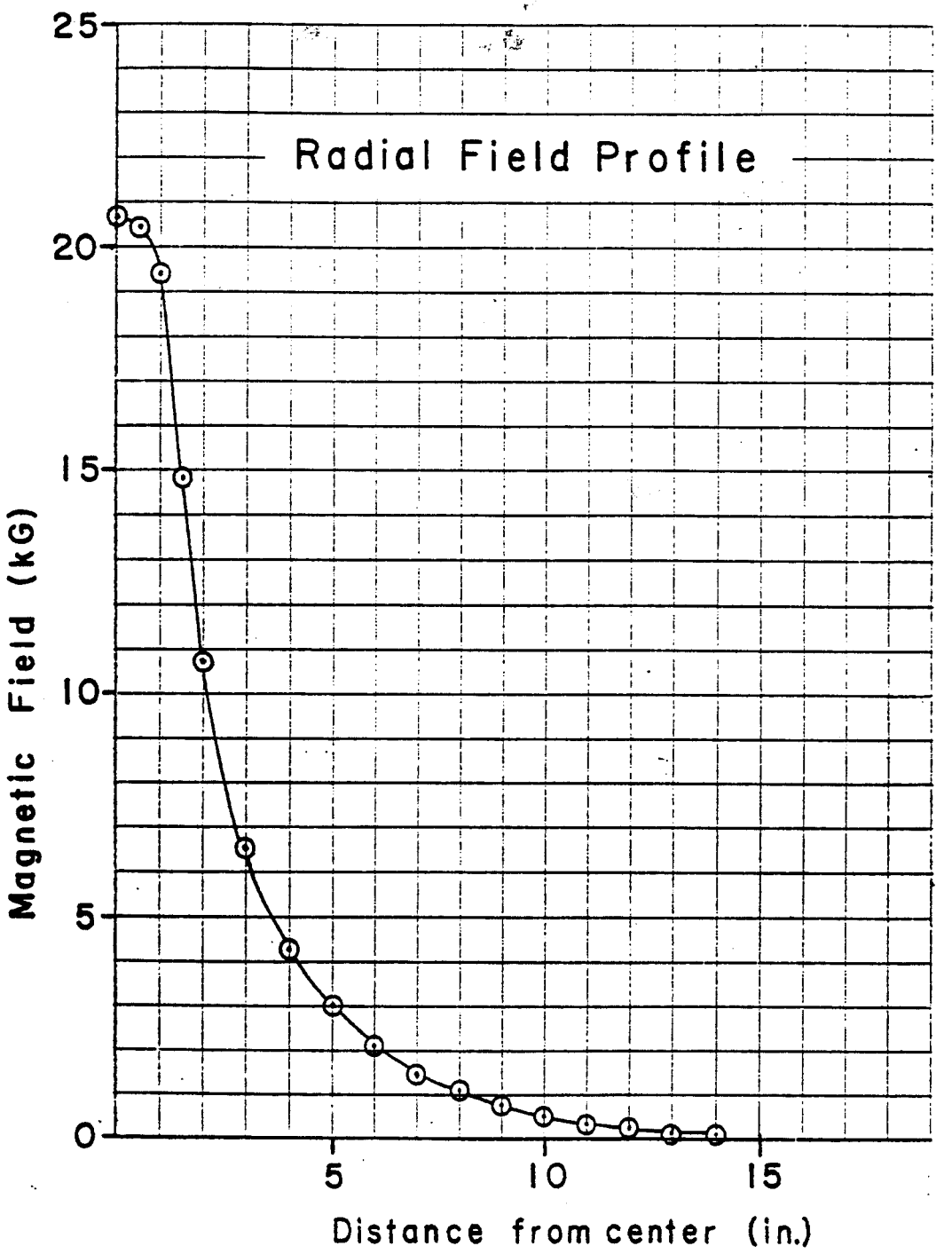

Figure 3-5. Magnetic field profile as a function of distance from center along median plane.

is

$$r_{(cm)} = \frac{144\sqrt{mE(MeV)}}{B(kg)q}$$

and the angle at the target will be

$$\Theta \approx \sin^{-1} \frac{d}{r}$$

where d is the effective radius of the gap. This gives 9.1° as a result. When running lower rigidity beams and higher fields one would expect a greater bending angle, so this would be a typical minimum bending angle.

3.3.4. Target Chamber Design

The target chamber was designed to be as simple as possible and yet afford suitable access and provide an exit path for the beam. Since the beam is bent significantly, an angled exit port is useful, so two exit-access ports were made, one at a larger angle than the other. The whole chamber was cut from a 5-1/4" 6060 aluminum pipe. A 2" diameter aluminum entrance pipe was

used to provide easy positioning of the Ge(Li) detectors at ±135°. The exit ports were 2.87" diam. and fitted with standard beam line flanges. One port served as a window through which a scintillator could be viewed. The targets slide in rails between the pole tips. Two targets or a target and scintillator can be positioned in the chamber. These are attached to a brass rod and movable thorugh a sliding seal in the target port on the side of the chamber, see Figure 3-6. A collimator is situated 0.25 in from the target to facilitate focusing of the beam. In a 20 kgauss field electrons with energy 14.3 MeV or lower from the target won't reach the collimator. The rear of the chamber and the pole tips were covered with 1/8" thick lead sheet to prevent them from being activated by the beam.

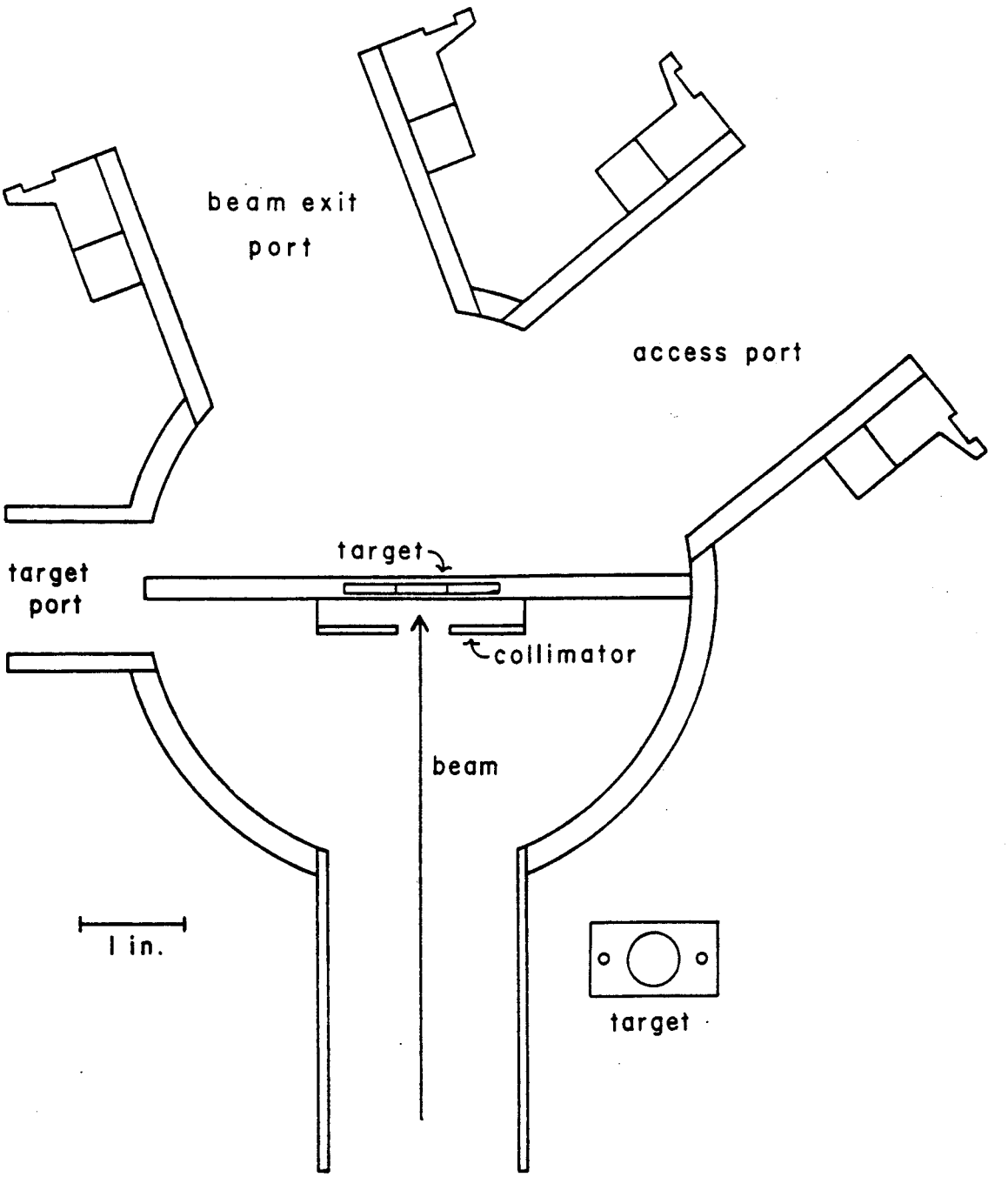

Figure 3-6. Target chamber and target.

IV. RESULTS OF MEASUREMENTS

4.1. ^{210}Po Test

To test out the system the g-factor of a previously well known case, the 8^+ isomer of ^{210}Po was measured. To produce the isomer we used the reaction ^{208}Pb (α,2n)-^{210}Po. 25 MeV alphas were used on a 2 mil (58 mg/cm^2) natural Pb target. A partial level scheme is given in Figure 4-1. The 8^+ isomer has $t_{1/2}$ = 112 ns and g = 0.910(5) [Ya70]. The 6^+ level has $t_{1/2}$ = 41 ns and g = 0.93(2) [Ya70],[Na73]. The line we observed was the 1180 keV line. To minimize background from beam hitting the pipe, a 4 ft long beam dump was used with a split Faraday cup at the end in order to allow the beam to be centered in the beam dump by adjusting the field of the magnet. A field of 18.6(1) kgauss was used. The beam was swept 1 out of 4 leaving 261.6 nsec between the beam bursts. The data taking method in Figure 3-2a was used, just a normal timing experiment with the γ-side gated. Only one detector was used in this experiment; and it was placed at 135°. The 1180 keV line was gated and the resulting TAC spectrum showed the oscillations due to the precessing angular distribution very clearly (Figure 4-1). The data were fit to the function

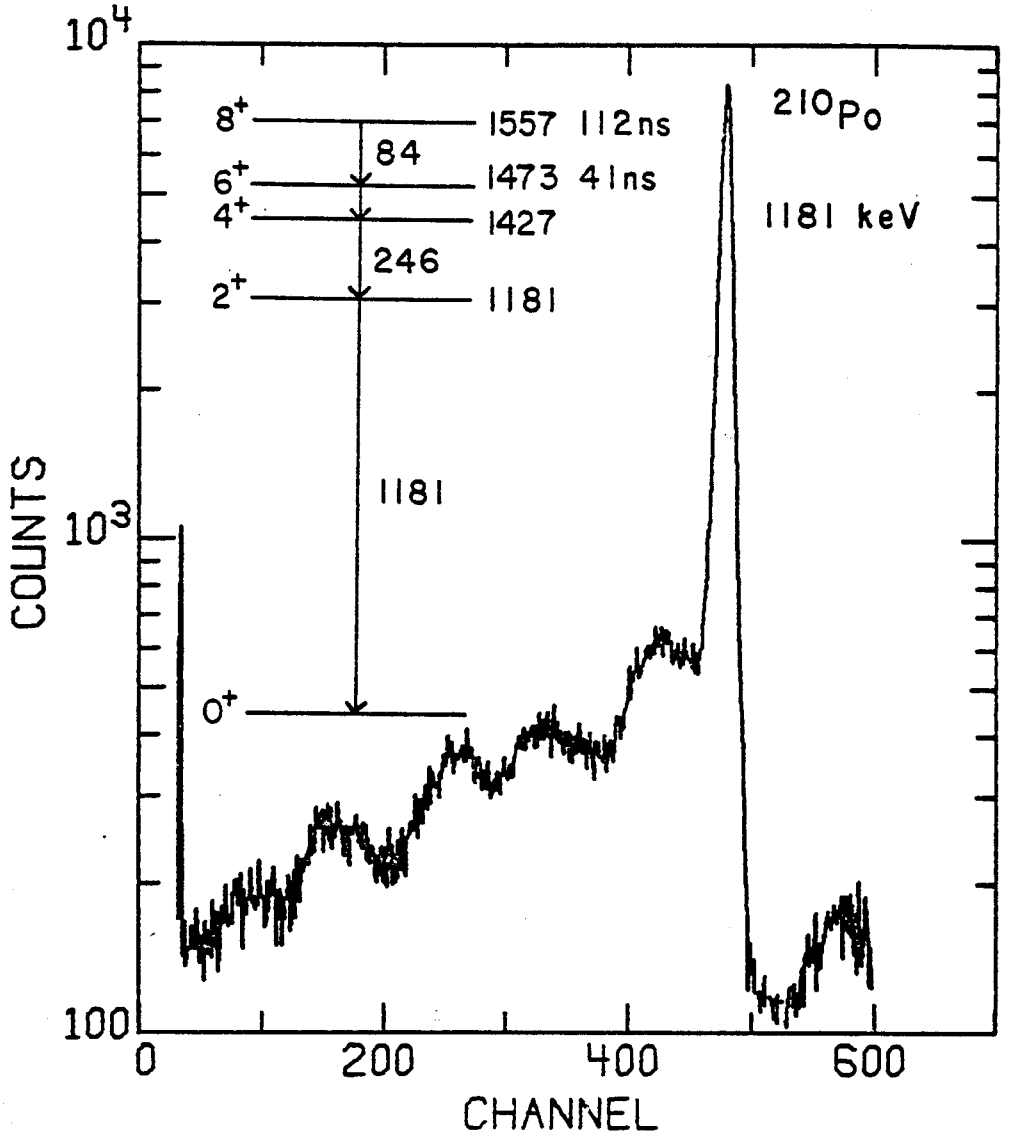

Figure 4-1. ^{210}Po TAC and partial decay scheme.

$$N = N_0 e^{-t/\tau}[1 + \frac{1}{4}A_2 + \frac{3}{4}A_2 \sin(2\omega_L t - 2\Delta\theta)], \qquad (25)$$

where $\Delta\theta$ is the phase shift due to the beam bending and other factors, with the least squares program KINFIT [Na71]. N_0, τ, A_2, ω_L, and $\Delta\theta$ were left as parameters in the fit. T_ω the period of oscillation = $\frac{\pi}{\omega_L}$ was found to be 38.8(5) nsec. Using the equation

$$g = \frac{\hbar\pi}{H\mu_N T_\omega} \qquad (26)$$

(Section 3.1) one obtains g = 0.909(13), very close to the accepted value 0.910(5) [Na74]. There is a complication, however, due to the presence of the 38 nsec 6^+ isomer. Since the 1180 keV line is being observed, the nucleus will have precessed under the influence of the 6^+ isomer also, introducing a change in the observed ω_L and a phase shift (incorporated here in $\Delta\theta$). Nagamya gives a detailed treatment of the PAD pattern equation with the presence of two isomers [Na70]. He also makes reference to the ^{210}Po case and how different experiments can yield different g-factors and half lives depending on the beam pulsing interval T and the initial

population ratio of the two isomers. Using his estimated value for $\alpha = N_1/N_2 = .9$ the initial population ratio, and our value T = 262 nsec the apparent ω_L should be $\omega_L = 0.90\ \omega_1 + 0.10\ \omega_2$. Substituting the measured $\omega_L = 38.9$ nsec and calculating ω_2 from Equation (26) assuming $g_2 = 0.93$ [Na74] one obtains $\omega_1 = 38.9$ nsec corresponding to g = 0.907 showing a minimal deviation in this case due to the similarity of the g-factors g_1 and g_2 and the small effect of ω_2 on ω_L. This experiment confirmed our faith in the setup and indicated certain needed improvements in the target positioning method. Holes were put in the edges of the target frames as in Figure 3-6 and a set screw was installed in the target positioning rod to rigidly fix the targets. A metal sleeve was used on the outside portion of the rod to fix target and scintillator position relative to the collimator hole.

4.2. The g-Factors of the $19/2^-$ and $11/2^-$ States in ^{115}Sb

4.2.1. Introduction

The nucleus ^{115}Sb lies in a shape transitional region. It is one proton outside the Z = 50 closed shell and exhibits some vibrational states similar to the neighboring Sn nuclei, but it also has a rotational band built on the $9/2^+[404]$ Nilsson state [Ga75]. The non-rotational

part of the spectrum has been explained by coupling a $d_{5/2}$ proton to excited states in the ^{114}Sn core [Va71]. Recently an in-beam γ-ray study of ^{115}Sb yielded data on high spin states in that nucleus [Br77]. Three isomers were seen: a $t_{1/2}$ = 6.7 nsec, $11/2^-$ isomer at 1300.2 keV, a 156 ns $19/2^-$ isomer at 2796.3 and a 4.0 ns $25/2^+$ isomer at 3059.7 keV corresponding to a $d_{5/2}$ proton coupled to the ^{114}Sn 3^-, 7^- and 10^+ states, respectively. Figure 4-2 shows a partial decay scheme involving those isomers. The $19/2^-$ isomer is thought to be a three particle state $[\pi d_{5/2} \otimes \nu h_{11/2} \otimes \nu d_{3/2}]$, where $[\nu h_{11/2} \otimes \nu d_{3/2}]$ is the 7^- state in the ^{114}Sn core. According to Bron [Br77] the wavefunction probably contains some admixture of $[\pi h_{11/2} \otimes 4^+]$ since the transition $19/2^-$ to $11/2^-$ in ^{115}Sb is enhanced about a factor of three over the corresponding 7^- to 5^- transition in ^{114}Sn. The measurement of the g-factor could give an indication of the extent of the admixture.

For the $11/2^-$ isomer a g-factor measurement would indicate the extent of possible admixture of the $[\pi d_{5/2} \otimes 3^-$ (octupole vibration)] with a pure $\pi h_{11/2}$ configuration.

4.2.2. Experiment

The g-factors were measured using the time differential perturbed angular distribution technique (TDPAD). The reaction was ^{115}In $(\alpha,4n\gamma)^{115}$Sb, induced by a 48 MeV

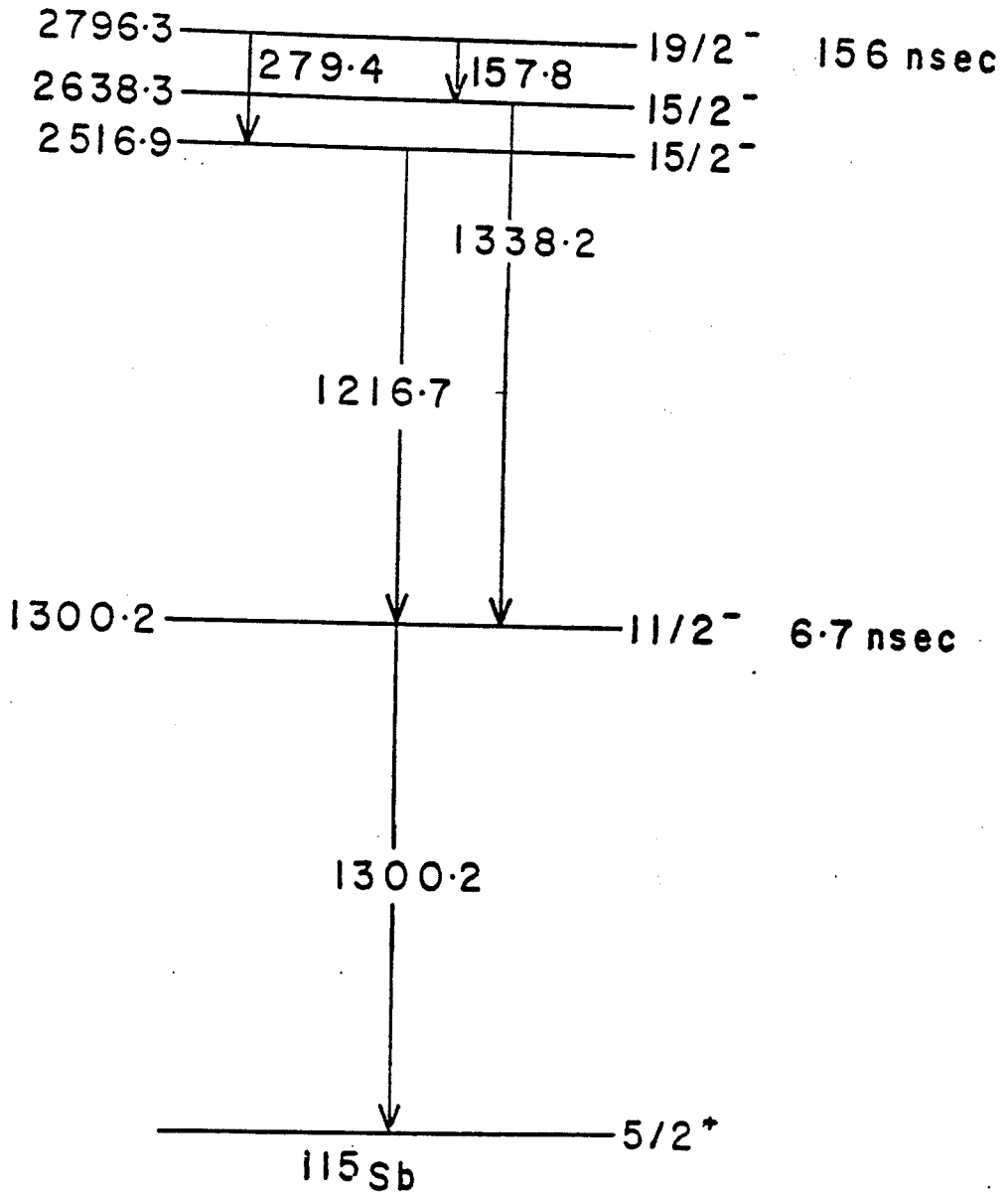

Figure 4-2. Partial decay scheme for ^{115}Sb.

α particle beam from the MSU cyclotron. The target was a thick (110 mg/cm^2) natural metallic In foil (95.7% ^{115}In). Indium is a good host lattice for the ^{115}Sb recoils due in part to its tetragonal lattice structure which maintains the alignment over several precession cycles. The low melting point of In (156°C) insures a high mobility of lattice defects induced by the beam even at room temperature and thus reduces the main cause of loss of alignment generally experienced with this technique.

The magnet used produced a 22.7 kG magnetic flux density with less than 0.5% deviation over the target area. The field was calibrated to less than 1% error using a flip coil that had been calibrated with nuclear magnetic resonance. Two 10% efficient Ge(Li) detectors were placed at ±135° to the beam. The beam was chopped with an electrostatic deflector so there were 526 ns between bursts. Six energy gates were set per detector, one on the 1217 keV line, one on the 1300 keV line, and two background gates, one on either side of each peak.

Figure 4-3 shows the background subtracted time to amplitude converter (TAC) spectra and the normalized sum spectra formed by adding the spectra from the two detectors. The 1300 keV transition is a doublet containing some of the 1294 keV line from ^{116}Sb decay. The amount of this background in each 1300 keV spectrum was

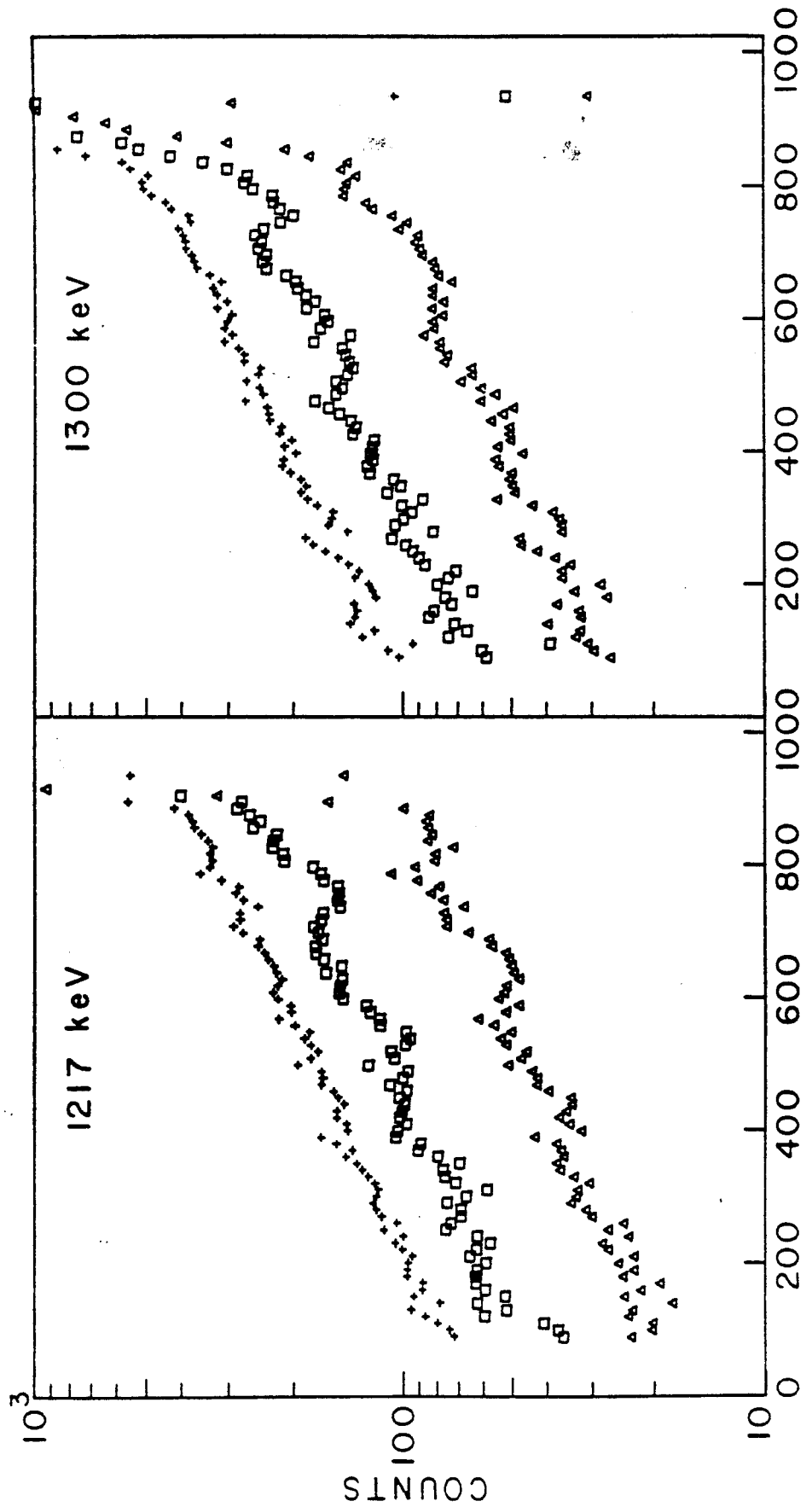

Figure 4-3. Time spectra for the 1217 and 1300 keV lines in ^{115}Sb. Detector 1 (-135°) are points, detector 2 (135°) Δ, and sum +. Points + and □ have been shifted up half a decade for clarity.

determined by fitting each TAC spectrum to the equation for a time spectrum incorporating the 156 ns half-life as determined from the 1217 keV sum TAC, plus a background due to the 15 min decay of ^{116}Sb. The ratio

$$R(t) = \frac{N(1)-N(2)}{N(1)+N(2)} \tag{27}$$

was formed for each γ ray, where N(1) and N(2) are counts from detector 1 and 2, respectively (Figure 4-4). The time-dependent equation for the counts N in a TAC spectrum in a pulsed beam and magnetic field is [Mo76]

$$N(t) = N_0 e^{-\lambda t}(1-e^{-\lambda T})^{-1}$$

$$x\ [1+B_0 \pm B_2 \sin(2\omega t - 2\Delta\theta + \phi_2)$$

$$-B_4 \cos(4\omega t - 4\Delta\theta + \phi_4)], \tag{28}$$

where λ is the decay constant of the isomer, T the time between beam bursts, ω is the precession frequency, and $\Delta\theta$ the correction for beam bending due to the magnet. The coefficients

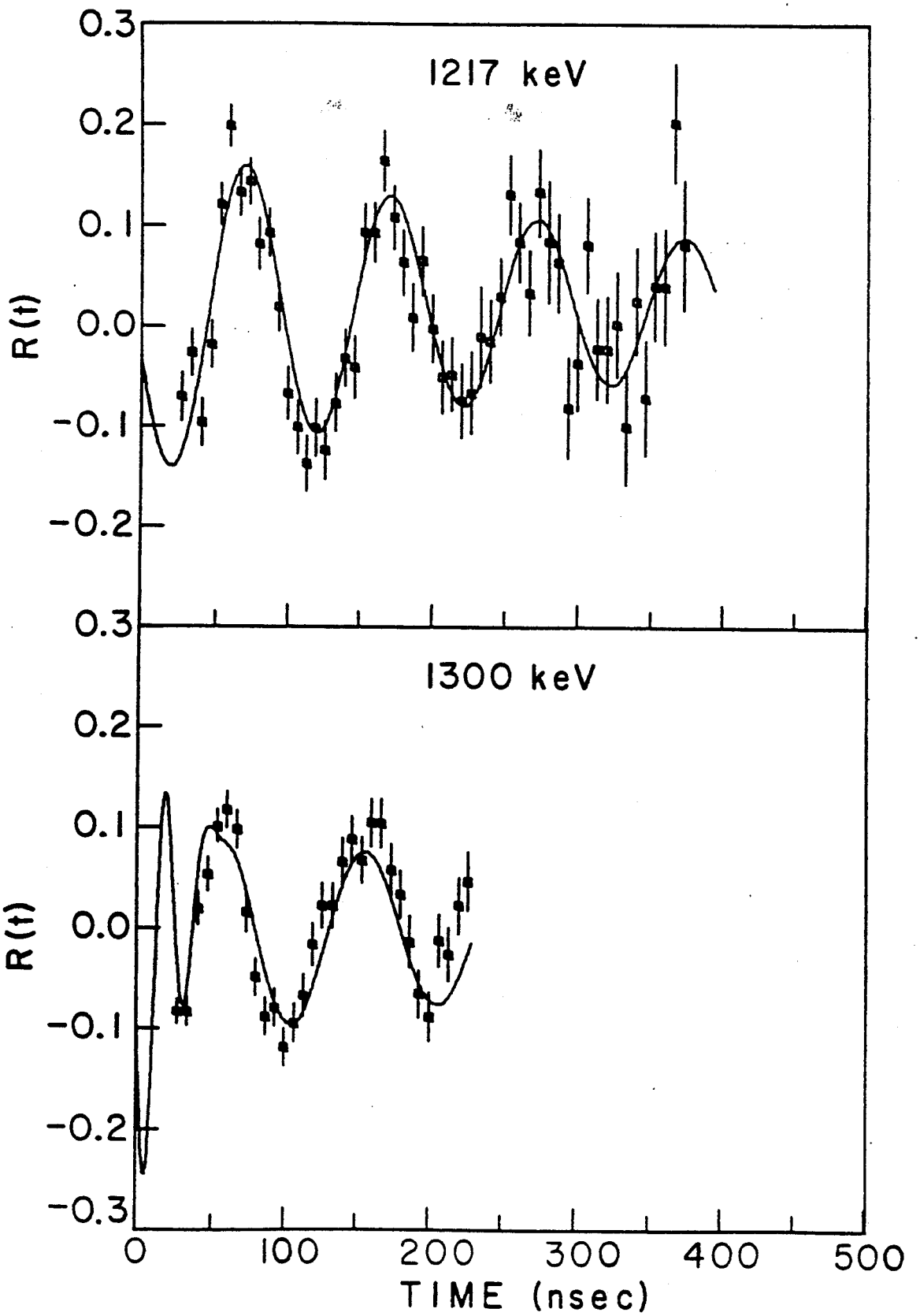

Figure 4-4. R(t) for the 1217 and 1300 keV lines in ^{115}Sb.

$$B_k = b_k G_k e^{-\lambda_k t} \tag{29}$$

in Equation (27) contain an exponential decay term with constant λ_k accounting for the relaxation of the alignment. The factors G_k and ϕ_k in Equation (28) arise from the overlap in time of decays from preceding beam bursts and are 1 and 0, respectively, when $t_{1/2} << T$. They are defined as follows:

$$G_k = \frac{1-\beta}{(1-2\beta\beta_k \cos k\omega T+\beta^2\beta_1{}^2)^{1/2}},$$

$$\phi_k = \frac{\beta\beta_k \sin k\omega T}{1-\beta\beta_k \cos k\omega T}, \tag{30}$$

where $\beta = e^{-\lambda T}$ and $\beta_k = e^{-\lambda_k T}$.

The factors b_k in Equation (29) are combinations of A_2 and A_4, the usual anisotropy coefficients,

$$b_0 = \tfrac{1}{4}A_2 + \tfrac{9}{64}A_4, \quad b_2 = \tfrac{3}{4}A_2 + \tfrac{5}{16}A_4, \quad b_4 = \tfrac{35}{64}A_4 \tag{31}$$

The ratio R(t) is then

$$R(t) = \frac{N(1)-N(2)}{N(1)+N(2)}$$

$$= \frac{B_2 \sin(2\omega t - 2\Delta\theta + \phi_2)}{1+B_0 - B_4 \cos(4\omega t - 4\Delta\theta + \phi_4)}. \qquad (32)$$

The data were fit to

$$R(t) = \frac{\frac{3}{4}A_2 e^{-\lambda_2 t} G_2(\omega T)}{1+\frac{1}{4}A_2} \sin[2\omega t - 2\Delta\theta + \phi_2(\omega T)] \qquad (33)$$

by varying the four parameters, A_2, λ_2, ω, and $\Delta\theta$ with a least squares fitting program. The simplifying assumptions, $A_4 = 0$ and $\lambda_0 << \lambda_2$ have been made.

4.2.3. Results

The results of the fit to the TDPAD data are in Table 4-1. The period of oscillation, $T_2 = \pi/\omega$, is 100.7 ns, corresponding to a g-factor of +0.287(4) obtained from the expression $g = -\hbar\omega/B\mu_N$. With the field B "down" and ω in the opposite direction, the g-factor is positive. Statistical errors were carried in the background subtraction of the TAC spectra and the formation of the ratio. Weighted least squares fits to the data were performed.

Table 4-1. Results of the ^{115}Sb g-Factor Analysis.

γ-Ray Energy	$g_{19/2^-}$	$g_{11/2^-}$
1217 keV	0.287(4)[a]	
1300 keV	0.287(4)	1.06(10)

Parameters Determined by Least Squares Fit[b]

1217 keV	1300 keV
$T_\omega = \frac{\pi}{\omega} = -100.7(13)$	$T_{\omega_1} = -100.7(11)$
$\Delta\theta = 0.13(6)$	$T_{\omega_2} = -27.2(6)$
$A_2 = 0.26(3)$	$A_2 = 0.36(6)$
$\lambda_2 = 0.0024(8)$	$\lambda_r = 0.0024(13)$
$C = 0.019(5)$[c]	$C = -0.056(5)$[c]

Constants Used in the 1300 keV Fit

$t_{1/2}^{(1)} = 156(3)$ ns	$\beta = 0.414(3)$	$\Delta\theta = 0.13(6)$	$G_2^{(1)} = 0.903$
$t_{1/2}^{(2)} = 6.2(4)$ ns	$\alpha = 0.7(2)$	$f_1 = 1.11$	

[a] The errors in the results reflect all fit uncertainties as well as magnetic field uncertainties and in the case of the $11/2^-$ g-factor were determined by varying entered parameters as stated in the text.

[b] The errors quoted reflect only statistical errors in the fit. The tabulated g-factor results also reflect the errors associated with the constants used for the 1300 keV fit, as determined from the 1217 keV fit and the 1300 keV sum spectrum fit.

[c] C is an offset constant left as a parameter in the fit. Its only function is to shift the curve vertically to correct for any normalization errors.

The effect of the A_4 term on the derived g-factor can be estimated by including it as a constant in the first equation for R(t). Varying A_4 from 0 to -0.1 changed the g-factor only about +0.1% so no adjustment was made to the final value. The magnetic field at the nucleus is not always the same as the applied field, however. In our case, the Knight shift due to polarization of the s electrons in the metal target increases the field at the nucleus (+0.82%), and the diamagnetic effect decreases the field (-0.6%), resulting in a correction in the measured g-factor that is small (-0.22%) compared to the estimated error [Mo76].

The ratio for the 1300 keV line can also be fit, but is complicated by the presence of the short-lived isomeric state that it depopulates. Nagamiya gives a detailed treatment of this problem [Na74]. The expression we have employed to calculate the intensity ratio of the line depopulating isomer 2 under isomer 1 is

$$R(t) = b_2 N(t)^{-1}[\cos\delta G_2^{(1)} f_1 \beta e^{-\lambda_1 t}\sin(2\omega_1 t+\delta+\phi_2^{(1)}-2\Delta\theta)$$

$$-G_2^{(2)} f_2 \beta e^{-\lambda_2 t}\cos\delta\sin(2\omega_2 t+\delta+\phi_2^{(2)}-2\Delta\theta)+\alpha G_2^{(2)} f_2 e^{-\lambda_2 t}$$

$$\times \sin(2\omega_2 t+\phi_2^{(2)}-2\Delta\theta)], \qquad (34)$$

where

$$N(t) = \beta f_1 e^{-\lambda_1 t} + (\alpha-\beta) f_2 e^{-\lambda_2 t},$$

$$\beta = \lambda_1/(\lambda_2-\lambda_1),$$

$$b_2 = 3A_2 e^{-\lambda_r t}/(4+A_2),$$

$$f_i = (1-e^{-\lambda_i T})^{-1},$$

$$\alpha = N_2/N_1,$$

$$\delta = \tan^{-1}[2(\omega_2-\omega_1)/(\lambda_2-\lambda_1)]. \qquad (35)$$

In the above, λ_i and ω_i are the decay constant and precession frequency for isomer i, λ_r is the decay constant for loss of alignment, α is the intensity ratio of initial population, and $G_2^{(i)}(\omega_i T)$ and $\phi_2^{(i)}(\omega_i T)$ are defined as before. Note β, b_2, and λ_i are defined differently in Equations (34) and (35) than in Equations (28)-(33). The same assumptions made in Equation (33) apply to Equations (34) and (35). In this case, $f_2 \approx G_2^{(2)} \approx 1$, and $\phi_2^{(i)} \sim 0$. The constants α and λ_2 are determined by fitting the sum TAC for the 1300 keV line to N(t) and solving for α and λ_2. These were entered as constants together with f_1, $\Delta\theta$, $G_2^{(1)}$, λ_1, and β and the parameters ω_2, ω_1, A_2, and λ_r were obtained from the best fit. The data for

the 1300 keV line later than about 230 ns after the beam burst were left out of the fit since a small amount of prompt beam leakage associated with the beam sweeper occurred at that time period. The g-factor of the $11/2^-$ isomer obtained from ω_2 is +1.06(10). The error was estimated by varying the constants over an appropriate range and noting the effect on ω_2. The derived g-factor is in agreement with the value +0.97(10) determined by Ketel et al. [Ke78]. The effect of the higher lying 4.0 ns $25/2^+$ state on the measured g-factor was assumed to be negligible due to its short half life and low population, perhaps introducing a small phase shift incorporated in $\Delta\theta$.

4.2.4. Discussion

The expected g-factor for the supposed configuration $[\pi d_{5/2} \otimes \nu h_{11/2} \otimes \nu d_{3/2}]$ for the $19/2^-$ state can be obtained by combining the measured g-factors for the ^{114}Sn 7^- isomer $[\nu h_{11/2} \otimes \nu d_{3/2}]7^-$, g = -0.810(6) with that of the ground state of $^{115}Sb[\pi d_{5/2}]_{5/2}{}^+$, g = 1.384(4) to give $g_{19/2^-}$ = 0.305(3) using the additivity relation (Equation 3). This procedure, however, neglects changes in core polarization due to different configurations. Figure 4-5 shows the suggested configuration of the $19/2^-$ isomer and that of the ground state. The arrows represent

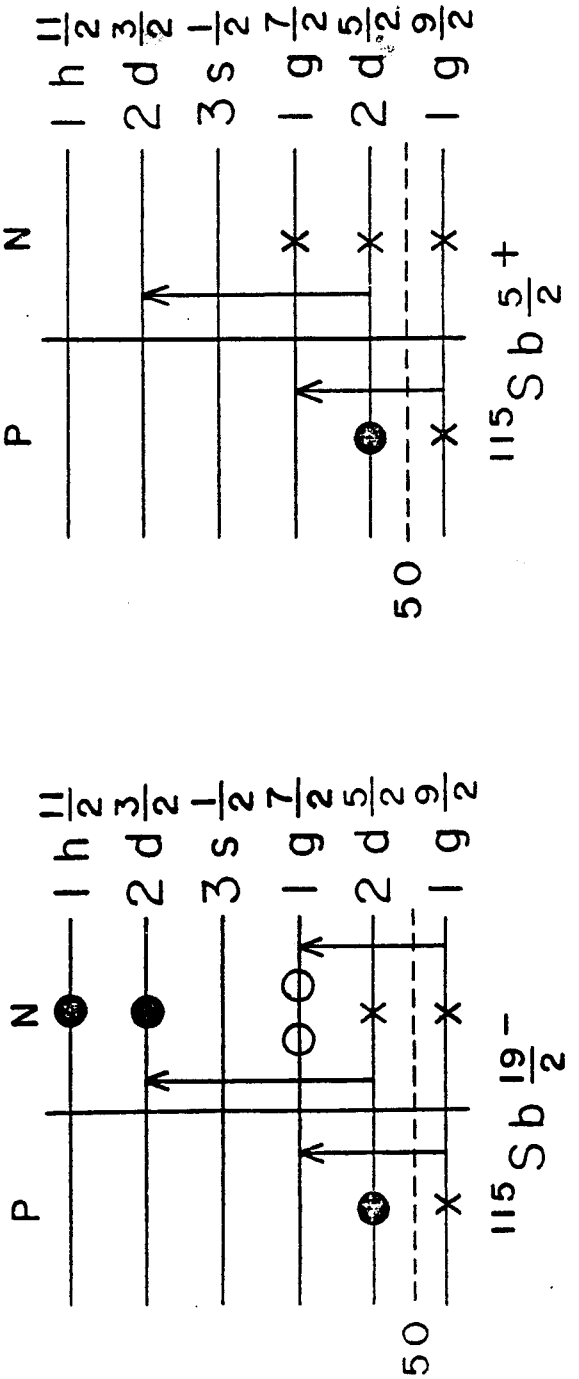

Figure 4-5. Configuration for the $19/2^-$ isomer and the ground state of ^{115}Sb. The arrows represent core polarization excitations. Filled shell-model orbits are indicated with an "x".

excitations corresponding to the core polarization of the neutrons by the odd proton. In the $19/2^-$ configuration the holes in the $g_{7/2}$ orbital allow an extra core polarization over that of the ground state where that orbital is filled. On the other hand, the extra particle in the $d_{3/2}$ orbital causes a blocking in the amount of d-orbital core polarization. The effects cancel each other, suggesting the additivity result should be reasonably accurate. The Arima-Horie formalism [No58] was used to estimate this effect and the result was $g_{19/2^-}$ = 0.293 to 0.313 using a pairing energy C = 30 to 37 MeV. If there were an admixture of $(\pi h_{11/2} \otimes 4^+)$ one would expect the g-factor to be somewhat larger. The measured value, slightly lower than predicted, suggests a relatively pure $[\pi d_{5/2} \otimes \nu h_{11/2} \otimes \nu d_{3/2}]_{19/2^-}$ configuration.

The g-factors of the $19/2^-$ and $11/2^-$ states in ^{115}Sb have recently been measured independently by other labs. T. J. Ketel measured the g-factor of the $11/2^-$ state by TDPAD using a ^{116}Sn(p,2n)^{115}Sb reaction where little or no population of the higher lying $19/2^-$ state occurred [Ke78]. He obtained a g-factor of 0.97(10) and suggested a 50% admixture in the configurations $\pi h_{11/2}$ and $[\pi d_{5/2} \otimes 3^-]$. Shroy, et al. concurrently measured the g-factor for the $19/2^-$ state using a ^{112}Cd(^{6}Li,3n)^{115}Sb reaction and reported it to be g = 0.290(5), in agreement with our measurement but of opposite sign [Sh77]. They have since determined

the sign is actually positive but was quoted wrong due to an error in the phase of the R(t) of a standard used to calibrate the magnetic field [Sh79]. Ketel et al. also published a measurement of the $19/2^-$ state g-factor using the $^{113}In(\alpha,2n)^{115}Sb$ reaction and obtained g = 0.282(6) [Ko79] in agreement with the others.

4.3. g-Factor of the 12^+ State in ^{202}Pb

The MSU-Purdue collaboration has recently obtained γ-ray spectroscopic data in the light Pb region [He77], [Sa77], [Do78]. Many isomers were discovered, some above the 3.6 hour 9^- isomer in ^{202}Pb. The presence of this isomer has made it difficult to observe the higher lying states, but the presumed 20 ns 12^+ state, and two higher lying isomers $t_{1/2}$ = 150 ns and 100 ns have been found (Figure 4-6). The g-factors of the 12^+ states in the even lead isotopes $^{194,196,198,200,206}Pb$ have all been measured [Ro77], [Yo75], [Na72]. The g-factors were found to be -0.158(6), -0.157(7), -0.144(11), -0.157(6), and -0.155(4), respectively. They are all amazingly close together showing little A dependence of the g-factor. The Schmidt g-factor for an $i_{13/2}$ neutron hole state $(i_{13/2})^{-2}$ would be $g_{Schmidt}$ = -0.294 (Equation 4). The large difference between the Schmidt and experimental values can be explained in part by core polarization (Section 2.2).

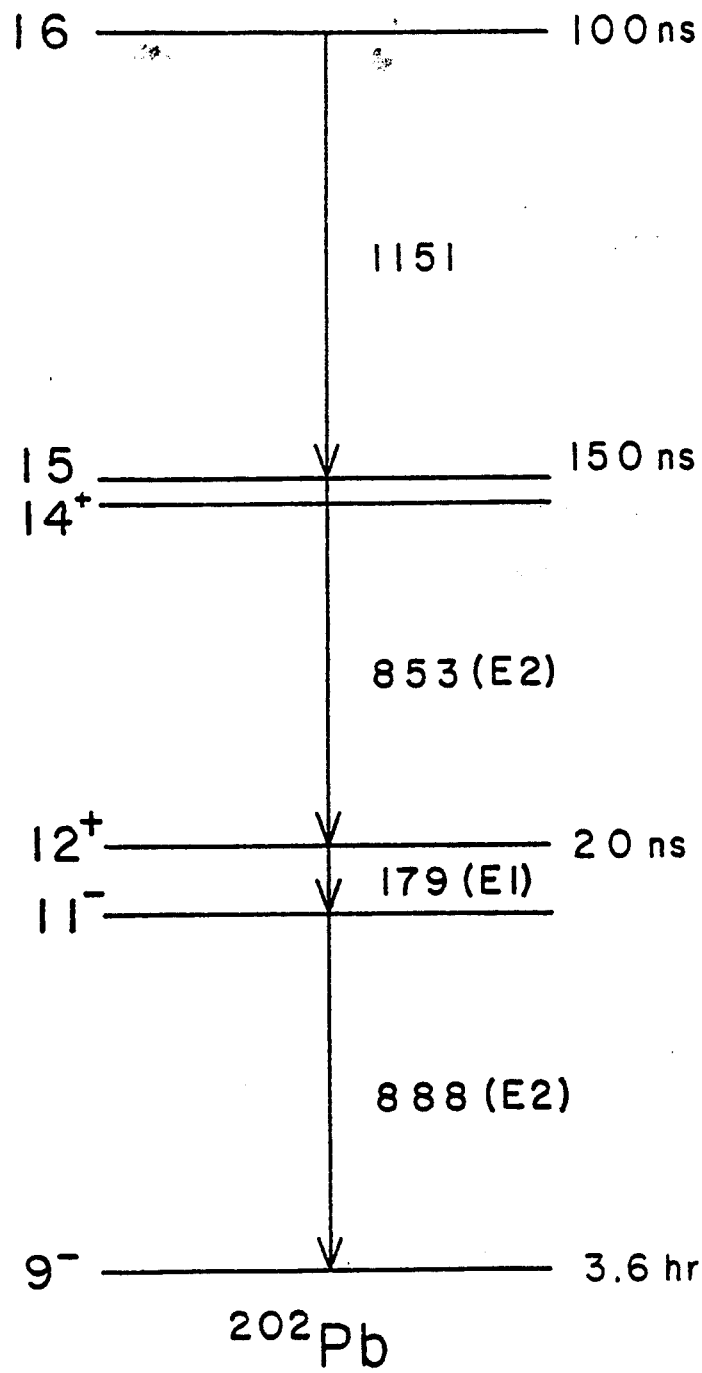

Figure 4-6. Partial ^{202}Pb decay scheme.

Using the Arima-Horie formalism [Ar54] and assuming only core polarization resulting from the $i_{13/2}$, $i_{11/2}$ shells (Figure 2-1a), one obtains $g_{corr} = -0.20$. Core polarization from other levels such as the ($\pi h_{11/2}$, $\pi h_{9/2}$) pair would further reduce the magnitude of the g-factor, but even with all corrections considered the discrepancy is considerable [Ro77]. If one assumes as a first approximation that all the neutron holes are in the $i_{13/2}$ orbit one would expect a decrease in the core polarization as the mass number decreases since the particle number in the $i_{13/2}$ orbit is decreasing. The g-factor would then be predicted to become more negative for the lower mass Pb isomer [LEY]. The effect of other core polarizations (c.p.) may counteract this effect however. A calculation by Roulet et al. [Ro77] shows the ($f_{7/2}$,$f_{5/2}$) excitation compensating the effect of the ($i_{13/2}$, $i_{11/2}$) levels. In this case as the $f_{5/2}$ shell fills, the higher neutron number blocks c.p. excitations to effectively counteract the increased ($i_{13/2}$, $i_{11/2}$) core polarizations.

The experimental method used is similar to that used to take the ^{115}Sb data. Gates were set on the 179 keV, ^{202}Pb, 197 keV, ^{19}F, 222 keV, ^{201}Pb, and 258 keV ^{203}Pb lines, and a background gate on the high energy side of each. A 48 MeV alpha beam was used to induce (α,xn) reactions on a thick 1/16" natural liquid Hg target. It is estimated from the natural abundance of the Hg isotopes

and the cross sections from the program CS8N [CS8N] that about 27% of the reaction goes into the production of ^{202}Pb at 48 MeV. Another peak in ^{202}Pb production occurs at 30 MeV, where 27% of the cross section produces ^{202}Pb. Since the target is thick enough to stop the beam, however, there will be lower energy components of the beam present that will result in a shift in production toward higher mass isotopes. Figure 4-7 shows a spectrum of delayed γ-rays from this reaction.

About 13 hours of data were collected at a magnetic field of 22.7 kgauss. One out of eleven beam bursts were selected by the sweeper, providing 526 ns between beam bursts. The relaxation time of Pb in liquid Hg is greater than 100 μsec [Qu69]. No relaxation should take place before the isomers decay. Figure 4-8 shows the final background subtracted TAC spectra and the ratio R(t) for the 179 keV line. Fitting the equation to a simple sine function (Equation 22) including a phase shift, Δθ, and assuming a negative A_2 for the 179 keV E1 transition, one obtains $A_2 = -0.10(2)$ $t_\omega = 207(25)$ ns and $\Delta\theta = 0.28(29)$. The phase shift Δθ is close to what one would expect from beam bending.) The g-factor from Equation (26) is then

$$g = \frac{-655.9}{22.7\text{kg}\cdot 207\text{ns}} = -0.14(2)$$

close to the g-factors of the other measured 12^+ isomers.

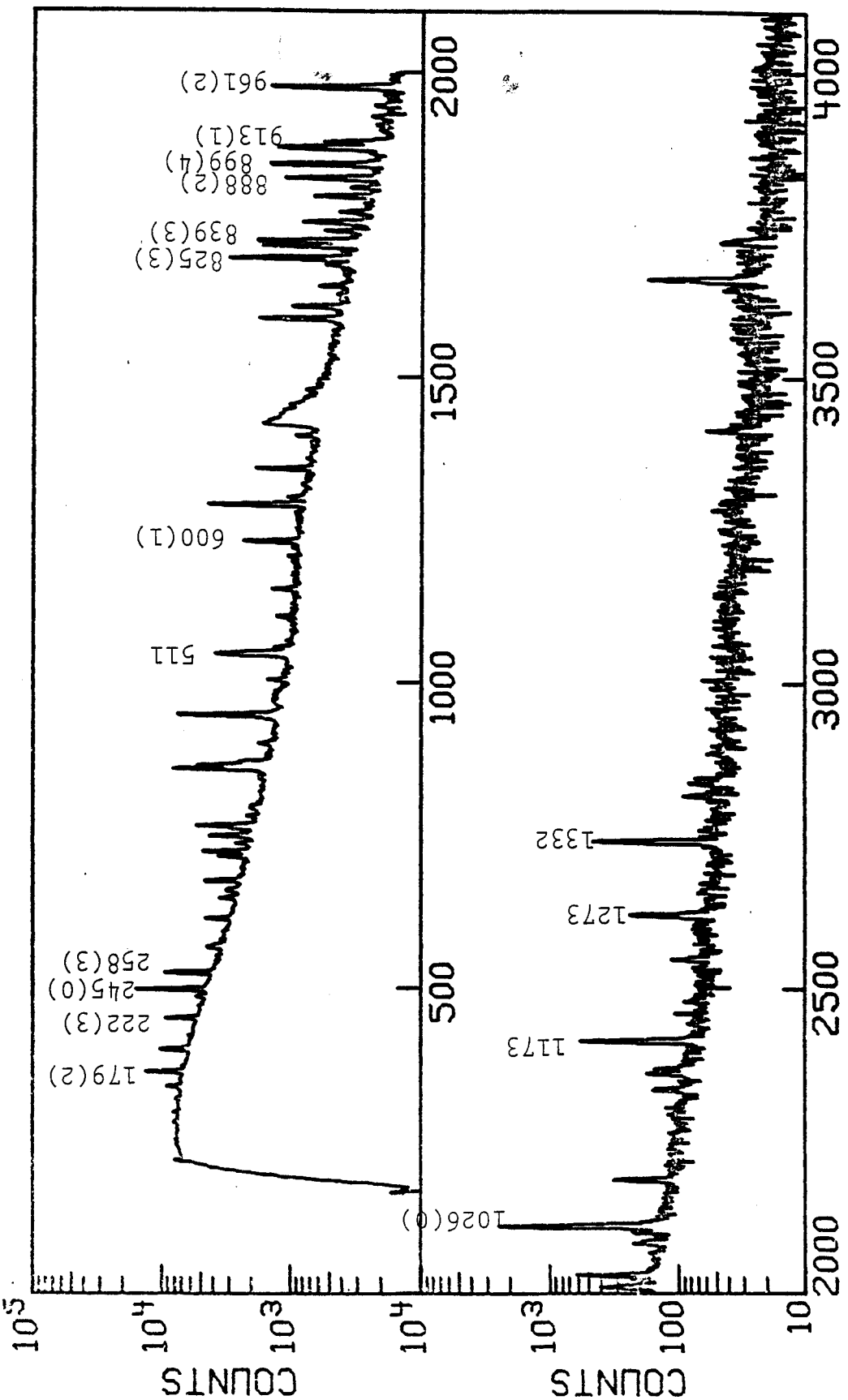

Figure 4-7. Delayed γ's from 48 MeV α's on Hg.

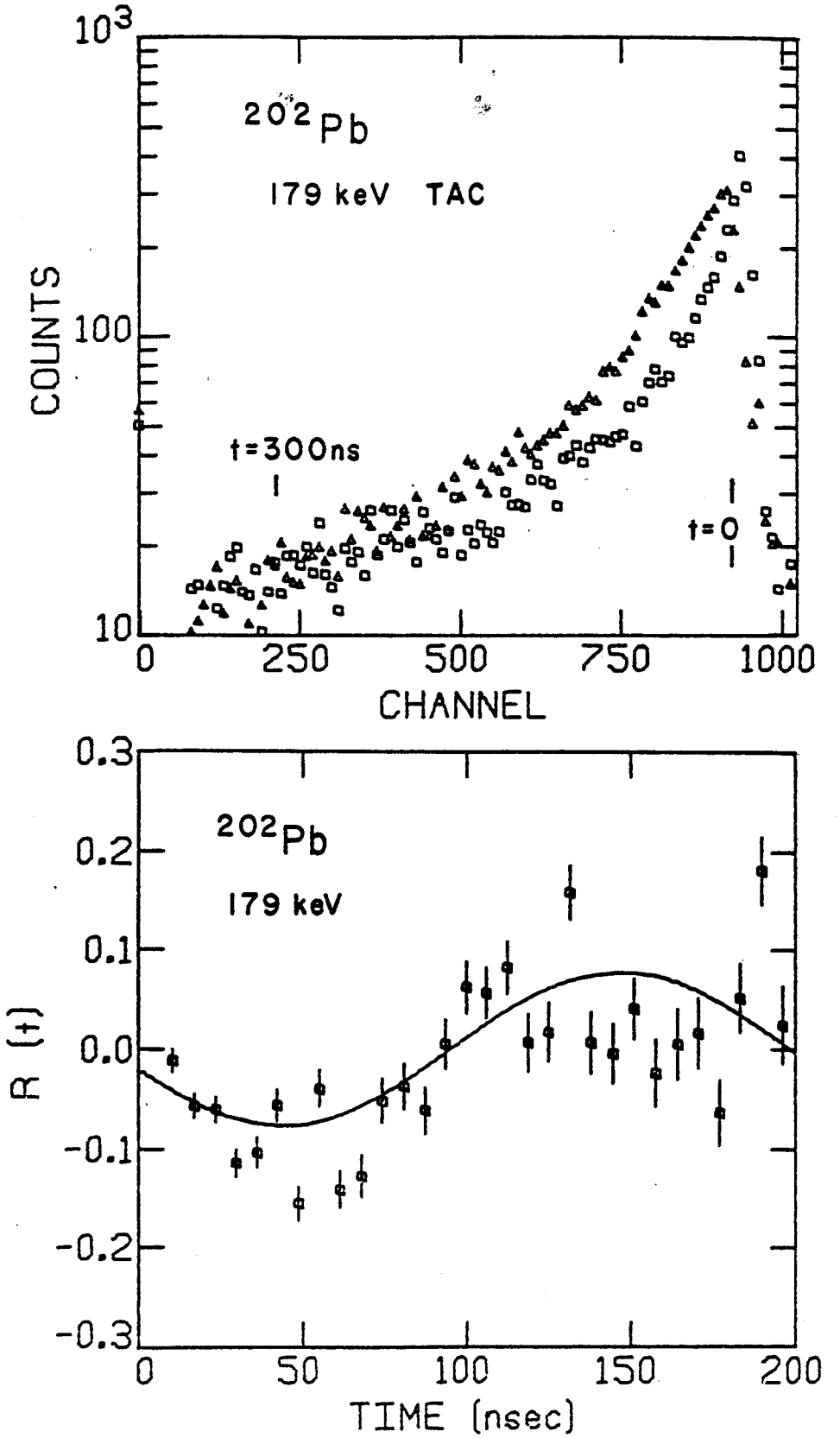

Figure 4-8. ^{202}Pb TAC spectra and ratio (R(t)) for the 179 keV transition Δ indicate -135°, □ indicate +135° detector angle.

There exist, however, two isomers above the 20 ns 12^+ isomer as can be seen from the longer $t_{1/2}$ components in the 179 keV TAC spectrum and in coincidence data obtained on this nucleus. The effect of these isomers on the PAD pattern is not known, but from the size of the 20 ns TAC peak one can conclude that the prompt feeding of the 12^+ level is significant, indicating that the g-factor extracted mostly reflects the 12^+ isomer.

Of the other lines observed, only the 258 keV $21/2^+$ $17/2^+$ transition in ^{203}Pb showed any hint of precession in the TAC spectra (Figure 4-9). The difference in the spectra between the two detectors is small but shows indication of a positive g-factor, assuming a positive A_2 for the 258 keV E2 transition. Theoretically the $21/2^+$ 42 ns isomer in ^{203}Pb is thought to be $(^{204}\text{Pb}\ 4^+ \otimes i_{13/2}{}^{-1})_{21/2^+}$ [Sa77]. Combining the effective g-factor of an $i_{13/2}$ neutron hole g = -0.157(6) (from ^{200}Pb) [Yo75] and the measured g-factor of the ^{204}Pb 4^+ 1274 keV level (260 ns $t_{1/2}$) g = +0.057(20) [Sa63] using additivity (Equation 3) one obtains g = -0.032(16). This g-factor is close to zero, but a measurable positive g-factor would be unexpected.

Another experiment was attempted with the same reaction using data taking method in Figure 3-2b, without the scale-down of prompt events. Timing SCA's were used to try and cut down the spectrum in uninteresting areas to reduce

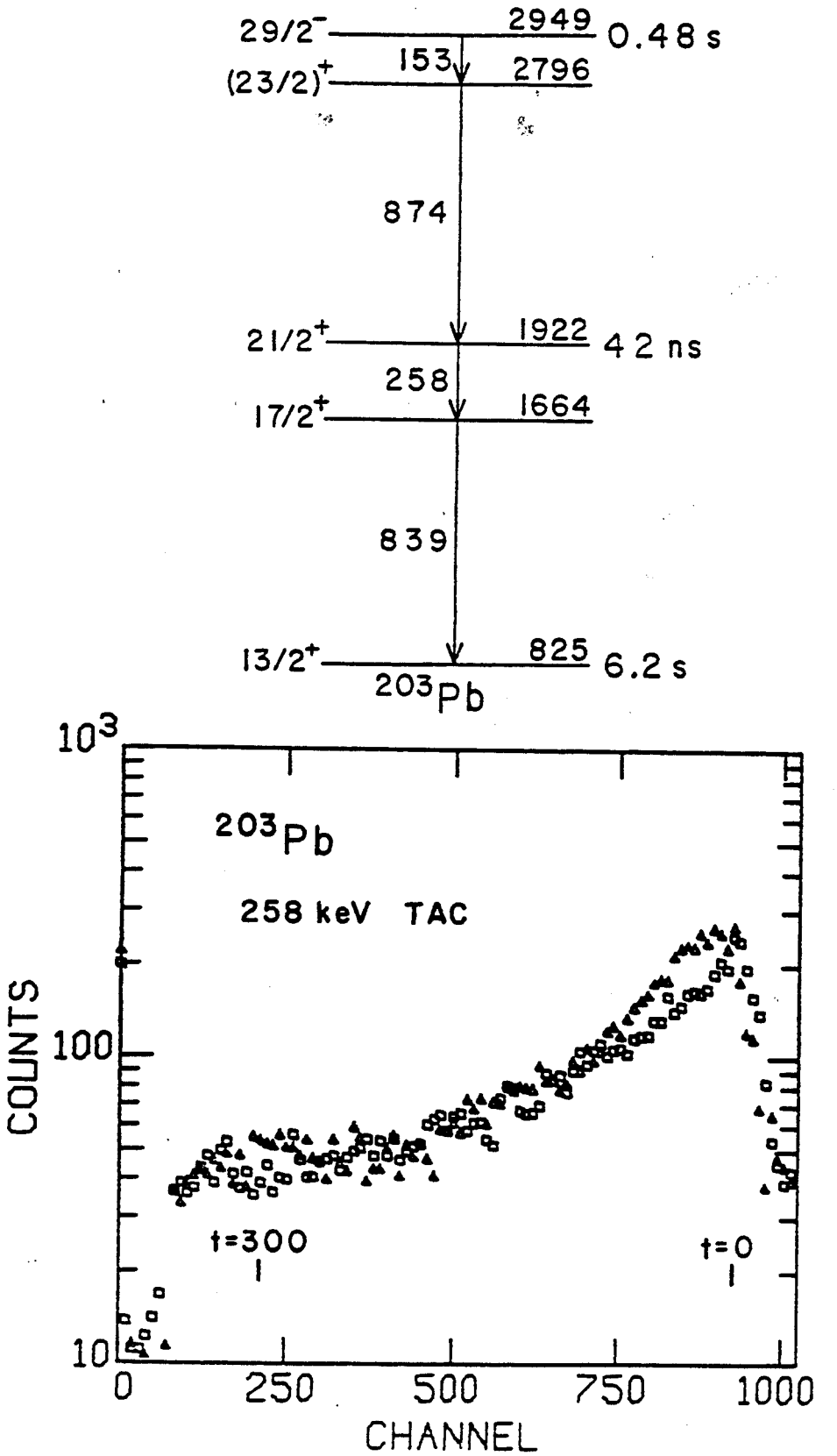

Figure 4-9. ^{203}Pb partial level scheme and TAC spectra. Δ = -135° spectrum; □ = +135° spectrum.

the count rate. The program IIEVENT was then used to collect data on tape. The TAC spectra for the 179, 222, 258, 600, 839, and 888 keV lines in ^{202}Pb, ^{201}Pb, ^{203}Pb, ^{201}Pb, ^{203}Pb, and ^{202}Pb, respectively, were sorted from the 16 tapes collected. The effective counting rate was quite low ($\sim$1 khz), limited by the tape collection method, and the statistics obtained were quite poor. The 222 and 600 lines had very poor statistics, the 179 and 258 lines were added to the previous data and the 839 and 888 lines showed no hint of precession taking place.

To improve these types of experiments a flowing or replaceable Hg target should be used, since the activity built up by the long lived 9^- isomers in 202, 204 Pb increase the background considerably after about an hour. A 30 MeV beam could also be used so less high spin isomer population would occur to possibly interfere with the 12^+ ^{202}Pb precession pattern.

Work was started on developing a flowing Hg target. The design consisted of a normal target frame backed with a 1/8in. thick piece of Al into which two polystyrene capillaries entered, top and bottom. The back plate must be glued on using a suitable epoxy that sticks to Al (not 5 min type). The capillaries run through the plastic beam port window (use of hypodermic needles glued in the window may be helpful) to the Hg reservoirs. The Hg is dripped under the action of gravity into a shielded

receiving bottle. The most suitable window material for the target proved to be 1 mil polystyrene, held on with cyanoacrylate "super glue", although it is not clear whether it can take prolonged exposure to greater than one atmosphere pressure for a sustained period. The Hg reservoirs may have to be evacuated to relieve this problem.

4.4. Conclusion

In conclusion, this system works quite well for measuring g-factors of suitable isomers using an (α,xn) reaction. The use of 50 MeV protons has been attempted in the measurement of a 10^- isomer in ^{190}Pt using the $^{193}Ir(p,4n)^{190}Pt$ reaction. The protons produced an excessive neutron flux background, especially when the beam struck parts of the chamber. The Pb lining tends to become activated quickly producing long-lived activity. Alpha particles and heavy ions are much nicer in this respect. When planning an experiment it is important to consider the target material in light of previous discussions on relaxation. It may also be advisable to do an experiment in a goniometer first to prove the feasibility of the experiment in terms of angular distribution and intensity before one attempts the use of the more difficult g-factor apparatus (in cases where little is known of the reaction). Summary of the measured g-factors is given in Table 4-2.

Table 4-2. Summary of Measured g-Factors.

Nucleus	Spin	g-Factor	$t_{1/2}$	Configuration
^{115}Sb	$19/2^-$	0.287(4)	156(3) ns	$\pi d_{5/2} \otimes \nu h_{11/2} \otimes \nu d_{3/2}$
	$11/2^-$	1.06(10)	6.2(4) ns	$\pi h_{11/2} \otimes [\pi d_{5/2} \otimes 3^-]$
^{202}Pb	12^+	-0.14(2)	20 ns	$(\nu i_{13/2})^{-2}$
^{203}Pb	$21/2^+$	Positive?	42 ns	^{204}Pb $4^+ \otimes i_{13/2}^{-1}$?

PART 2

HIGH SPIN STATES IN ^{180}W FROM THE $^{180}Hf(\alpha,4n\gamma)^{180}W$ REACTION

V. INTRODUCTION

Recently much research has been done by our group and by others on the Hf and W isotopes. They have been found to yield interesting information about the "backbending" phenomenon [Be76] and display the first observable 4-quasi-particle high K isomers [Kh75]. The nucleus ^{180}W being amongst these isotopes and an isotone of the fruitful ^{178}Hf was chosen for study of the high spin states using an (α,4n) reaction. The MSU facility provided the rare combination of equipment to make this project possible; a cyclotron capable of providing a pulsed beam of 45-50 MeV alphas with good timing and the necessary data taking equipment and data analyzing computer.

Previous work included decay studies of levels in ^{180}W from ^{180}Re ([Ho67],[Go67] and [Ha68]) which showed the first 3 members of the ground band and the first two members of the 2^- band. An (α,2n) reaction study showed the 8^- isomer in ^{180}W and other nuclei [Bu66]. An (α,4n) reaction done long ago with NaI (Tl) detectors showed the ground band to spin 12 [La65]. Some work was done using the (p,2n) reaction observing γ's and conversion electrons but the data quality and difficulties involved lead to a questionable level scheme [Gr66]. Recently in beam γ work done concurrently with this work using the (p,2n)

reaction has confirmed the low spin portion of this work [Ma79]. The present study investigates high spin states by the $^{180}Hf(\alpha,4n)^{180}W$ reaction using modern high resolution Ge(Li) gamma-ray detectors and high speed computers for analysis, enabling more information to be gained than heretofore possible. The following discussion will include some of the relevent theory, a description of the experiments performed, and the results obtained.

VI. THEORY

6.1. Deformed Nuclei

The problem of developing a quantitative nuclear model is much more complicated in many ways than that for an atom. In the nucleus one doesn't have a central force problem such as that for the atom. The nuclear force is a strong short range interaction and the nucleus is more like a particle in a box problem. One can approximate the nuclear force in terms of a square well or harmonic oscillator potential, fill it with spin 1/2 nucleons with orbital angular momentum ℓ and obtain a series of possible energy levels. If spin-orbit coupling is included (M. G. Mayer) [Ma50], a nuclear shell model results that predicts the observed "magic numbers" or closed shells observed for nuclei. Excited nuclear states near closed shells can also be explained in terms of these orbitals. When one observes nuclei with many valence particles, far from closed shells things change rapidly and the spherical shell model doesn't work as well. Measurements of quadrupole moments of these nuclei suggest that they are non-spherical. Nuclei in the rare-earth region Er, Yb, even through W show large deformations usually a prolate shape with $\beta \approx 0.3$ ($\beta = \frac{\text{major axis - minor axis}}{\text{average of the axes of the ellipsoid}}$). The energy

levels of these nuclei can be separated into groups that correspond to rotational bands similar to those seen in molecular spectra. The energy levels obey the relation $E = \frac{\hbar^2}{2\mathcal{J}} I(I+1)$ where I is the sum of the particle angular momentum $\vec{j}$ and the rotational angular momentum $\vec{R}$ (see Figure 6-1). The unpaired nucleons traveling around the deformed core have intrinsic spin $\vec{S} = \pm\frac{1}{2}$, orbital angular momentum $\vec{\ell}$ and total angular momentum $\vec{j}$. Consider a nucleus rotating about the 2 axis with angular velocity ω. The projections of the angular momentum vectors on the symmetry axis (3) for $\vec{\ell}$, $\vec{S}$, $\vec{j}$, and $\vec{I}$ are Λ, Σ, Ω, and K, respectively. For an axially symmetric core $\vec{R}$ is parallel to Z so $\Omega = K$. These considerations are the basis of a model explaining deformed nuclei behavior, the Nilsson model.

6.2. The Hamiltonian

The Hamiltonian for deformed nucleus can be broken up into a part describing the energy of the rotating nucleons as a whole (collective motion) and the energy of the particle configurations in the deformed potential on which the rotational bands are based (intrinsic motion). For a single valence particle it can be written:

$$H = H_{rot} + H_{int}$$

$$H_{rot} = \frac{\hbar^2}{2\mathcal{I}} \langle R \rangle^2 = \frac{\hbar^2}{2\mathcal{I}}\{(I_1-j_1)^2 + (I_2-j_2)^2\}$$

$$= \frac{\hbar^2}{2\mathcal{I}} (I^2-I_3^2) + \frac{\hbar^2}{2\mathcal{I}} (j^2-j_3^2) + H_c \qquad (36)$$

where

$$H_c = - \frac{h^2}{2\mathcal{I}} (I_+j_- + I_-j_+)$$

H_c corresponds to the classical Coriolis force $\vec{F} = -\vec{\omega}x\vec{p}$, exerted on a particle momentum p in a rotating system with angular velocity $\vec{\omega}$. This force tends to orient the angular momentum vector along $\vec{\omega}$. The wavefunction for a particle moving in a deformed system is characterized by the quantum number Ω and a linear combination of spherical states $\psi_{j\Omega}$ [Mo76].

$$\chi_\Omega = \sum_j C_{j\Omega} \psi_{j\Omega} \qquad (37)$$

Each rotational band can be characterized by its projection quantum number K which is a function of the intrinsic configuration of the nucleus. The Coriolis force mixes bands with $\Delta K = \pm 1$. For a single particle the non-diagonal matrix element is:

$$\langle K,I|H_{rot}|K\pm1,I\rangle = -A\langle K|j^{\mp}|K\pm1\rangle \sqrt{(I\mp K)(I\pm K+1)} \qquad (38)$$

where

$$\langle K|j^{\mp}|K\pm1\rangle = \sum_j C_{jK}C_{jK\pm1} \sqrt{(j\mp K)(j\pm K+1)}$$

The diagonal rotational energy is:

$$E_I = A\{I(I+1)-K^2 + \delta_{K,1/2}\, a(-)^{I+1/2}(I+\tfrac{1}{2})\} \qquad (39)$$

where a is called the decoupling parameter:

$$a = -\langle \Omega = \tfrac{1}{2}|j+|\Omega = -\tfrac{1}{2}\rangle = \sum_j (-)^{j-1/2}(j+\tfrac{1}{2})|C_{j1/2}|^2 \qquad (40)$$

The Coriolis mixing is usually small because the $C_{j\Omega}$ coefficients are small. The exceptions are when high j unique parity spherical orbitals are involved ($h_{11/2}$, $i_{13/2}\ldots$). In these $C_{j\Omega} = 1$ because there are no other states to be mixed, and high j and low Ω leads to increased Coriolis mixing.

6.3. Nilsson Model

The Nilsson model is a description of the splitting of the spherical shell model states as a function of nuclear deformation [Ni55]. The Hamiltonian for the single particle problem is

$$H_o + 2\kappa\hbar\omega(\vec{\ell}\cdot\vec{s} - \mu\ell^2). \qquad (41)$$

H_o is the deformed harmonic oscillator potential part of which depends on the deformation. The parameters κ and μ are adjusted to reproduce observed level schemes of rare earth nuclei. The wavefunctions are linear combinations of cylindrical harmonic oscillator functions. Due to the lack of spherical symmetry j is not a good quantum number, but $j_z = \Omega$ is. The eigenfunctions for each Ω are composed of a sum of terms characterized by N, ℓ, Λ, and Σ, where N is the number of oscillator quanta involved (the

other quantities are shown in Figure 6-1). On a Nilsson orbital diagram the energy of the eigenstates are plotted as a function of deformation, see [Le68]. Each Nilsson orbital can hold 2 nucleons and is labeled with the asymptotic quantum numbers $\Omega^{\pi}[Nn_z\Lambda]$ where n_z is the number of nodes along the symmetry axis. The energy levels can be calculated as a function of both quadrupole (ε_2) and hexadecapole (ε_4) deformation. The quadrupole deformation was estimated for ^{180}W from the formula in Stelson and Grodzins [St65]

$$\varepsilon_2 \cong \beta_2 = B(E2)^{1/2} \left[\frac{4\pi}{3ZR_o^2}\right] \qquad (42)$$

The B(E2) was calculated from the lifetime of the $2^+ \rightarrow 0^+$ transition (see Section 8.3). R_o is the radius of the nucleus $R_o = 1.2 \times 10^{-13} A^{1/3}$ cm. The parameters used and the final result of the Nilsson calculation are given in Figure 6-2 for both protons and neutrons. The Fermi surface was placed somewhat arbitrarily half way between the last "filled" orbital and the nearest "unfilled". The Fermi surface (λ) is given a value of zero on the energy scale. On the basis of these orbitals one can predict the energy and spins of possible intrinsic states for ^{180}W, but first a word about pairing.

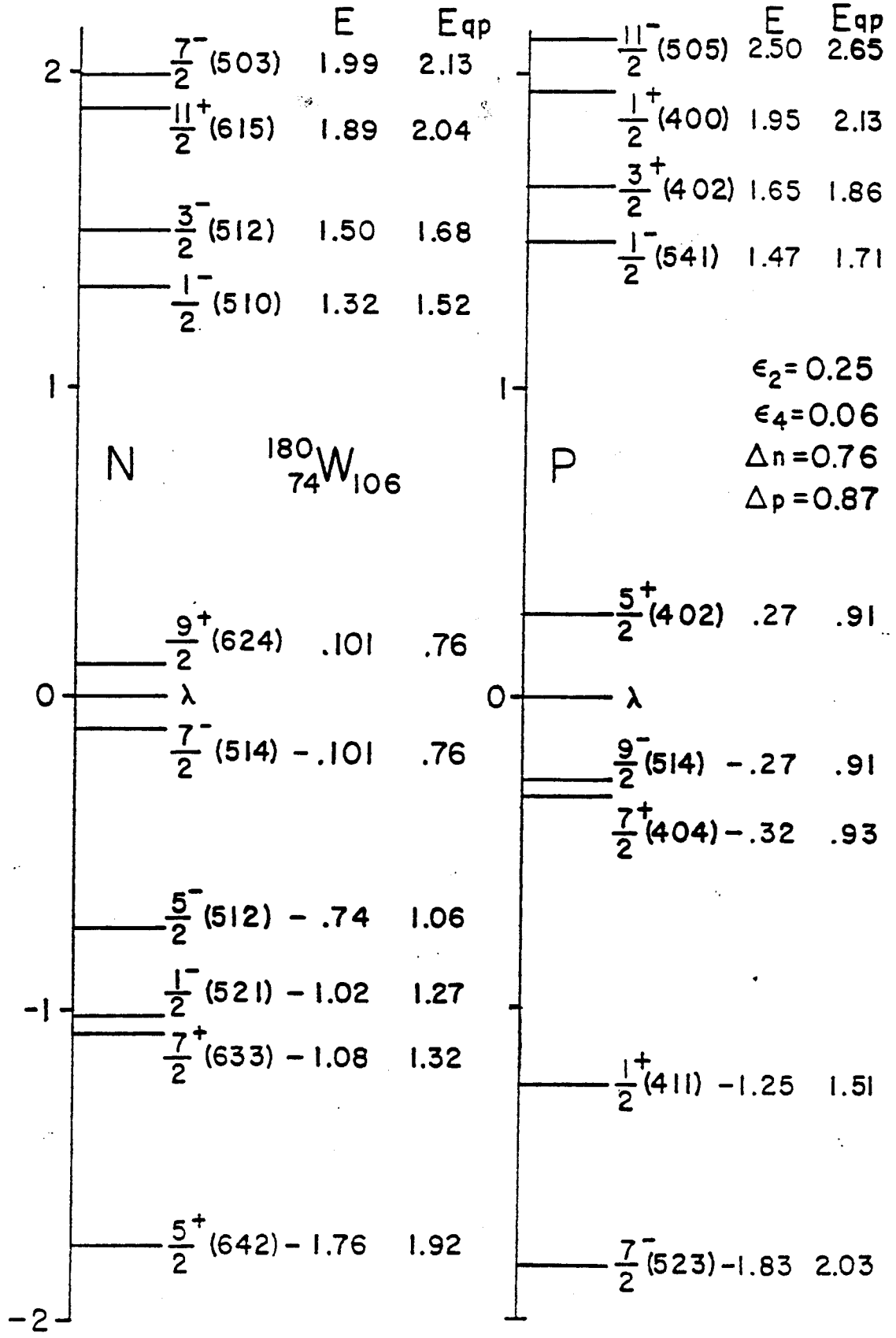

Figure 6-2. Nilsson diagram showing quasiparticle energies.

6.4. Pairing Correlations

Nucleons which occupy identical but time reversed (opposite m_j) orbitals interact with each other through a pairing force. The cumulative effect of this interaction lowers the energy levels below the values predicted from the pure intrinsic calculation given above. The interaction is similar to that in an electron gas in the theory of superconductivity by Bardeen, Cooper, and Schrieffer (BCS) [Ba57]. The nucleus can be viewed as a Fermi gas also where each orbital has a certain probability of being occupied at a given time with the average occupation level being at the Fermi surface. The occupation probability parameters for holes (v_K^2) and particles (μ_K^2) is given by:

$$\left.\begin{matrix}\mu_K^2 \\ v_K^2\end{matrix}\right\} = \frac{1}{2}\left[1 \pm \frac{(E_{sp}-\lambda)}{E_{qp}}\right] \qquad (43)$$

These are called quasiparticle excitations and E_{qp} is the quasiparticle energy. E_{qp} can be found from the formula:

$$E_{qp} = \sqrt{(E_{sp} - \lambda)^2 + \Delta^2} \qquad (44)$$

where Δ is the pairing gap parameter [Og71]. The pairing

gap 2Δ can be obtained from the odd-even mass differences. The value Δ is larger for protons than neutrons. The values used for ^{180}W were obtained from an empirical formula derived by Nilsson [Ni69]. The quasiparticle energies and parameter values are listed in Figure 6-2. For an even-even nucleus the excitations observed are even quasiparticle excitations obtained by simply adding the quasiparticle energies for the orbitals involved. For an odd A nucleus, the ground state is a single quasiparticle excitation with higher lying 3-quasiparticle states, etc. A list of 2 and 4-quasiparticle states possible for ^{180}W and their energies is given in Table 6-1. Each of these excitations could be expected to be the basis of a rotational band with K isomerism displayed (that is the bandhead may decay with a long lifetime due to $\Delta K \neq 0$ forbidden interband transition).

6.5. Collective Phenomena

In even-even nuclei the lowest excited states will be those in the rotational band built on the ground state. The lowest intrinsic excitations will be two-quasiparticle levels separated from the ground state by an energy about 2Δ. There are other excitations possible, however, other than just the quasiparticle configurations and their rotational bands. Collective vibrations are possible which may lie lower in energy than the 2-quasiparticle levels. These

Table 6-1. Some Possible Multiquasiparticle States in ^{180}W.

K^π	Configuration		Energy	g_K
2-Quasiparticle States				
8^-	$\frac{9}{2}^+[624\uparrow]_n$	$\frac{7}{2}^-[514\downarrow]_n$	1.52	0
6^+	$\frac{7}{2}^-[514\downarrow]_n$	$\frac{5}{2}^-[512\uparrow]_n$	1.82	0
7^-	$\frac{5}{2}^+[402\uparrow]_p$	$\frac{9}{2}^-[514\uparrow]_p$	1.82	1.34
7^-	$\frac{5}{2}^-[512\uparrow]_n$	$\frac{9}{2}^+[624\uparrow]_n$	1.82	-0.33
8^-	$\frac{7}{2}^+[404\downarrow]_p$	$\frac{9}{2}^-[514\uparrow]_p$	1.84	1
6^+	$\frac{7}{2}^+[404\downarrow]_p$	$\frac{5}{2}^+[402\uparrow]_p$	1.84	1
4^+	$\frac{1}{2}^-[521\downarrow]_n$	$\frac{7}{2}^-[514\downarrow]_n$	2.03*	-0.58
5^-	$\frac{1}{22}^-[521\downarrow]_n$	$\frac{9}{2}^+[624\uparrow]_n$	2.03*	0
5^-	$\frac{1}{2}^-[510\uparrow]_n$	$\frac{9}{2}^+[624\uparrow]_n$	2.28	-0.46
4-Quasiparticle States				
15^+	8^-_n	7^-_p	3.34	0.63
14^-	8^-_n	6^+_p	3.36	.5
16^+	8^-_n	8^-_p	3.36	.5
13^-	6^+_n	7^-_p	3.64	0.72
14^+	7^-_n	7^-_p	3.64	.5
14^-	6^+_n	8^-_p	3.66	.5
12^+	6^+_n	6^+_p	3.66	.5
15^+	6^-_n	8^-_p	3.66	0.37
13^-	7^-_n	6^+_p	3.66	0.28

*Probably not realistic because the $\frac{1}{2}^-[521\downarrow]_n$ orbital is at a lower energy experimentally as evident in ^{179}W.

vibrational states may also have rotational bands built on them. Some of the lowest energy modes seen in even-even rare-earth deformed region nuclei are the following:

1. β vibration - the elongated ends vibrate in and out keeping a circular cross section. It has zero angular momentum along the symmetry axis.

2. γ vibration - Similar to the β vibration but the cross section becomes eliptical. It carries 2 units of angular momentum along the symmetry axis.

3. Octupole vibration - This excitation carries 0-3 units of angular momentum along the symmetry axis, has odd parity, and oscillates about a 3 lobe shaped cross section.

These vibrations may contain one or more units of vibrational quanta (phonons). The lowest energy modes will be single phonon states. Higher energy bands based on multiple phonon excitations are also possible.

In summary, the energy levels in a deformed nucleus are made up of rotational bands of I(I+1) spacing that are built on intrinsic quasiparticle states (derived from Nilsson type orbitals) or collective vibrations. The Coriolis force may introduce mixing between bands or cause anomolies at high spins which are reflected in the level scheme.

VII. ^{180}W EXPERIMENTAL DETERMINATIONS

7.1. Singles Spectra

The ^{180}W nuclei were produced by bombarding a thin $\sim$1 mg/cm^2 foil of ^{180}Hf with 48-50 MeV α particles resulting in the reaction ^{180}Hf(α,4n)^{180}W. The target was a self supporting metal foil made by sputtering techniques at Niels Bohr Institute in Copenhagen by G. Sletten [Sl72]. In later experiments (all but the first timing experiments) the target material remaining from the broken target was remounted on formvar. The spectra were fairly clean consisting of the (α,4n) reaction, some (α,5n) and (α,3n) contamination as well as some ^{18,19}F production due to the oxide existing on the target. The program CS8N [CS8N] was used to calculate excitation function for the (α,xn) reactions. It predicted maximum production at 47-48 MeV which were the energies used in all experiments except for the prompt coincidence experiment where 49.4 MeV α's were used to favor the high-spin states. The singles spectra were taken in a goniometer at 125° and counted with and without ^{75}Se and ^{110m}Ag sources as internal standards for energy calibration. An 8% efficient Ge(Li) detector (Edax) with FWHM of 2.0 keV at 1332 keV was used

to take the spectra. A copper-cadmium absorber was used to cut the X-ray intensity. The data were analyzed using the γ-ray peak fitting program SAMPO [Ro69] and the interactive version TVSAMPO as adapted by Clare Morgan. The relative efficiency of the detector was determined by analyzing spectra of the standard sources ^{166m}Ho and ^{75}Se using the standard relative efficiencies as determined in reference [Ge77]. The density of lines is quite high; about 150 peaks were fit, almost all at an energy under 600 keV. The spectrum is shown in Figure 7-1 and a list of the peaks, energies, intensities and angular distribution coefficients (mentioned later) is given in Table 7-1. The efficiency curve accuracy is poorer than indicated below 80 keV due to the absence of calibration points. The energy calibration accuracy is around 0.1 keV.

7.2. Angular Distributions

In an in-beam nuclear reaction the product nuclei are aligned in a plane perpendicular to the beam. The γ-radiation is emitted in a preferred direction yielding an angular distribution as mentioned in Section 3-1. The experiment was performed by moving the detector about the target in the goniometer arm and counting for an hour and 15 minutes at each angle. Seven angles were done: 90°, 105°, 115°, 125°, 135°, 145°, and 155°. The spectra were

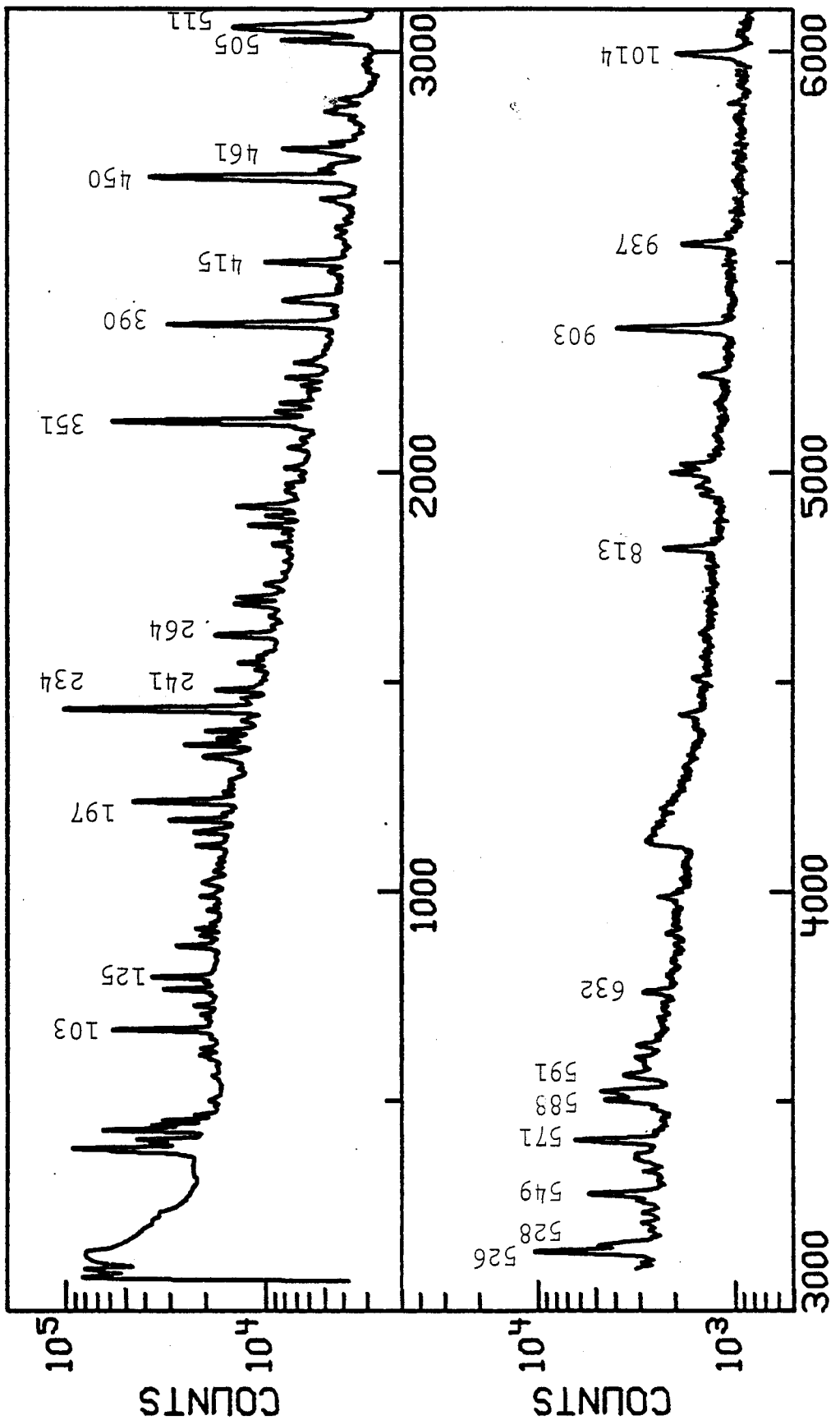

Figure 7-1. γ-rays from the $^{180}Hf(\alpha,4n)^{180}W$ reaction (48 MeV α).

Table 7-1. γ-Rays in the $^{180}Hf(\alpha,4n\gamma)^{180}W$ Reaction.

E_γ (keV)	Nucleus	I_γ (rel. int.)	A_2	A_4
71.2		0.27(15)		
72.8		0.74(10)		
75.0		1.72(12)		
76.1	a	0.77(8)		
83.1		0.26(5)		
84.8		1.25(9)		
87.2		0.26(5)		
88.9		0.51(6)		
91.9	^{181}W	1.92(12)		
93.3	^{180}Hf	3.42(20)		
95.8	^{179}W	3.11(19)	-0.40(3)	-0.10(5)
100.6	^{182}W	0.84(13)	-0.21(7)	0.20(11)
103.6	a	34.0(19)	0.036(13)	-0.007(18)
105.0	^{178}W	0.83(13)		
108.1		1.56(15)	0.17(9)	-0.03(16)
109.9	^{181}W	2.43(19)		
113.4	^{181}W	4.05(23)	-0.314(22)	0.06(3)
118.1		1.07(11)		
119.9	^{179}W	12.4(7)		
122.8	a	2.05(14)	0.24(6)	0.17(9)
125.0*	a	15.7(9)	-0.10(3)	0.03(4)
136.8		1.05(19)	-0.5(4)	0.2(7)
137.7	$^{181}W, ^{179}W$	8.8(5)	-0.43(3)	0.09(6)
139.6		1.07(11)		
142.0	^{174}W	3.79(23)	-0.39(9)	-0.22(12)
144.6	^{179}W	4.18(26)		
146.9	a	1.58(13)	-0.55(7)	0.12(12)
152.3		2.41(14)		
154.3		1.01(7)	0.18(9)	0.03(15)

Table 7-1. Continued.

E_γ (keV)	Nucleus	I_γ (rel. int.)	A_2	A_4
156.1		0.72(6)	0.25(4)	-0.05(7)
158.1	a	4.09(23)		
159.6	^{179}W	1.11(8)	0.09(8)	-0.07(17)
162.5	^{179}W	1.33(15)	-0.18(9)	0.3(2)
163.4	^{181}W	3.03(29)	-0.28(8)	0.23(17)
164.2		1.67(26)		
165.2		1.71(14)	-0.29(9)	-0.08(12)
168.4	^{179}W	1.68(11)	-0.54(7)	0.03(11)
170.1		0.54(7)		
171.3	a	1.21(9)	-0.48(12)	-0.07(20)
173.3		1.15(9)		
175.1		0.29(7)	-0.83(15)	-0.32(27)
178.7*	a	6.0(3)	0.17(3)	0.08(4)
181.5	^{179}W	0.52(7)		
184.2	^{18}F	6.7(4)		
185.2	^{181}W	1.90(14)	-0.59(6)	-0.12(10)
189.1	^{179}W	14.0(8)		
191.4	a	1.50(19)	-0.33(4)	0.05(9)
196.5	a	25.9(15)		
197.3	^{19}F	5.6(5)		
200.4	^{179}W	2.16(15)	-0.22(4)	-0.16(6)
202.5		1.47(10)	-0.28(3)	0.09(4)
204.2	^{179}W	1.50(11)	0.18(6)	0.08(10)
205.4	^{179}W	1.59(12)	-0.44(4)	0.04(6)
209.8		0.36(12)		
213.0	^{179}W	2.18(17)	-0.30(5)	0.01(8)
214.4*	^{179}W	6.6(5)		
215.3	^{180}Hf	4.6(4)		
219.5	a	13.2(8)	-0.47(3)	0.10(5)

Table 7-1. Continued.

E_γ (keV)	Nucleus	I_γ (rel. int.)	A_2	A_4
222.0*	a ^{179}W	5.8(3)		
225.2	a	8.4(5)	0.24(4)	-0.05(6)
229.1	^{182}W	1.83(13)	0.25(11)	-0.12(15)
230.3		0.80(12)		
233.9	a	98.(5)	0.132(18)	0.001(20)
236.9	^{179}W	1.19(18)		
238.3		2.46(21)		
241.8	a	8.5(5)	-0.63(5)	-0.03(7)
243.4	^{179}W	0.97(19)	0.548(8)	-0.32(2)
245.0		0.75(21)	-0.54(14)	0.4(2)
250.0		1.88(12)	0.24(5)	0.00(11)
251.2	^{181}W	0.94(8)	0.34(18)	-0.1(3)
252.9	^{179}W	5.21(29)	-0.16(4)	-0.16(6)
254.7		1.10(12)		
255.5		1.90(14)		
257.0	1.41(9)	0.32(7)	-0.24(9)	
264.0	a	7.9(5)		
264.6	^{179}W	5.4(4)		
268.0		0.92(8)		
271.7	(^{181}W) a	1.54(10)		
273.3		0.61(7)	0.33(11)	-0.3(2)
275.8		2.02(15)	0.49(5)	0.21(8)
276.9	a	7.7(4)	0.26(2)	0.04(3)
279.6	^{179}W	7.1(4)	0.18(3)	-0.05(5)
284.4		1.31(15)		
285.3	a	2.43(19)	-0.46(1)	-0.19(1)
289.7		0.41(5)		
292.7		0.29(7)		
294.5		0.93(8)	0.29(9)	-0.26(15)

Table 7-1. Continued.

E_γ (keV)	Nucleus	I_γ (rel. int.)	A_2	A_4
297.9		0.26(11)		
298.7		0.52(10)		
301.2*	^{181}W,^{179}W	2.96(18)		
303.9		0.80(8)		
306.1	a	1.58(10)	-0.47(6)	0.11(9)
308.9	^{179}W	8.2(5)		
312.7	^{179}W	4.65(28)	0.23(6)	-0.07(8)
316.6	a	11.1(6)	0.34(4)	0.02(6)
318.0	a	0.83(7)	0.46(9)	-0.50(17)
321.1		0.48(7)		
322.6		1.77(13)	0.34(10)	-0.3(2)
323.9		1.44(11)		
325.6		2.61(17)	-0.13(10)	-0.11(20)
328.8		0.75(7)		
332.2	a	3.03(18)		
339.2		0.51(11)		
340.3	a	3.02(20)	0.48(7)	0.13(12)
341.7		0.73(7)		
343.6		1.51(10)		
345.1		0.38(6)		
348.6	^{181}W	2.24(16)		
350.9	a	100.(6)	0.130(11)	0.000(18)
354.2		2.18(18)		
355.0	^{179}W	5.1(4)	0.31(8)	0.03(13)
358.4	^{179}W	5.4(3)	0.26(5)	-0.12(9)
361.0	a	1.01(9)	0.38(6)	0.09(10)
362.8	a	1.44(11)	0.24(5)	0.17(8)
365.6	^{181}W	2.62(17)		
368.9	a	5.4(3)	0.29(2)	0.04(4)

Table 7-1. Continued.

E_γ (keV)	Nucleus	I_γ (rel. int.)	A_2	A_4
373.2		0.37(9)		
375.0	(^{179}W)	4.59(27)	0.35(5)	-0.14(8)
376.9		1.28(11)	0.58(18)	-0.5(3)
386.1		0.50(6)		
390.5	a	58.(3)		
400.1	a	8.7(5)	0.30(3)	-0.03(4)
401.5	^{179}W	5.1(3)	0.27(8)	-0.18(13)
412.2		1.55(12)	0.43(8)	0.06(11)
415.9	a	14.8(8)	0.17(3)	0.00(4)
424.2		0.22(8)		
426.5		1.37(11)		
429.8	^{179}W	1.66(12)		
439.9		1.80(13)		
441.5	^{179}W	4.24(25)	0.29(3)	-0.15(5)
450.0	a	95(5)	0.116(11)	-0.023(16)
453.2	a	4.9(3)	0.29(6)	-0.23(10)
455.3	a	3.47(26)		
459.7	^{179}W	2.88(18)	0.32(6)	-0.12(9)
461.4	a	14.1(8)	0.16(3)	-0.01(4)
464.1	^{179}W	3.86(23)		
466.8	^{179}W	0.73(7)	0.4(4)	
473.7		1.34(12)		
476.7	a	5.3(3)		
478.5	^{179}W	3.71(24)		
482.0	^{181}Ta	3.50(22)		
493.7		0.85(8)	0.39(8)	0.02(13)
496.0		1.24(9)	0.31(7)	-0.13(10)
498.8		0.69(8)	0.39(15)	-0.09(23)
505.9	a	17.1(9)	0.15(3)	-0.04(5)

Table 7-1. Continued.

E_γ (keV)	Nucleus	I_γ (rel. int.)	A_2	A_4
518.6		0.82(14)		
521.3		0.0054(6)		
525.7	a	27.4(16)	0.29(3)	-0.05(5)
528.0	a	7.1(4)		
529.4	a	2.87(26)	0.24(8)	-0.12(15)
534.4		0.80(7)		
537.4		1.39(12)		
541.5	^{179}W	1.53(13)	0.43(14)	-0.04(12)
546.3	a	2.51(16)	0.35(9)	-0.07(5)
549.1	a	11.1(6)	0.17(3)	0.07(5)
550.3		0.56(5)		
558.4		1.41(8)		
562.2		0.81(7)		
563.6		2.36(16)	0.26(6)	0.26(9)
565.3	^{179}W	2.18(15)		
571.3	a	15.5(9)	0.31(4)	-0.012(55)
574.5		0.51(10)		
584.0		0.70)10)		
587.6	a	8.9(5)	0.32(4)	0.02(6)
589.6	a	4.8(3)	0.36(4)	-0.08(6)
591.2	a	9.2(5)	0.13(4)	-0.03(5)
596.6		2.13(20)	0.25(15)	0.07(26)
597.8	a	3.81(27)		
609.7	a	2.80(18)		
631.6		3.61(22)	0.25(5)	-0.02(8)
670.7		2.09(15)	0.16(4)	-0.13(7)
745.0		1.90(14)		
760.0		1.23(9)	0.32(7)	0.39(11)
813.4	a	6.2(3)		

Table 7-1. Continued.

E_γ (keV)	Nucleus	I_γ (rel. int.)	A_2	A_4
835.2		1.08(11)		
838.5		1.08(11)	0.24(4)	-0.15(8)
843.9		4.61(28)		
846.9		3.31(21)		
883.5		2.61(17)		
902.8	a	20.3(12)		
937.1	^{18}F	6.0(3)		
1014.2		7.8(5)		
1098.9		0.82(13)		

a. Placed in level scheme.

*Multiple peak.

analyzed in the same manner as the singles spectra with SAMPO. The 390 keV gamma ray which depopulates a 5.2 msec isomer was used for normalization between angles, since it would be isotropic. The peak areas were then fit to the usual angular distribution function (Equation 16) in this case:

$$I = I_o [1 + A_2 P_2(\cos\theta) + A_4 P_4(\cos\theta)]. \qquad (45)$$

The coefficients A_2 and A_4 were obtained and used to indicate the multipolarity of the transition and to some extent the dipole-quadrupole mixing ratios. Due to inherent inaccuracies and error in multiplet peak areas, accurate A_2 and A_4 coefficients were not obtainable in many cases. Angular distributions from lines depopulating isomers as short lived as 25 nsec were isotropic. The hexagonal crystal structure of Hf causes rapid dealignment and isotropy (Section 3-1). Useful angular distribution data concerning the multipolarity of lines deexciting isomers was lacking therefore, and for the most part the data served to confirm the dipole and stretched quadrupole nature of transitions in the rotational bands.

7.3. Gamma-ray Lifetimes

Gamma-ray lifetimes were obtained by performing timing experiments in which the detection of the gamma-ray is timed against the arrival of the beam pulse. Two parameter data were required (energy, time) as with the g-factor data, Section 3.3.2. This time the time spectrum was gated into 10 bands and the respective energy spectra accumulated.

The first timing experiment was done with the beam sweeper removing six out of seven beam pulses resulting in 338 nsec between bursts. The time bands were set giving 30.7 nsec between each collected energy spectrum. The spectra were analyzed with SAMPO, sorted and least squares fitted with a program called FITBAND [FITB]. The results are given in Table 7-2 for some delayed lines found.

A series of long-lived lines is present, the half-lifes of which are beyond the range of this experiment. These form a rotational band as confirmed by coincidence data. Apparently a long-lived isomer feeds into this band. In order to determine the half-life a slow beam pulsing experiment was done. In this experiment a high voltage square wave is applied to the deflector plates allowing one to obtain macroscopic beam pulses with minimum width of 40 μsec and beam off time of 50 μsec. Using a 20 μsec TAC range and 1.28 μsec between time

Table 7-2. Delayed γ's in ^{180}W.

Energy	$t_{1/2}$	Comments
103*	19.2 ns + 5.2 msec[a]	$8^- + 5^{(-)}$
108	13 ns	unknown
125	8.6(6) ns	15^+
158	20.3(6) ns	16^+
178	26(5) ns	$5^{(-)}$
196*	150 ns + 2.3 μsec[a]	^{19}F, 14^-
219	2.05(20) μsec	
222*	2.3 μsec[a] + 5 min[a]	14^-, ^{179}W $\frac{1}{2}^-$
224	24(7) ns	$5^{(-)}$
234	5.3 msec	8^-
238	26(8) ns	unplaced high spin line
241	2.7(4) μsec	14^-
263	2.26(7) μsec	14^-
284	2.82(9) μsec	14^-
306	2.09(22) μsec	14^-
332	23(7) nsec	$5^{(-)}$
351	5.3 msec	8^-
365	18.3(4) μsec	^{181}W $\frac{5}{2}^-$
390	5.3 msec	8^-
416	2.25(6) μsec	14^-
450	5.3 msec	8^-
455	20 ns[a]	
461	2.17(6) μsec	14^-
505	2.3 μsec[a]	14^-
528	2.13(1) μsec	14^-
548	2.38(8) μsec	14^-
591	2.25(5) μsec	14^-

*Multiple peaks.

a. Evident but not measured in this work. The 5.2(2) msec

Table 7-2. Continued.

value is from [Bu66] for the 8^- isomer. The 19.2(3) nsec measurement for the $5^{(-)}$ isomer is from [Ma79].

Summary of Isomer Half Lives Measured

Spin	
8^-	5.2(2)* msec [Bu66]
$5^{(-)}$	24(7) nsec, 19.2(3)* [Ma79]
14^-	2.3(2) μsec
15^+	8.6 (6) ns
16^+	20.3(6) ns

*Taken from stated reference, others from this work.

bands a half life of 2.3(2) sec was found for the isomer. Figure 7-2 shows the decay of these lines. The high energy tailing is a result of excessive count rates. The counting rate was kept at around 15 kHz assuming most of the rate was in the prompt part of the spectrum, but pileup still resulted in the delayed spectra causing the skewed peaks.

It became evident that there were short lifetime isomers in the 20 nsec region from the first timing experiment. To more accurately determine these lifetimes another experiment was done, this time using a low energy photon spectrometer (LEPS) for better low energy resolution (0.774 keV FWHM at 122 keV ^{57}Co). One of five beam sweeping was used, giving 8 nsec per time band. The results showed a delayed 125 keV and 158 keV line which were suspected of feeding the 14^- isomer as deduced from delayed coincidence data. The results are included in Table 7-2.

7.4. Delayed Coincidence Experiment

Due to the intensity of the 2.3 μsec delayed lines it was expected that they made up a rotational band built on the known $K^\pi = 8^-$ 5.2 msec $t_{1/2}$ isomer [Bu66]. To place this 2.3 μsec isomer and find higher lying states feeding it a delayed coincidence experiment was planned in which both γ-γ and γ-beam timing information were recorded along with the detector-energies E_1 and E_2.

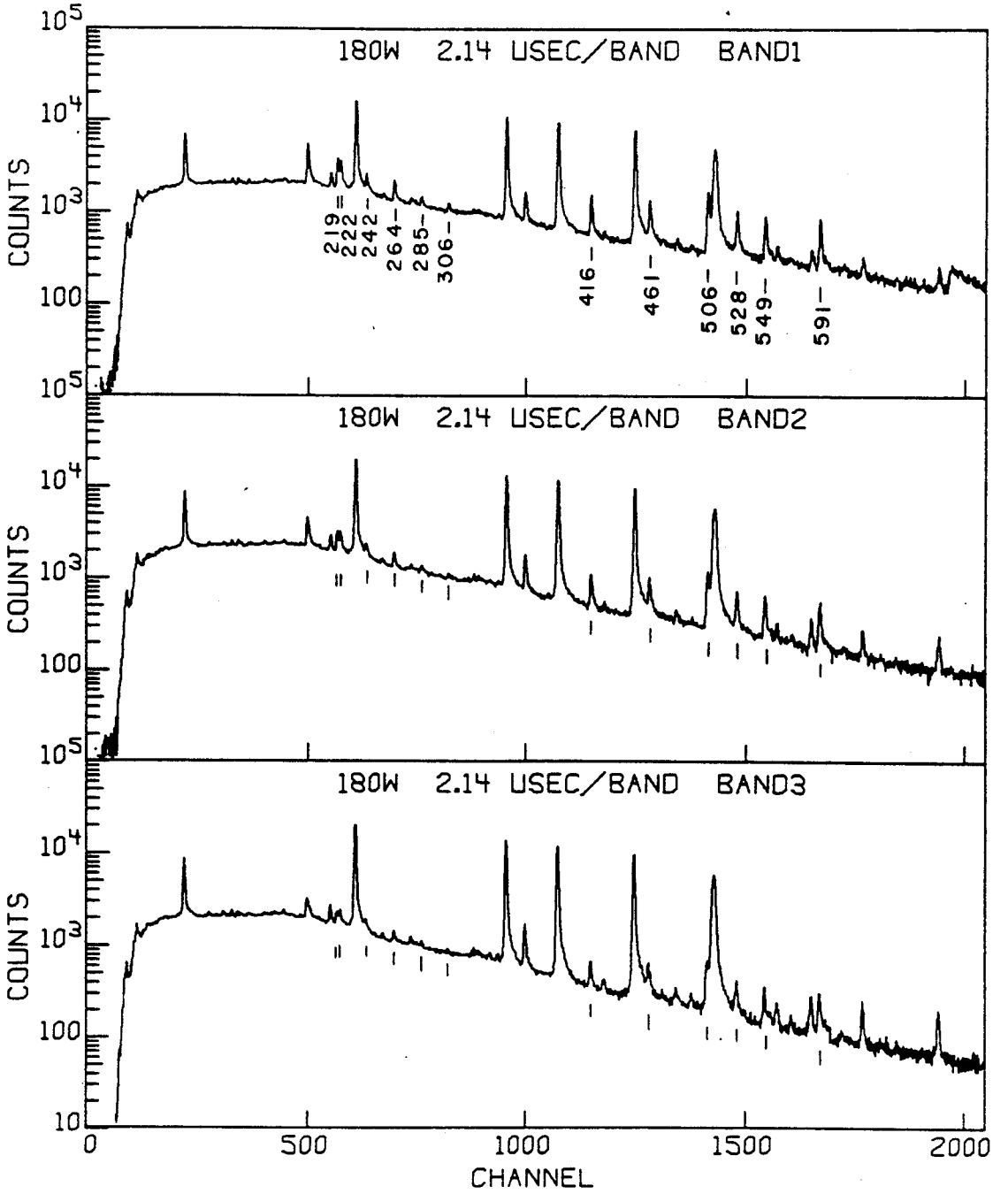

Figure 7-2. Delayed spectra showing the decay of the 2.3 usec isomer.

The beam was swept at 1 out of 11 leaving 536 nsec between beam bursts. The 4-parameter data was recorded event by event on tape to be sorted later as desired. Two 10% efficient Ge(Li) detectors were used resolution 2.1 to 2.2 keV FWHM at 1332 keV. 10 tapes of data were collected at approximately 3 million events per tape.

Coincidence data were sorted using the program KKRECOVERY [KKRE] which allows up to 120 2048 channel spectra to be generated from corresponding gates in about 30 minutes of Xerox Σ7 computer time per tape.

Clean background-free coincidence data on the delayed lines were obtained from setting a delayed gate on the γ- beam TAC showing clearly the $K^{\pi} = 8^{-}$ band. A delayed gate on the γ-γ TAC yielded information on levels feeding isomers including confirmation of the $K^{\pi} = 8^{-}$ band placement. These data provided the bulk of information from which the level scheme was deduced. The level scheme is shown in Figure 7-3.

7.5. Prompt Coincidence

In looking at the high spin states the intensity of the lines was very weak. Various tricks were used to attempt to improve the statistics such as gating on both detectors, shifting the spectra by computer to match gains, and adding the resultant spectra. The delayed coincidence data were limiting since the duty cycle of the beam was reduced

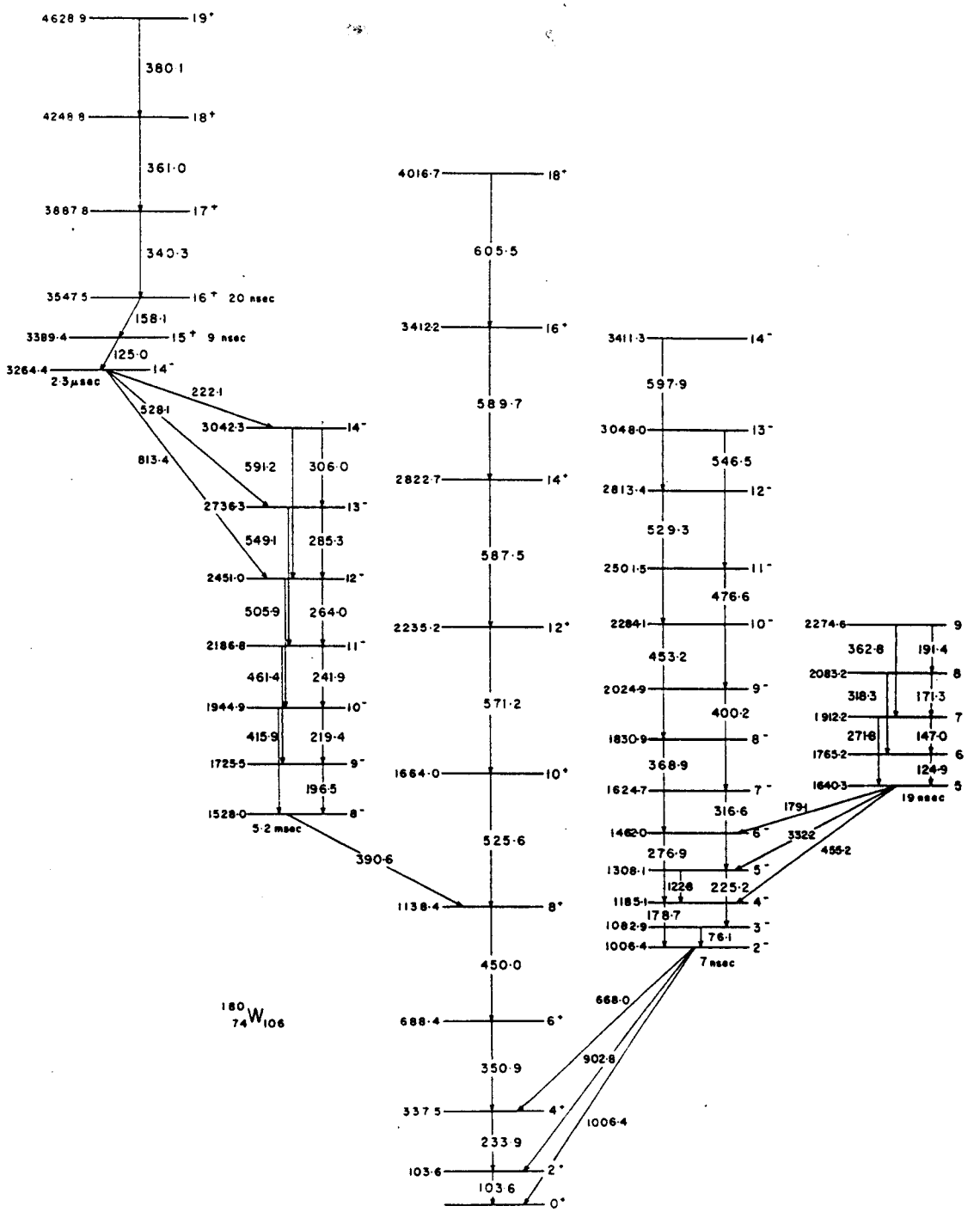

Figure 7-3. Level scheme for ^{180}W.

11 to 1, resulting in fewer prompt coincidence events per unit time than could be obtained with a non-swept beam. To clarify the complicated high spin states feeding the $K^{\pi} = 14^{-}$ isomer a prompt coincidence experiment would be of value. Delayed gates on the γ-γ TAC would provide the necessary delayed-coincidence data to resolve the placement of the nanosecond isomers above the $K^{\pi} = 14^{-}$. For these reasons a prompt coincidence experiment was done. The beam energy used was 49.4 MeV compared to 47.0 MeV used previously. More (α,5n) product (^{179}W) was produced with the higher energy beam but the higher energy also favored the population of the high-spin states which were the subject of investigation. The Appendix shows some gates that were useful in determining the level scheme.

VIII. ^{180}W EXPERIMENTAL RESULTS

8.1. The Ground Band and Backbending

The ground band has been determined to spin 18 as shown in the level scheme, Figure 7-3. In a pure rotational band there is a constant difference between successive transition energies. This is certainly not the case with this band. In order to show rotational band deviation more clearly it is customary to plot $\frac{2\mathcal{J}}{\hbar^2}$ = where $\mathcal{J}$ is the moment of inertia vs. $(\hbar\omega)^2 = (\Delta E/2)^2$ where ω is the rotational frequency. Figure 7-4 shows such a plot for ^{180}W. For a rigid rotor one would obtain a horizontal line. A vibrator would give a vertical line. The variable moment of inertia model (VMI) which predicts a smooth increase in the moment of inertia with increasing rotational frequency would give a straight line with a positive slope intermediate between the rotor and vibrator models. ^{180}W shows a sharp upbend around spin 14 (Figure 8-1). Certain rare-earth nuclei such as ^{162}Er exhibit an even more pronounced backbending of this curve from which the term "backbending" arises.

Backbending is thought to be caused by a rotation-alignment effect where a pair of high-j, usually $i_{13/2}$ neutrons, unpair and align themselves with the spin of

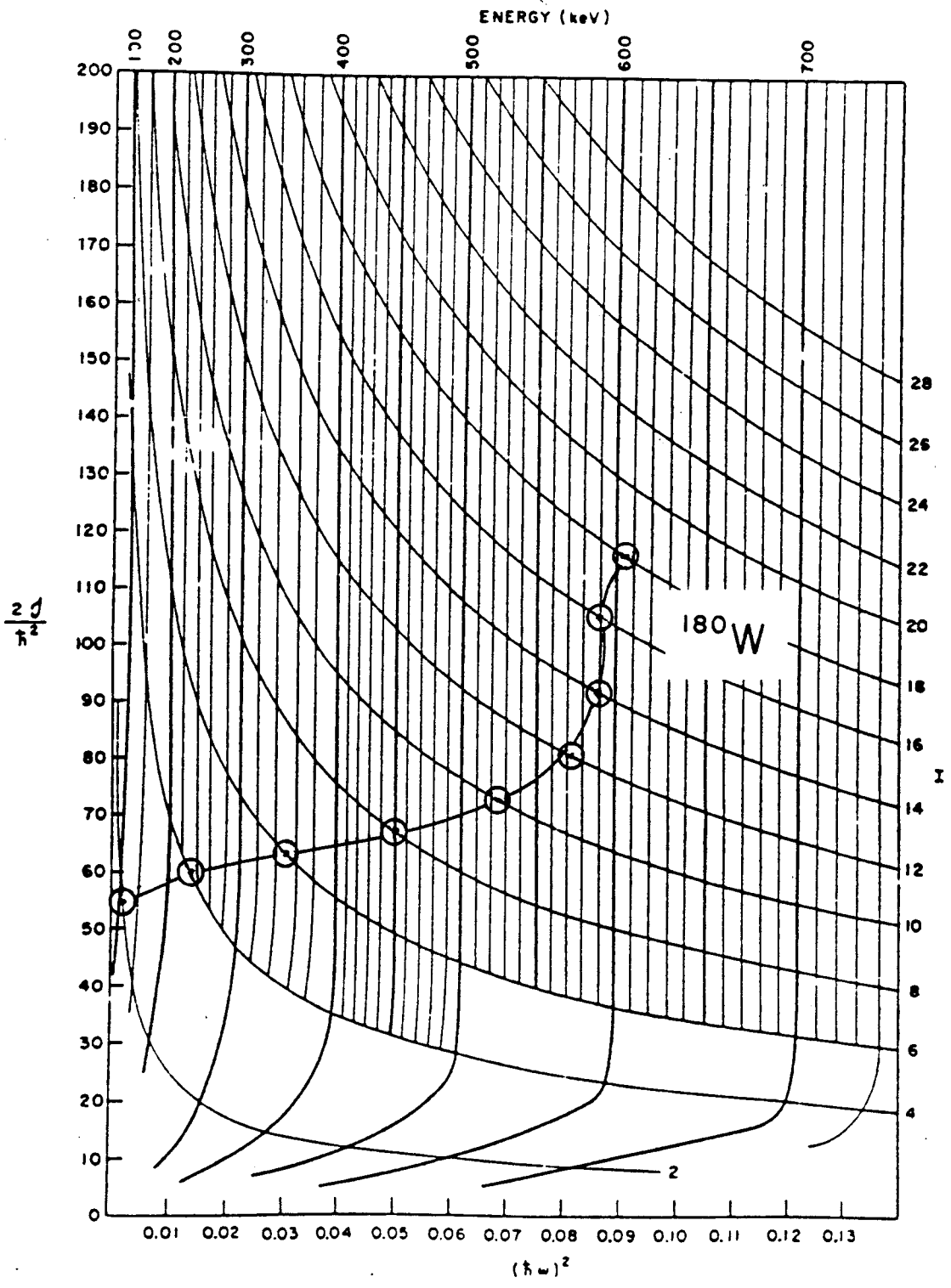

Figure 8-1. Backbending plot for ^{180}W.

the rotating core due to the Coriolis force [St72]. This causes an effective increase in the moment of inertia responsible for the observed curve. In a less simple but related model proposed many years before the actual discovery of backbending it was explained as a breakdown of the superfluidity (paired spins) of the nucleus [Mo60].

Some calculations have been done in the ^{180}W region by Bernthal et al. that describe the backbending behavior quite well [Be74], [Be76]. A comparison is made between the amount of decoupling observed in $i_{13/2}$ bands in corresponding odd-A nuclei and the degree of backbending observed in the even-A nuclei. The amount of decoupling is calculated by obtaining wavefunctions for the $i_{13/2}$ bands from a fit to observed energy levels and calculating the expectation value of the rotational angular momentum $\langle R^2 \rangle$. The values for $\langle R^2 \rangle$ are compared to the minimum value possible for $\vec{R}$, $\vec{R}_{dec} = \vec{I}-\vec{j}$ (See Figure 6-1). The difference $[\langle R^2 \rangle = \langle R^2_{dec} \rangle]$ tends to be zero for highly decoupled (particle angular momentum aligned with the core angular momentum) bands and approaches zero with increasing spin of the nucleus. The amount of decoupling in the odd-A nucleus predicts quite well (with the exception of ^{170}Yb) the amount of backbending observed in the corresponding even (A+1) nucleus.

8.2. The K = 2^- Band

The 2^- level of the octupole band has been seen in the study of the radioactive decay of ^{180}Re [Ho67], [Go67]. The 3^- level is also seen, but the placement of these levels was wrong until clarified by conversion electron data [Ha68] from the decay. The 3^- level is strongly populated in the (d,d') reaction [Gu71]. The decay of the ^{180}Re ground state $\{\pi\frac{5}{2}^+[402\uparrow] \times \nu\frac{7}{2}^-[514\downarrow]\}_{1^-}$ to the 2^- level is an unhindered allowed beta transition consistent with the observed log ft value suggesting a single particle transition of $\nu\frac{7}{2}^-[514\downarrow] \rightarrow \pi\frac{9}{2}^-[514\uparrow]$ and a configuration of $\{\pi\frac{9}{2}^-[514\uparrow] \otimes \pi\frac{5}{2}^+[402\uparrow]\}_{2^-}$ for the 2^- level [Ho67]. This decay occurs with a 7.4(4) ns $t_{1/2}$ [Go67].

The $K^\pi = 2^-$ band has been determined to spin 14^- in this work and has subsequently been seen to spin 11^- in the (p,2n) reaction [Ma79]. The 902 keV gate, Figure 8-2, and gates on transitions within the band confirm its existence quite conclusively. Only the E2 transition connecting the odd spin members to the odd, and even to the even are seen clearly. The odd-even M1/E2 transitions are very weak; only the 122.8 keV $5^- \rightarrow 4^-$ transition can be seen clearly. A good angular distribution for one of these transitions may indicate the proton-neutron character of the band as in Section 8.3. The 122.8 keV coincidence gate shows some unexplained lines suggesting it may be a doublet but the majority of the intensity is from the

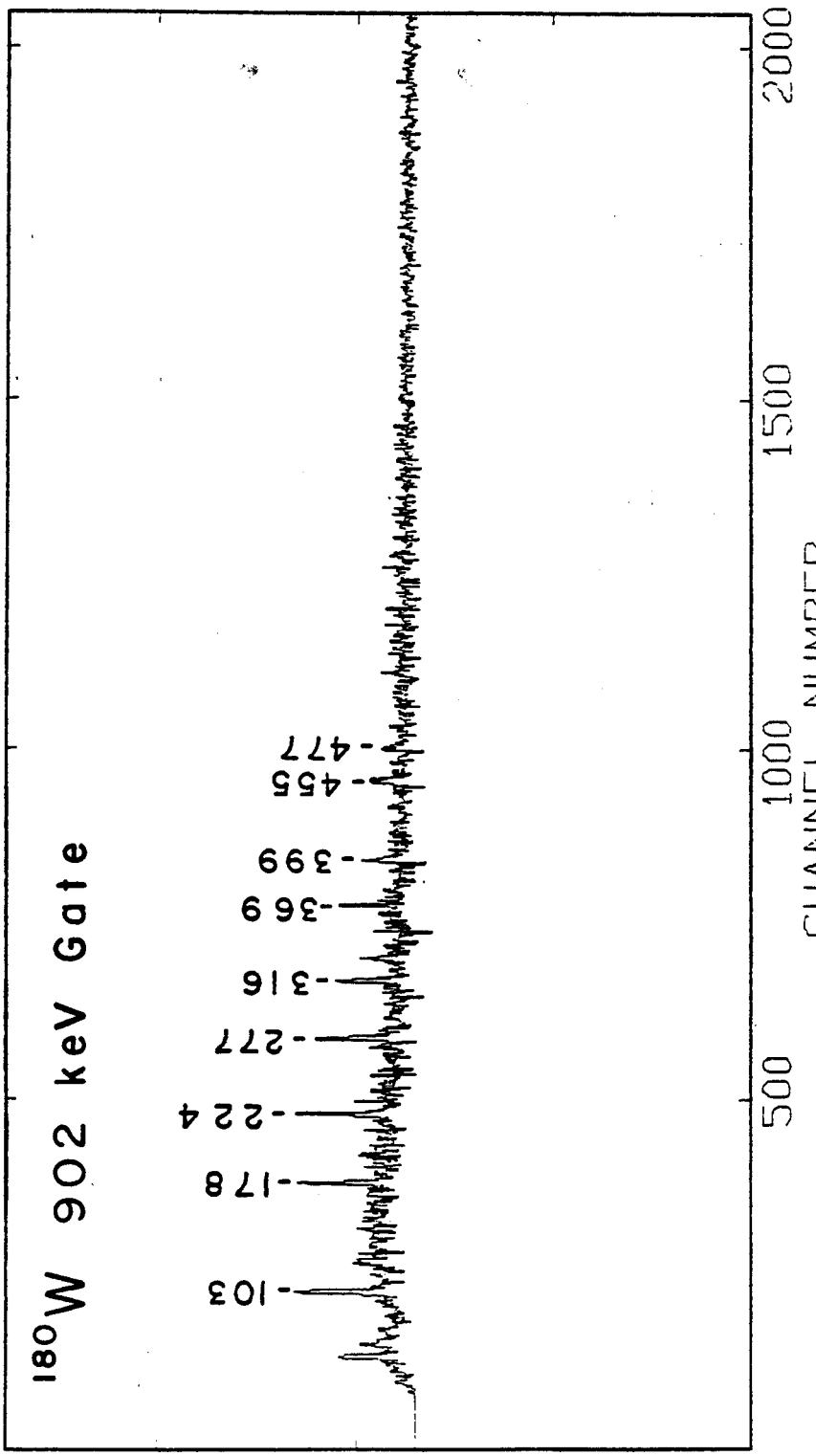

Figure 8-2. The 902 keV coincidence gate.

$5^- \rightarrow 4^-$ transition. The angular distribution for this peak is shown in Figure 8-3 gives $A_2 = 0.24(6)$ and $A_4 = 0.17(9)$. Assuming an $\alpha_2 \simeq .6$, $\delta = 0.37$ or 4.89 requiring an A_4 of 0.05 or 1.6. The first value of $\delta = 0.37$ is more compatible with the observed A_4. The positive sign obtained for the δ suggests a proton configuration in keeping with the previous assignments. The g-factor by branching ratio method was not attempted due to the questionable value of such a result obtained from such a highly perturbed structure.

The "perturbed" nature of the band is indicated by the non-rotational energy level spacing of the band. The odd and even spin members act almost as separate bands in that they each have different moments of inertia when plotted on a $\Delta E/2I$ vs $2I^2$ plot (Figure 8-4). A $K \neq \frac{1}{2}$ rotational band obeys the following formula:

$$E = AI(I+1) + BI^2(I^2+1). \qquad (46)$$

The A term is $A = \frac{\hbar^2}{2\mathcal{I}}$ and the B term is a higher order correction that accounts for the stretching of the nucleus as a function of rotational frequency and subsequent increase in moment of inertia. On the above type of plot A is the intercept and B is the slope. A good rotational

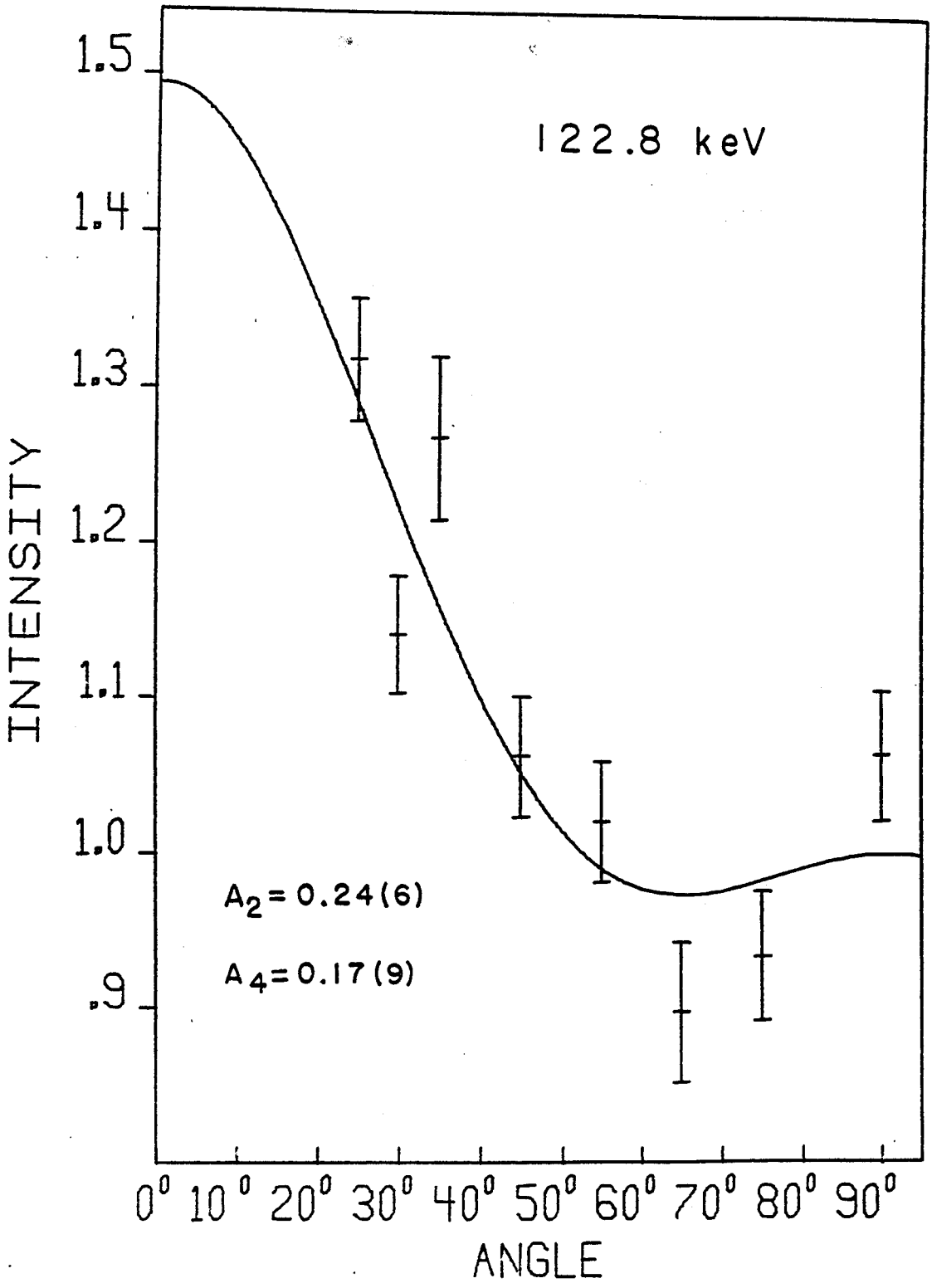

Figure 8-3. Angular distribution of the 122.8 keV $5^- \rightarrow 4^-$ transition.

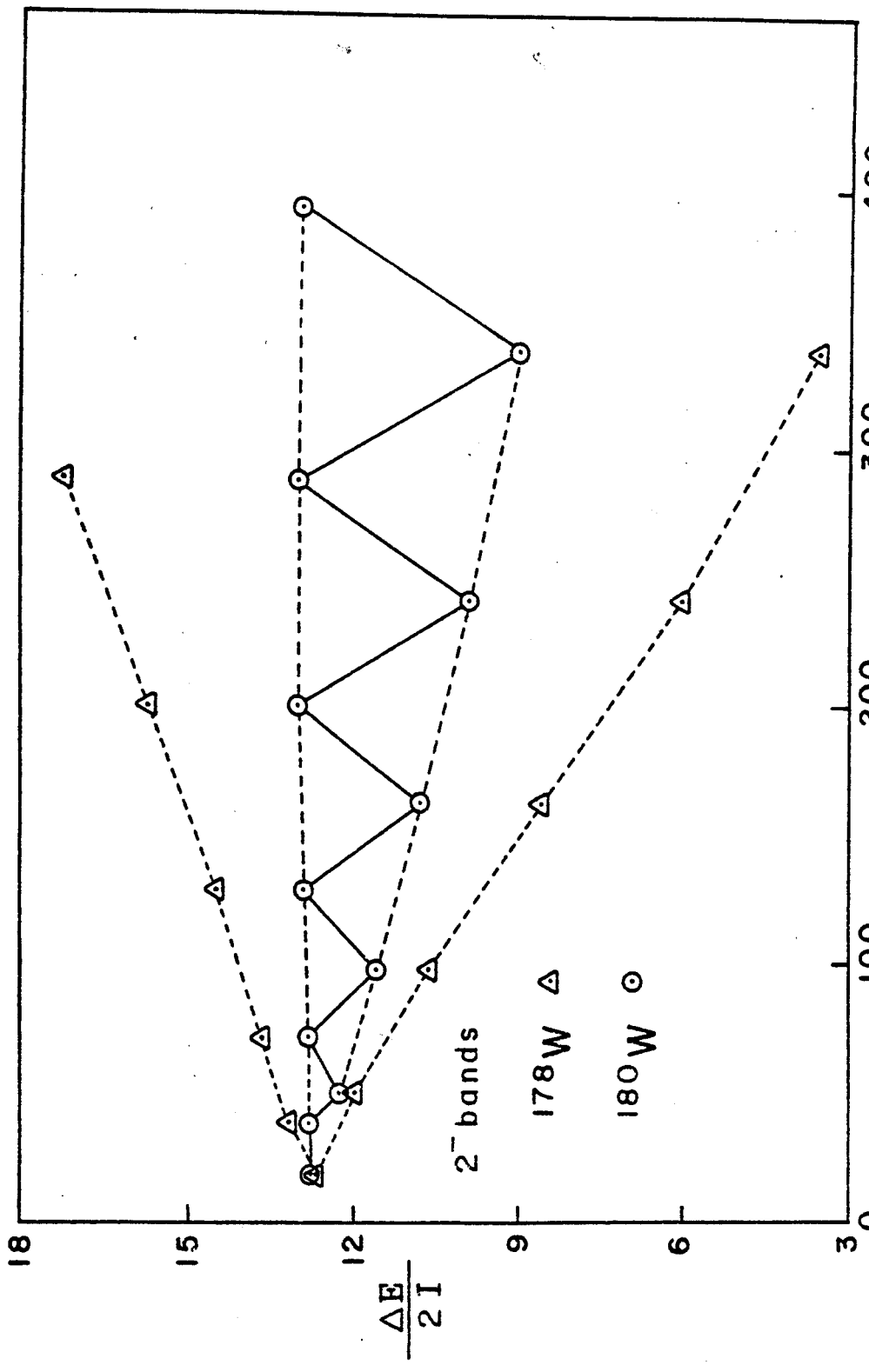

Figure 8-4. $\Delta E/2I$ vs $2I^2$ plot of the $K^{\pi} = 2^-$ bands of $^{178,180}W$.

band would be a level line with some intercept A and small slope B. The $K^{\pi} = 2^{-}$ bands in the light W and Yb nuclei exhibit this odd-even splitting behavor. This has been attributed to the effect of mixing of the odd spin members with an unseen $K^{\pi} = 0^{-}$ band (which contains only odd spin members for symmetry reasons). The energies of these odd spin levels are then depressed compared to the evens giving rise to the apparent higher moment of inertia. This mixing is greater when the state has some $i_{13/2}$ 2-quasi-particle component since the Coriolis mixing is greater for high j orbitals. There is indirect evidence for $i_{13/2}$ neutron components in the systematics of $^{174,176,178,180}W$ negative parity yrast bands [WALK]. If the $i_{13/2}$ neutron bands of the corresponding odd-mass nuclei are plotted similar to Figure 8-4 the magnitude of the oscillations follows the same trend as the octupole bands in Figure 8-4 [WALK]. The magnitude of the oscillations also increases with decreasing mass. This can be explained in terms of the increasing Coriolis mixing as the Fermi surface descends to lower Ω Nilsson orbitals with decreasing mass. (Lower Ω results in increased Coriolis forces.)

The negative A_2 of the 113.5 keV $4^{-} \rightarrow 3^{-}$ and 133.8 keV $5^{-} \rightarrow 4^{-}$ transitions suggest neutron character for the $K^{\pi} = 2^{-}$ band in ^{182}W [Je77]. The M1/E2 transitions are not seen in ^{178}W, however, so no such argument can be made there [Do79]. Similar arguments have been made for the

negative parity yrast bands in ^{170}Yb however [Wa79].

The 902 keV $2^- \rightarrow 0^+$ transition has been shown to have mixed E1-M2-E3 character from angular correlation studies [Ko71]. The presence of the E3 octupole component suggests a highly collective (octupole vibration) nature. The strong population of the 3^- level in the (d,d') reaction also suggests collectivity [Gu71].

In conclusion it is probably impossible from this evidence to assign a particular particle configuration to this band, as it is probably a mixture of all of these.

8.3. The $K^\pi = 5^{(-)}$ Band

The coincidence data give good evidence of a band feeding into the 4^-, 5^-, and 6^- levels of the $K^\pi = 2^-$ band. It is populated rather weakly but is seen clearly in the ^{181}Ta(p,2n)^{180}W reaction also [Ma79]. From the way it feeds the $K^\pi = 2^-$ band one would expect it to be a $K^\pi = 5^\pm$, $6^\mp$ band. Some possible 2-quasiparticle states include (See Table 6-1) a $\{\frac{7}{2}^-[514\downarrow]_n \otimes \frac{5}{2}^-[512\uparrow]_n\}\ 6^+$ state and a $\{\frac{7}{2}[404\downarrow]_p \otimes \frac{5}{2}[402\uparrow]_p\}6^+$ state. Due to the unexpectedly low energy of the $\frac{1}{2}^-[521\downarrow]$ neutron orbital as seen in ^{179}W a configuration of $\{\frac{9}{2}^+[624\uparrow]_n \otimes \frac{1}{2}^-[521\downarrow]_n\}5^-$ is also possible (See Section 8.6.3). If one plots ΔE vs I for this band it is a straight line through the origin for a K = 5 band (Figure 8-5) with the same slope as the

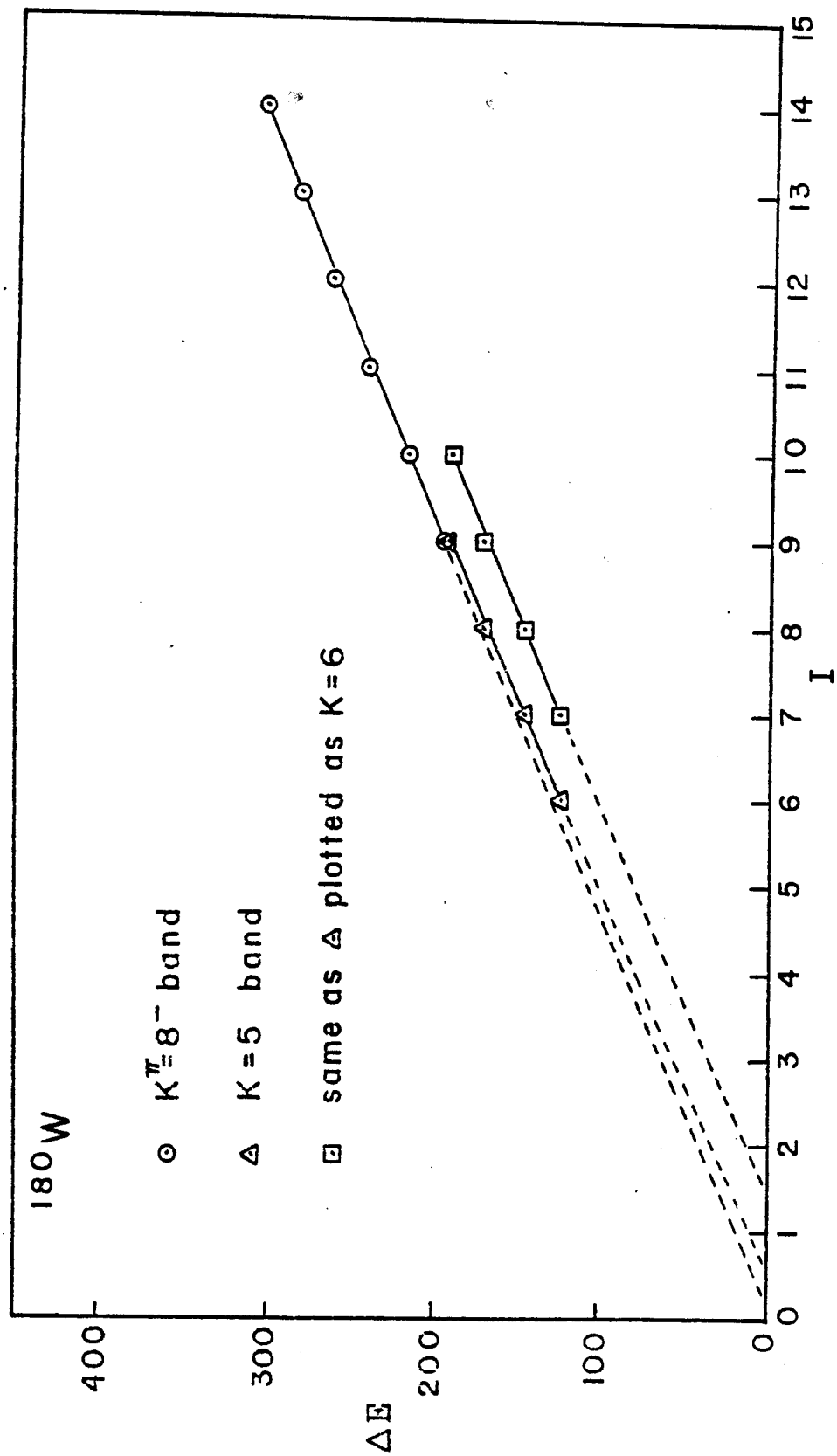

Figure 8-5. ΔE vs I for the $K^{\pi} = 8^{-}$, $5^{(-)}$ bands.

K = 8 band. The E/2I vs $2I^2$ plot (Figure 8-6) is also more consistent with a K = 5 assignment but no direct proof exists since the angular distributions for the inter-band transition are isotropic due to the 20 ns lifetime of the bandhead. Timing measurements show a half life of 26(5) nsec from the 178 keV doublet in the LEPS timing data, and a $t_{1/2}$ - 24(7) nsec for the 224 line. These are close to the $t_{1/2}$ = 19.2(3) nsec measurement from the (p,2n) reaction [Ma79], but the transitions are very weak in this reaction (α,4n) and hence yield inaccurate half life values.

8.4. The $K^{\pi} = 8^-$ Band

As mentioned previously the delayed coincidence experiment provided the proof of the existence of a band built on the 8^- $t_{1/2}$ = 5.2 msec isomer fed by a higher lying isomer. Some out of beam coincidence gates and angular distributions of transitions in the band are given in the Appendix and show conclusively levels up to 14^- in the band. Delayed gates on the ground band and 390 keV transitions show the presence of the band. The intensities are also consistent with the band based on the $K^{\pi} = 8^-$ isomer. A plot of E/2I vs $2I^2$ for the band (Section 8.2) gives a very flat line (Figure 8-6). No backbending or other perturbation is seen. The moment of inertia is consistent

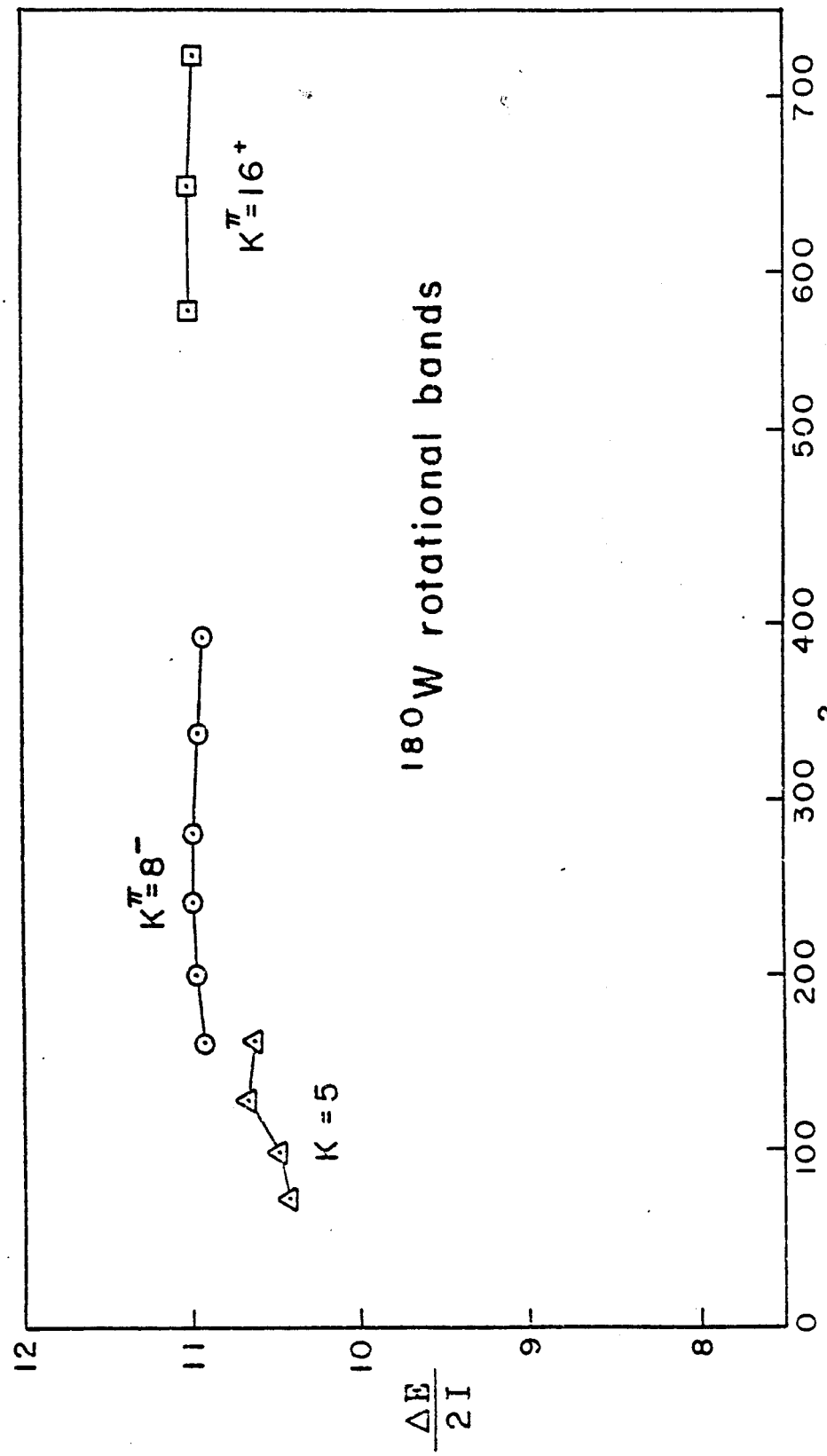

Figure 8-6. $\Delta E/2I$ vs $2I^2$ plot of the $K^{\pi} = 5^{(-)}$, 8^-, and 16^+ rotational bands.

with the bands seen in the isotone ^{178}Hf [Kh77]. The particle configuration of the band is deduced in Section 8.6.2 from the branching ratios. The $t_{1/2}$ of the 8^- isomer has not been measured in this work but is given by Burde et al. as 5.2(2) msec [Bu66].

8.5. High Spin 4-Quasiparticle Isomers

8.5.1. The $K^\pi = 14^-$ Isomer

When it was discovered that the transitions in the $K^\pi = 8^-$ rotational band were delayed (as seen in the 350 ns range timing experiment) the existence of a high lying 4-quasiparticle state was suspected. A 20 μsec range, slow beam pulsing experiment was done (Section 7.3) and the half life of this isomer was found to be $t_{1/2}$ = 2.3(2) μsec (averaged from several transitions).

The spin of the isomer can be guessed at in a manner similar to the K = 5 band assignment, by the way it feeds into the K = 8 band (see level scheme Figure 7-3). Probable spins are $14^\pm$ or $13^\pm$. Multipolarities cannot be obtained from the angular distribution, but conversion coefficients can be obtained from intensity balances in the delayed spectra. On this basis the conversion coefficient for the 222 keV transition can be deduced. The conversion coefficient for the 528 and 813 keV lines are quite small and can't be obtained with much accuracy.

The 222 keV line is a doublet with the $\frac{1}{2}^- \rightarrow \frac{7}{2}^-$ (gnd. state) delayed (5.2 min) transition in ^{179}W, but the percent contribution to the observed line can be calculated from the published relative intensities in ^{179}W [Be75] and the observed relative intensities for the ^{180}W reaction (Table 7-1). Using intensities obtained from the 20 μsec range timing experiment and subtracting an estimated 19% of the 222 keV intensity due to the delayed impurity line from ^{179}W, the conversion coefficient is $\alpha_T \approx 0.55(4)$ (neglecting efficiency calibration errors). The theoretical total conversion coefficients for various multipolarities are:

	α_T
M1	0.54
E1	0.050
M2	2.21
E2	0.22

The data predicts an M1 which means the level would be a spin 13^- or 14^-.

Using a model dependent argument, a look at possible 4-quasiparticle isomers of that energy (Table 6-1) shows a 14^- $\{\nu\frac{9}{2}^+[624\uparrow] \otimes \nu\frac{7}{2}^-[514\downarrow] \otimes \pi\frac{7}{2}^+[404\downarrow] \otimes \pi\frac{5}{2}^+[402\uparrow]\}$ configuration at one of the lowest excitation energies, E = 3.4 MeV in good agreement with the experimental findings E_{isomer} = 3.264 MeV.

From systematics, a look at the isotone ^{178}Hf shows the presence of a similar 14^- isomer feeding a $K^\pi = 8^-$ band [Kh77]. From these arguments, a $K^\pi = 14^-$ is assigned to this isomer.

8.5.2. The $K^\pi = 15^+$ Isomer

Delayed coincidence gates from the 4 parameter experiment were set on transitions in and feeding the $K^\pi = 8^-$ band in order to determine transitions feeding the $K^\pi = 14^-$ isomer.

The resultant sum of these gates is shown in Figure 8-7. One can see clearly 125 and 158 keV lines feeding the isomer Both the 125 and 158 keV transitions are seen to be delayed in the timing experiments with a $t_{1/2}$ of 15 to 20 nsec. Half life curves for these transitions taken from the LEPS timing experiment are shown in Figure 8-8. The experiment was performed with a band set in the prompt part of the TAC spectrum starting at the centroid (t = 0). This enables one to detect the presence of a prompt component of a delayed line. Note that both the 125 and 158 keV transitions show no apparent prompt component, indicating that they directly depopulate an isomer. (See note in Appendix.) In other words there are two higher lying isomers (4-quasiparticle) that lie above the $K^\pi = 14^-$ isomer.

Delayed gates set on the 125 and 158 keV transitions

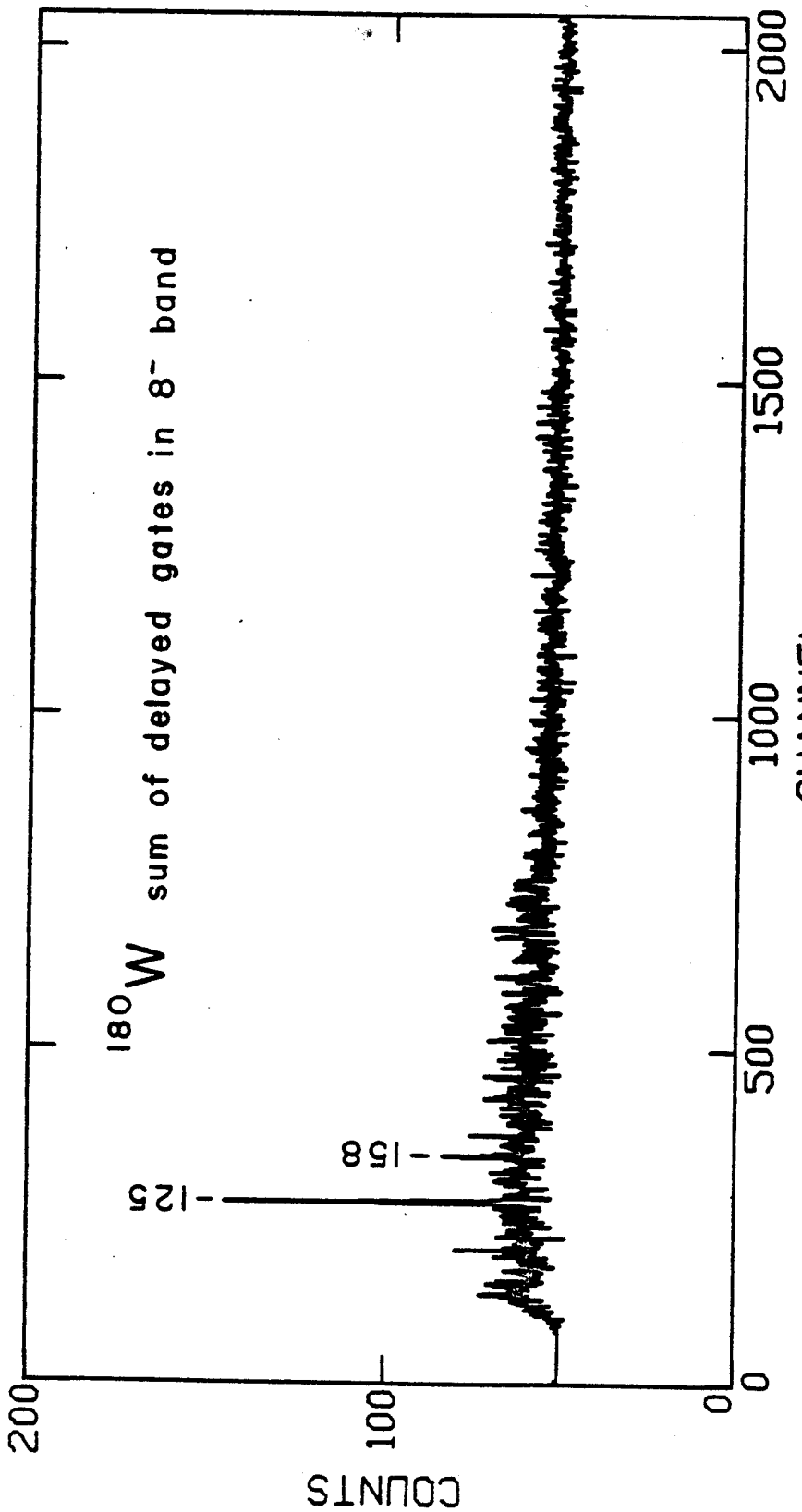

Figure 8-7. Sum of delayed gates set on members of the $K^{\pi} = 8^{-}$ rotational band.

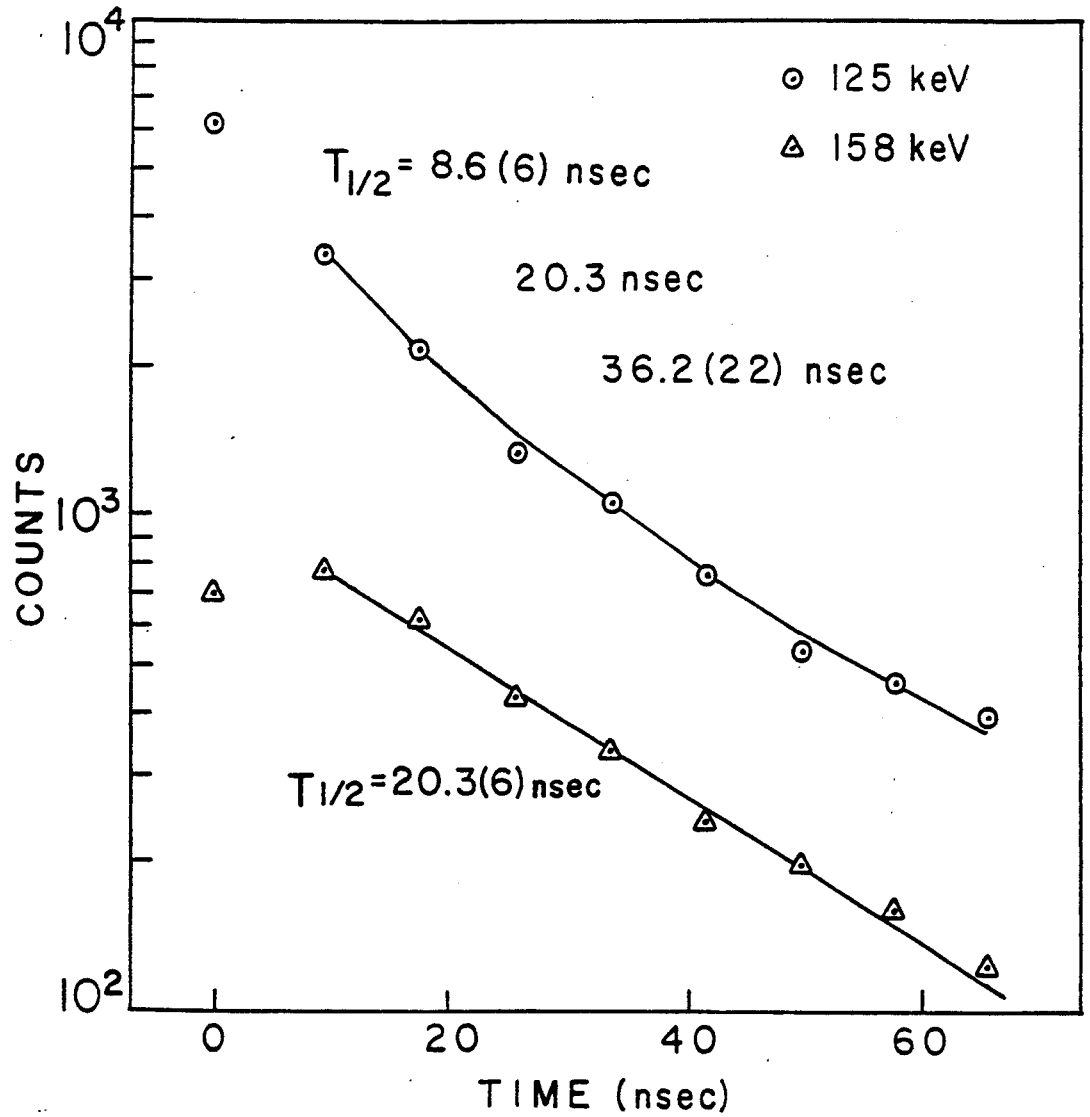

Figure 8-8. Half lives of the 125 and 158 keV transitions.

show a rotational band built on the 158 keV transition. The level scheme then takes the form as in Figure 7-3. Spectroscopically the multipolarities of the 125 and 158 keV transitions can't be absolutely determined, but a coincidence gate on a transition feeding the two isomers should give the relative electron conversion ratio of the two lower transitions. That is, the coincidence gate of the 340 keV transition should show the 125 and 158 keV transitions with equal intensity except for a small correction taking into account the differing half lives. Any intensity difference seen would be due to internal conversion and the efficiency of the detector. The 125 keV transition is seen much more strongly than the 158 keV indicating a higher conversion coefficient for the later.

From the list of possible quasiparticle isomers predicted (Table 601), a 16^+ $\{\nu\frac{9}{2}[624\uparrow] \otimes \nu\frac{7}{2}^-[514\downarrow] \otimes \pi\frac{7}{2}[404\downarrow] \otimes \pi\frac{9}{2}^-[514\uparrow]\}$ or a 15^+ $\{\nu\frac{9}{2}[624\uparrow] \otimes \nu\frac{7}{2}^-[514\downarrow] \otimes \pi\frac{5}{2}[402\uparrow] \otimes \pi\frac{9}{2}^-[514\downarrow]\}$ are probable. Assuming these are the isomers, an ordering of 15^+ above the 16^+ would give multipolarities of M1 and M2 for the 158 and 125 keV transitions respectively. The M2 would be highly converted and the γ-intensity would be low. The data supports the opposite ordering consistent with a low conversion for the 125 keV E1 and a moderate conversion for the 158 keV M1.

8.5.3. The $K^{\pi} = 16^{+}$ Band

The rotational band built on the 16^{+} isomer is plotted in Figure 8-6 and is consistent with the moments of inertia seen for the other bands, giving additional evidence in favor of the adopted scheme.

The transitions within the band are seen to have highly anisotropic angular distributions with large positive A_2 values (Table 7-1). The mixing ratio calculated from the A_2 is large suggesting a high g-factor (proton configuration) for the band. Indeed, the g_K calculated (in Section 8.6.4) accurately corresponds to the theoretical g-factor for the proposed 2 proton-2 neutron configuration. The large mixing ratio may also explain the unseen E2 crossover transitions.

This isomer is also seen in the isotone ^{178}Hf where it lies at a lower energy than the $K^{\pi} = 14^{-}$ isomer [Kh77]. The $K^{\pi} = 14^{-}$, and 16^{+} isomers in ^{178}Hf are yrast traps; that is they lie lower in energy than corresponding spin members of the other bands. This may result in a long lifetime for the isomer if they can decay only by high multipolarity K forbidden transitions. The $K^{\pi} = 16^{+}$ example in ^{178}Hf is particularly striking in that it has a half life of 31 years [He68]. In ^{180}W, however, the Fermi surface has risen above the two proton orbitals involved ($\frac{9}{2}^{-}[514\uparrow]$ and $\frac{7}{2}^{+}[404\downarrow]$) (See Figure 6-2), causing the energy of the 16^{+} isomer to be higher in this nucleus than in ^{178}Hf.

8.6. g-Factors From Branching Ratios

8.6.1. Method

G-factors for the bandheads of rotational bands can be deduced from branching ratios within the band in the framework of the Nilsson model. The branching ratios here are the ratio of intensity of the E2 crossover to the M1+E2 cascade transition leaving the same level within the band. Values of the mixing ratio-squared δ^2 and $|g_K-g_R|$ can be obtained if Q_o, the quadrupole moment of the nucleus, is known. These quantities are computed from the following formulas [A164]:

$$1 + \frac{1}{\delta^2} = \frac{(I+1)(I-1+K)(I-1-K)}{2\lambda K^2(2I-1)} \left[\frac{E(I\ I-2)}{E(I\ I-1)}\right]^5$$

$$\lambda = \frac{I_\gamma(I\rightarrow I-2)}{I_\gamma(I\rightarrow I-1)}$$

$$(g_K-g_R) = \frac{0.933\ Q_o\{E(I\rightarrow I-1)(MeV)\}}{\sqrt{(I^2-1)}\ \delta} \qquad (47)$$

Sometimes δ can be deduced from conversion electron or angular distribution data. The quadrupole moment Q_o

is taken to be that of the ground state of the nucleus and can be determined from rotational band theory from the B(E2) of the $2^+ \rightarrow 0^+$ transition [St65] where

$$B(E2) = 4.08 \times 10^{-61}[E_\gamma(\text{MeV})]^{-5}[\tau_{(\text{sec})}]^{-1}[1+\alpha]^{-1} \quad (48)$$

and τ is the mean life of the 2^+ and α the total conversion coefficient. (One must be careful which definition of B(E2) one uses because they differ from source to source.) Q_o is then

$$Q_o = [16\pi B(E2)/5]^{1/2} \quad (49)$$

Using τ = 1.76(4) ns [Zi73] and the energy 103.6 from this work, and α from [St65], the value Q_o = 6.48(24) was obtained.

The value of g_R of the ground band was determined from the measurement of the g-factor of the 2^+ state using Mossbauer [Zi73] $g(2^+)$ = .258(17) = g_R. The ground band value for g_R was taken to be approximately the same for the other bands when determining g_K for these bands.

Angular distributions can also be used to obtain the

mixing ratio δ. They are not usually accurate enough to yield a good value however. One must have alignment parameters (α_2) which represent the fraction of total maximum theoretical alignment lost. These can be obtained from known unmixed transitions (E2 for example) of similar spin. The corrected A_2 coefficient is entered in a quadratic equation which is solved for δ (see [Mo76] p.55). The appropriate one of the two δ values obtained can sometimes be chosen by comparison with the observed A_4 values.

8.6.2. $K^\pi = 8^-$ Band

The $K^\pi = 8^-$ band is thought to be a two neutron state on the basis of systematics observed through the N = 106 nuclei [Bu66]. The lower mass isotone ^{178}Hf has two $K^\pi = 8^-$ bands, however, a corresponding two neutron $K^\pi = 8^-$ and a two proton $K^\pi = 8^-$ at a lower energy [Kh77]. These two bands are mixed about 64%-36% [He68], [Bo76], as determined by g_K values from branching ratios. In ^{180}W the two proton $K^\pi = 8^-$ is not seen. It would lie at a higher energy in ^{180}W since the Fermi surface for the protons would be farther away from the $\frac{9}{2}[514\uparrow]$ and $\frac{7}{2}[404\downarrow]$ proton orbitals (Section 6.3). The two neutron singlet state $\{\frac{9}{2}[624\uparrow] \otimes \frac{7}{2}^-[514\downarrow]\}_{8^-}$ would be expected to have $g_K = 0$ (Section 2.5), but the g_K values obtained from the data are $g_K = 0.400(12)$ or $0.120(12)$ depending on the sign of δ, (Table 8-1). The angular distributions of the M1/E2

Table 8-1. $K^{\pi} = 8^{-}$ Band

I of Level	$\frac{1}{\delta^2}$	g_K for $+\delta$	g_K for $-\delta$
10	0.67(20)	0.367(24)	0.149(24)
11	1.45(27)	0.419(23)	0.097(23)
12[a]	1.03(24)	0.394(24)	0.122(24)
13	1.03(24)	0.393(23)	0.123(24)
14	1.45(25)	0.418(23)	0.098(23)
average[b]		0.400(12)	0.120(12)
final g_K			0.120(12)
$K^{\pi} = 5^{(-)}$ Band			
8[c]	9.3(10)	0.376(27)	-0.12(3)
9	11.0(18)	0.69(4)	-0.17(4)
average		0.530(24)	-0.150(25)
Final g_K			-0.150(25)

[a]The 264 keV transition from the $I=12^{-}$ level in a doublet and may be unreliable.

[b]Computed omitting the 12^{-} level data.

[c]The 124.9 keV and 271.8 keV lines from the I=6 and 7 levels are doublets and hence omitted.

$g_R = 0.258(17)$ $Q_o = 6.48(24)$

transition in the $K^\pi = 8^-$ band have highly negative A_2 values implying a negative δ, so $g_K = 0.120(12)$. This is slightly greater than the expected $g_K = 0$ indicating a possible small proton admixture similar to the ^{178}Hf case but less, around 12%, assuming $g_K = 1$ for the two proton band.

8.3.3. $K^\pi = 5^{(-)}$ Band

The highly negative A_2 coefficients of the M1/E2 transitions in the K = 5 band suggest a negative also. The branching ratio method yields $g_K = -0.150(25)$ (See Table 8-1) consistent with a two neutron band. From the Nilsson orbitals calculated (Figure 6-2, Table 6-1) one wouldn't have expected any low lying K = 5 isomer since the $\frac{1}{2}^-[521\uparrow]$ orbital is 1 MeV from the Fermi surface. Looking at the neighboring nucleus ^{179}W, however, the $\frac{1}{2}^-[521\downarrow]$ band is seen at an excitation energy of only 222 keV. The actual energy of this orbital must be much closer to the Fermi surface than calculated. On this basis the existence of a K = 5 isomer is not surprising and one would expect it to be $\{\nu\frac{9}{2}^+[624\uparrow] \otimes \nu\frac{1}{2}^-[521\downarrow]\}_{5^-}$. This is a singlet neutron state and would be expected to have $g_K = 0$. A value of $g_K = -0.150(25)$ would be more representative of a triplet neutron configuration such as $\{\frac{1}{2}^-[510\uparrow] \otimes \frac{9}{2}[624\uparrow]\}_{5^-}$. From formula 15 $g_K = -0.46$ for this configuration if the empirical "quenched" value for g_S is used where $g_S = 0.6\ g_{free}$.

The experimental value is closer to $g_K = 0$ suggesting the singlet configuration, but there may be some admixture with this higher energy triplet configuration.

The errors quoted on the g_K values do not reflect possible model dependent errors in determining the δ's. That is the δ value extracted assumes pure rotational band theory is correct with good K quantum number. From the observed energy level spacing and $E/2I$ *vs* $2I^2$ plots (Figure 8-6) the assumptions made are probably quite good.

The δ values calculated from the angular distributions are not model dependent but harder to obtain to a known accuracy. Values obtained for the $K^\pi = 8^-$ band are typically $\delta = -0.6$ or -1.4 by solving the quadratic equation for δ. (Alignment parameters α_2 were obtained from the E2 transitions.) The inaccurate A_4 values observed are not sufficient to choose which δ is appropriate, but each is close to the value $\delta \approx -1$ obtained from the branching ratio data.

The same methods applied to the K = 5 band gives $\delta = -0.27$ or -2.5 for the $I = 8 \rightarrow 7$ transition corresponding to an $A_4 = 0.023$ or 0.30. The $\delta = -0.27$ value is consistent with the observed A_4's and the value $\delta \approx -0.3$ from branching ratios.

8.6.4. The $K^{\pi} = 16^{+}$ Band

No E2 crossovers were observed for this band so a branching ratio calculation could not be done. The angular distribution of the M1+E2 transitions, however, are highly anisotropic allowing a δ value to be extracted which could be used to obtain a g_K value for this isomer. The calculation gives (estimating $\alpha_2 \approx 0.9$) an unambiguous:

$$\delta = 0.48 \text{ for spin 17 yielding } g_K = 0.51$$

and

$$\delta = 0.39 \text{ for spin 18 yielding } g_K = 0.57$$

These g_K values are close to the theoretical $g_K = 0.50$ for the proposed configuration $\{\nu\frac{9}{2}^{+}[624\uparrow] \otimes \frac{7}{2}^{-}[514\downarrow] \otimes \pi\frac{7}{2}^{+}[404\downarrow] \otimes \pi\frac{9}{2}^{-}[514\uparrow]\}16^{+}$ (Table 6-1).

8.7 Summary and Conclusions

In summary three 4-quasiparticle isomers have been discovered in ^{180}W with a rotational band seen on one of them (16^{+}) The rotational band built on the known $K^{\pi} = 8^{-}$ isomer has been discovered and characterized along with the $K^{\pi} = 2^{-}$ octupole band, both to spin 14^{-}. Knowledge of the ground band has been extended to spin 18^{+}. A K = 5, 2-quasiparticle side band has been identified which feeds the $K^{\pi} = 2^{-}$ band. The configurations proposed for the intrinsic

states are summarized in Table 8-2.

^{180}W has proven to be a fruitful nucleus for the study of low lying multi-quasiparticle states. The presence of the Fermi surface in an island of closely spaced high spin Nilsson orbitals accounts for this. More information may be obtained from further study of this nucleus. The present data shows as yet unplaced transitions feeding the 15^+ isomer and 16^+ isomer in the prompt and delayed gates on the 125 and 158 keV transitions. More work might resolve the problem further.

Table 8-2. Summary of Isomers Discovered and Proposed Configurations.

K^{π}	Energy	$t_{1/2}$	Configuration
4-g.p.			
14^-	3264 keV	2.3(2) μsec	$\frac{9}{2}^+[624\uparrow]_n$ $\frac{7}{2}^-[514\downarrow]_n$ $\frac{7}{2}^+[404\downarrow]_p$ $\frac{5}{2}^+[402\uparrow]_p$
15^+	3389	8.6(6) ns	$\frac{9}{2}^+[624\uparrow]_n$ $\frac{7}{2}^-[514\downarrow]_n$ $\frac{5}{2}^-[512\uparrow]_n$ $\frac{9}{2}^+[624\uparrow]_n$
16^+	3547	20.3(6) ns	$\frac{9}{2}^+[624\uparrow]_n$ $\frac{7}{2}^-[514\downarrow]_n$ $\frac{7}{2}^+[404\downarrow]_p$ $\frac{9}{2}^-[514\uparrow]_p$
2-g.p.			
8^{-b}	1529	5.2(2) msec[a]	$\frac{9}{22}^+[624\uparrow]_n$ $\frac{7}{2}^-[514\downarrow]_n$
5^-	1640	19.2(3) ns[a]	$\frac{9}{2}^+[624\uparrow]_n$ $\frac{1}{2}^-[521\downarrow]_n$[c]
2^{-b}	1006	7.4(4) ns[a]	$\frac{9}{2}^-[514\uparrow]_p$ $\frac{5}{2}^+[402\uparrow]_p$[c] + octupole vibration + neutron character?

a. Halflives taken from References [Bu66],[Ma79], and [Go67].

b. Isomers known previously.

REFERENCES

REFERENCES

[Ab53] A. Abragam and R. V. Pound, Phys. Rev. 92, 943 (1953).

[Al64] P. Alexander, F. Boehm, and E. Kankeleit, Phys. Rev. B, 133, 284 (1964)

[Ar54] A. Arima and H. Horie, Prog. Theor. Phys. 12, 623 (1954).

[Ba57] J. Bardeen, L. N. Cooper, and J. R. Schrieffer, Phys. Rev. 106, 162 (1957).

[Be68] G. F. Bertsch, Phys. Lett. 28B, 302 (1968).

[Be70] Bertchat, Phys. Rev. Lett. 25, 102 (1970).

[Be74] F. M. Bernthal, J. S. Boyno, T. L. Khoo, and R. A. Warner, Phys. Rev. Lett. 33, 1313 (1974).

[Be75] F. M. Bernthal and R. A. Warner, Phys. Rev. C 11, 11 (1975).

[Be76] F. M. Bernthal, C. L. Dors, B. D. Jeltema, T. L. Khoo, and R. A. Warner, Phys. Lett. 64B, 147 (1976).

[Bl52] Blatt and Weisskopf, Theoretical Nuclear Physics, Wiley.

[Bo76] F. W. N. deBoer, et al., Nucl. Phys. A263, 397 (1976).

[Br77] J. Bron, W. H. A. Hesselink, H. Bedet, A. Verheul, and G. Vanden Berghe, Nucl. Phys. A279, 365 (1977).

[Bu66] J. Burde, R. M. Diamond, and F. S. Stephens, Nucl. Phys. 85, 481 (1966).

[Ch68] J. Christiansen, H. E. Mahnke, E. Recknagel, D. Riegel, G. Schatz, G. Weyer and W. Witthuhn, Phys. Rev. C 1, 613 (1970).

[Do78] Private communication. C. L. Dors and P. J. Daly, et al.

[Do79] C. L. Dors, F. M. Bernthal, T. L. Khoo, C. H. King, J. Borggreen, and G. Sletten, Nucl. Phys. A314, 61 (1979).

[FITB] S. R. Faber, Computer program for determining half-lives from timing data, unpublished.

[Ga69] H. Gabriel, Phys. Rev. 181, 506 (1969).

[Ga75] A. K. Gaigalas, R. F. Shroy, G. Schatz, and D. B. Fossan, Phys. Rev. Lett. 35, 55 (1975).

[Ge77] R. J. Gehrke, R. G. Helmer, and R. C. Greenwood, Nucl. Inst. Meth. 147, 405 (1977).

[Go67] P. F. A. Goudsmit, J. Konijn, and F. W. N. deBoer, Nucl. Phys. A104, 497 (1967).

[Gr66] R. Graetzer, G.B.Hagemann, K. A. Hagemann and B. Elbek, Nucl. Phys. 76, 1 (1966).

[Gu71] C. Günther, P. Kleinkeinz, R. F. Casten, and B. Elbek, Nucl. Phys. A172, 273 (1971).

[Ha68] B. Harmatz and T. H. Handley, Nucl. Phys. A121, 481 (1968).

[He68] R. G. Helmer and C. W. Reich, Nucl. Phys. A114, 649 (1968).

[He77] H. Helppi, S. K. Saha, P. J. Daly, S. R. Faber, T. L. Khoo, and F. M. Bernthal, Physics Letts. 67B, 279 (1977).

[Ho59] W. M. Hooke, Phys. Rev. 115, 453 (1959).

[Ho67] H. J. Hofstetter and P. J. Daly, Phys. Rev. 159, 1000 (1967).

[Je77] B. D. Jeltema, F. M. Bernthal, T. L. Khoo, and C. L. Dors, Nucl. Phys. A280, 21 (1977).

[Ke78] T. J. Ketel, E. A. Z. M. Vervaet, and H. Verheul, Z. Physik, A285, 177 (1978).

[Kh73] T. L. Khoo, J. C. Waddington, and M. W. Johns, Canadian J. of Phys., 51, 2307 (1973).

[Kh75] T. L. Khoo, F. M. Bernthal, R. A. Warner, G. F. Bertch, and G. Hamilton, Phys. Rev. Lett. 35, 1256 (1975).

[Kh77] T. L. Khoo and G. Lovhoiden, Phys. Lett. 67B, 271 (1977).

[KKRE] C. B. Morgan - computer program for sorting coinc. data (special version).

[Kl65] D. Klerk, High Field Electromagnets, 1965.

[Ko71] J. Konijn, B. J. Meijer, and G. Van Middelkoop, Phys. Lett. 35B, 567 (1971).

[Ko79] J. Konijn, T. J. Ketel, and H. Verhuel, Zeitschrift fur Physik A289, 287 (1979).

[La65] N. L. Lark and H. Morinaga, Nucl. Phys. 63, 466 (1965).

[Le68] C. M. Lederer, J. M. Hollander, and I. Perlman, Table of the Isotopes, John Wiley & Sons.

[LEY] L. E. Young, Ph.D. Thesis, 1975, State University of New York at Stony Brook.

[Ma50] M. G. Mayer, Phys. Rev. 78, 16 (1950).

[Ma79] L. G. Mann, J. B. Carlson, R. G. Lanier, G. L. Struble, W. M. Buckley, D. W. Heikkinen, I. D. Proctor, and R. K. Sheline, Phys. Rev. C 19, 1191 (1979).

[Mi56] H. Miyazawa, Phys. Rev. 101, 1564 (1956).

[Mi64] A. B. Migdal, Nucl. Phys. 57, 29 (1964).

[Mo60] B. R. Mottelson and J. G. Valatin, Phys. Rev. Lett. 5, 511 (1960).

[Mo76] H. Morinaga and T. Yamazaki, In Beam Gamma Ray Spectroscopy, North-Holland Publ. 1976.

[Na72] K. Nakai, B. Herskind, J. Blomquist, A. Filevich, K. G. Rensfelt, J. Sztarkier, I. Bergstrom, and S. Nagamiya, Nucl. Phys. A189, 526 (1972).

[Na73] S. Nagamiya, O. Hashimoto, and Y. Yamazaki, Physica Scripta 8, 95 (1973).

[Na74] S. Nagamiya, Nucl. Inst. Meth. 114, 349 (1974).

[Ni55] S. G. Nilsson, Mat. Fys. Medd. Dan. Vid. Selsk. 29 No. 16 (1955).

[Ni69] S. G. Nilsson, et al., Nucl. Phys. A131, 1 (1969).

[Ni71] V. A. Nicely, J. Chem. Ed. 48, 443 (1971).

[No58] H. Noya, A. Arima, and H. Horie, Suppl. Prog. Theor. Phys. 8, 33 (1958).

[Og71] W. Ogle, S. Wahlborn, R. Piepenbring, and S. Fredriksson, Rev. Nucl. Phys. 43, 424 (1971).

[Pi75] M. Piiparnen, J. C. Cunnane, P. J. Daly, C. L. Dors, F. M. Bernthal and T. L. Khoo, Phys. Rev. Lett. 17, 1110 (1975).

[Qu69] D. Quitmann and J. Jaklevic, Laurence Radiation Lab. Report UCRL-18958 (1969).

[Ro69] J. T. Routti, and S. G. Prussin, Nucl. Inst. Meth. 72, 125 (1969).

[Ro77] C. Roulet, G. Albouy, G. Auger, J. M. Lagrange, M. Pautrat, K. G. Rensfelt, H. Richel, H. Sergolle and J. Vanhorenbeeck, Nucl. Phys. A285, 156 (1977).

[Sa63] S. Salomon, L. Bostrom, T. Lindqvist, E. Matthias, and M. Perez, Nucl. Phys. 46, 377 (1963).

[Sa77] S. K. Saha, H. Helppi, P. J. Daly, S. R. Faber, T. L. Khoo, and F. M. Bernthal, Phys. Rev. C 16, 2159 (1977).

[Sc37] T. Schmidt, Z. Physik 106, 358 (1937).

[Sh77] R. E. Shroy, A. K. Gaigalas, G. Schatz, D. B. Fossan Int. Conf. on Hyperfine Interactions, Madison, N. J. (R. S. Raghaven and D. E. Murnick, 1977, p. 37).

[Sh79] R. E. Shroy, A. K. Gaigalas, G. Schatz, D. B. Fossan, Phys. Rev. C 19, 1324 (1979).

[Si68] K. Siegbahn, Alpha, Beta and Gamma Ray Spectroscopy, 1968 North-Holland Publ.

[Sl72] G. Sletten, Nucl. Instr. Meth. 102, 459 (1972).

[St65] P. H. Stelson and L. Grodzins, Nucl. Data 1, 21 (1965).

[St72] F. S. Stephens and R. S. Simon, Nucl. Phys. A183, 257 (1972).

[Va71] Vanden Berghe and K. Heyde, Nucl. Phys. A163, 478 (1971).

[Wa79] P. M. Walker, S. R. Faber, W. H. Bentley, R. M. Ronningen, R. B. Firestone and F. M. Bernthal, Phys. Lett. 86B, 9 (1979).

[WALK] P. M. Walker, Ph.D. Thesis, Canberra, Australia ACT 2600.

[Ya70] T. Yamazaki, T. Nomura, S. Nagamiya, and T. Katou Phys. Rev. Lett. 25, 547 (1970).

[Yo75] L. E. Young, S. K. Bhattacherjee, R. Brenn, B. A. Brown, D. B. Fossan, and G. D. Sprouse, Phys. Rev. C 12, 1242 (1975).

[Zi73] K. Zioutas, B. Wolbeck and B. Perscheid, Zeitschrift fur Physik, 262, 413 (1973).

APPENDIX

APPENDIX

A. Notes on Data Acquisition Programs

1. TOOTSIE

TOOTSIE is a program for the Σ-7 computer designed primarily for taking spectrograph data. It enables one to display E vs. ΔE for example and set non-linear bands around groups of counts in the 2-D spectrum. It then can accumulate 1-D spectra corresponding to these bands.

This program can be used to take γ-ray timing data by setting straight line gates on the vertical (time) axis and accumulating up to 10 time sliced 2048 channel γ-ray spectra. To take g-factor data one can make the vertical axis γ-energy, set gates on it and collect time spectra, but the visual resolution (on the screen) for the vertical axis is only 256 channels.

A typical g-factor configuration would use this initial command

```
DEFINE,EDE,WX,256x64,1024,10,2048
```

The EDE is the operating configuration, WX refers to

the ADC's used W(time) horizontal, X(energy) vertical, 256x64 in the 2-D array size (256 vertical), 1024 is the size of the 1-D spectra, 10 refers to the number of bands to be set, and 2048 is the conversion gain of the XADC.

A little known feature of this program makes it possible to set accurate gates on a 2K or greater γ-spectrum. The program retains the resolution equal to the conversion gain specified in the original command. To set bands one must then expand the whole screen to one channel, divide it into say 8 equal parts and set bands surrounding these drawn in lines. A band set surrounding the 3rd line drawn between a full scale expansion between channel 100 and 101 will contain channel 803 in the 2K ADC space.

2. IIEVENT

This program records up to 4 parameter coincidence data on magnetic tape event by event. KKRECOVERY is the program of choice to sort the data quickly but has the limitation of a fixed gate on the first ADC. IIEVENT RECOVERY does not have this limitation but is slower. CDRECOVERY is a special version of KKRECOVERY that sorts with the last ADC as the fixed gate (but otherwise the same). Another special version that sorts four parameter data exists in ABS form (the source is lost), the first and last ADC's being fixed (the last having no background subtract).

B. Notes on Resolving the 125 keV and 158 keV Half Lives

Figure 8-8 shows the resolving of the 125, and 158 keV transitions half lives into three components. The first data point represents a band set starting in the middle of the prompt peak. Its purpose was to indicate the presence of a prompt component and is not expected to contain all the counts associated with that time bin due to the spread of the TAC prompt peak and for that reason is left out of the fits. It is seen that the 158 transition contains little or no prompt component but the 125 keV line does have some since the first point is relatively higher than in the 158 keV case. This is expected due to some contribution from the prompt 125 keV line in the K = 5 band.

The data for the 125 keV transition was fit with the least squares program KINFIT to a complex decay function (Equation 35) incorporating the 20.3 nsec half life (determined from the 158 keV data with the same program) and the initial population ratios (determined from the peak area ratios from the summed timing data) as fixed parameters and solving for the short half life component plus an added exponential containing the third long lived component. The evidence for the existence of an unknown longer-lived component was strengthened by including another data point not shown on the figure (Figure 8-8) that represented a wide band set on the late part of the time spectrum. This last point was corrected for unequal time band width in the program.

C. Some Interesting Coincidence Gates from the 49 MeV Prompt Coincidence Experiment

180W PR 125 KEV GATE
COUNTS
CHANNEL
0
100
200
300
400
500
600
700
800
900
1000
1100
1200
500
1000
1500
2000
158
147
B.S.
215
257
284
323
340
355
455
902

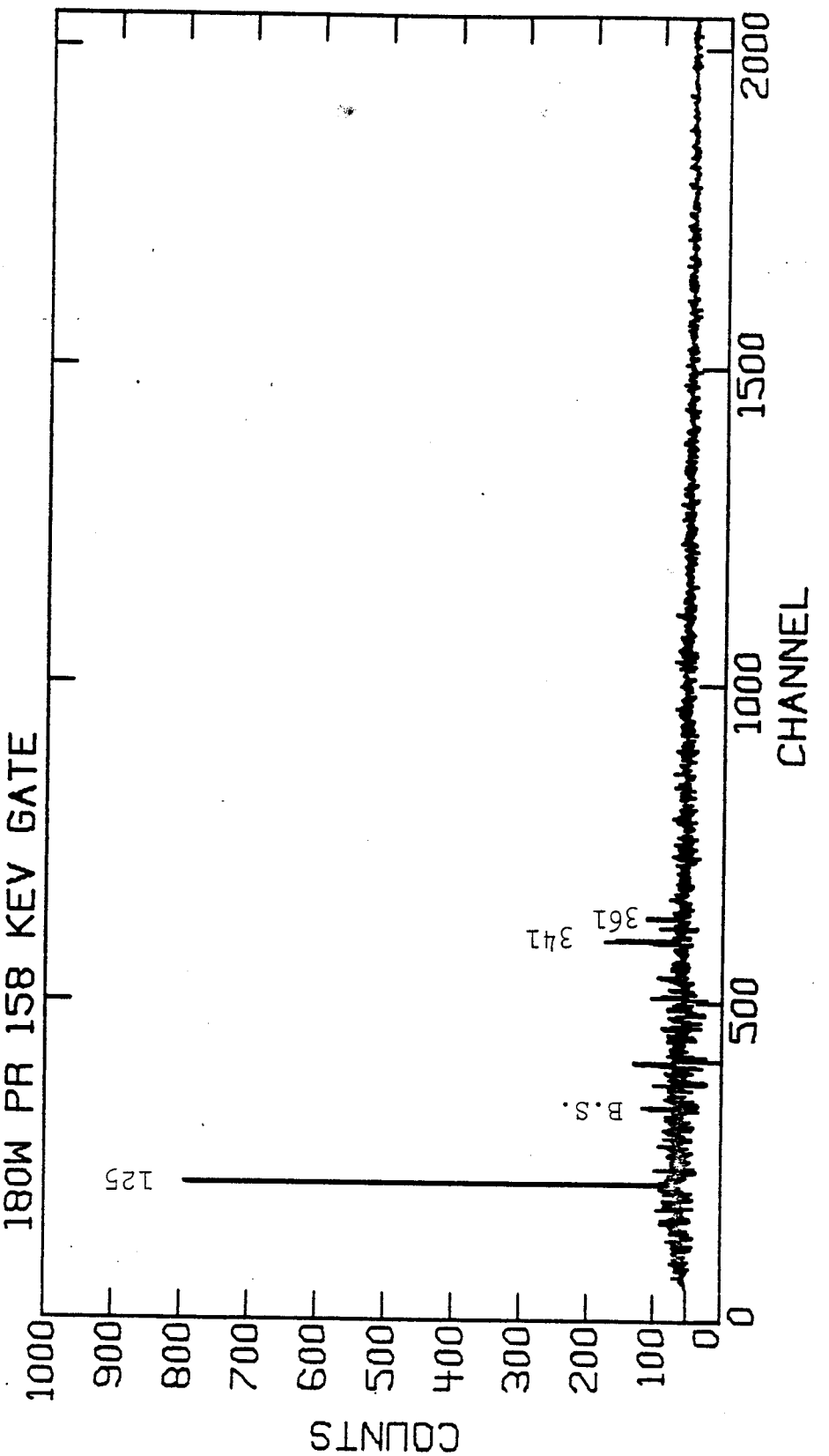
180W PR 158 KEV GATE
COUNTS
CHANNEL
125
B.S.
341
361
0
100
200
300
400
500
600
700
800
900
1000
500
1000
1500
2000

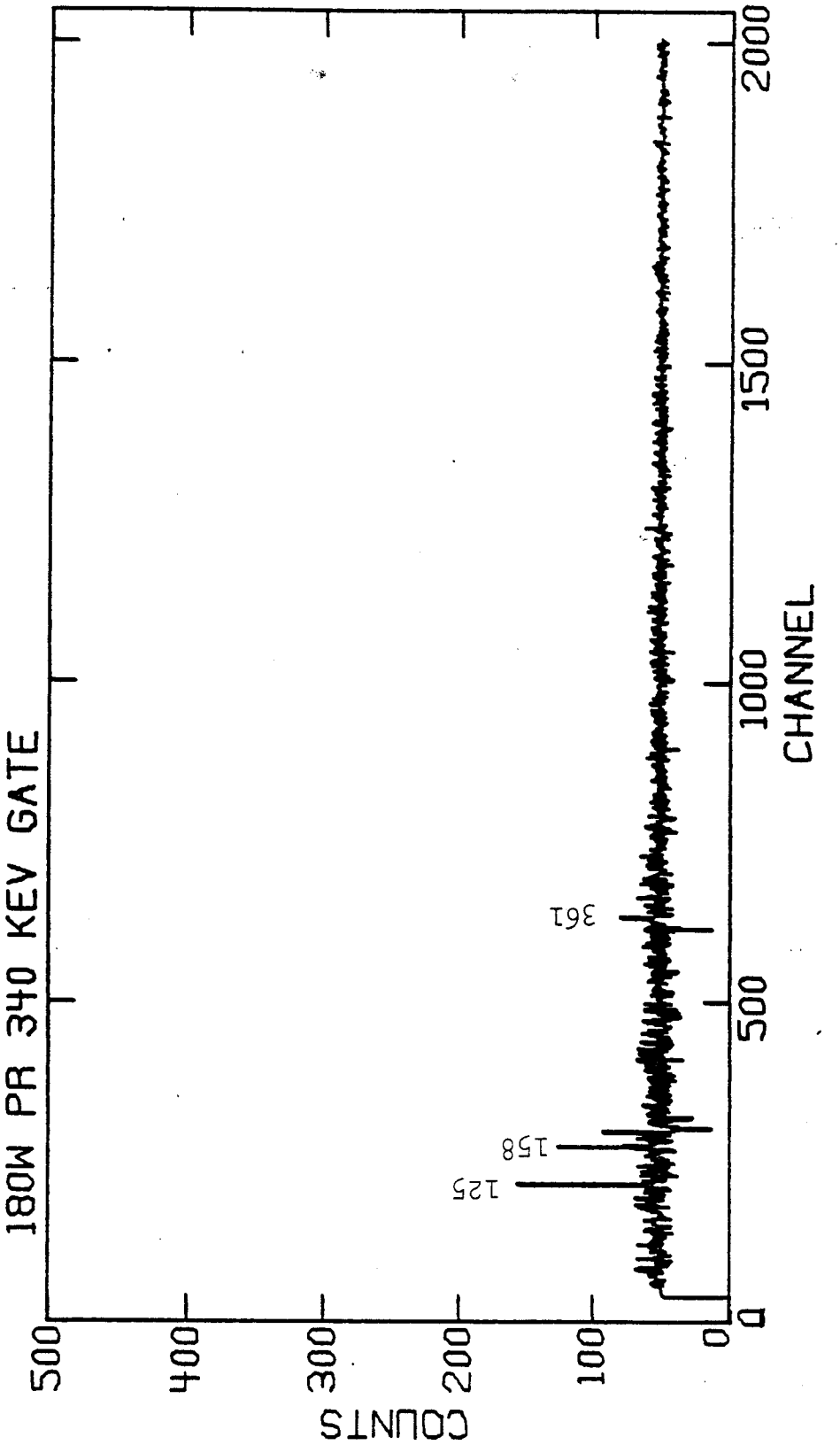
180W PR 340 KEV GATE
COUNTS
CHANNEL
0
100
200
300
400
500
0
500
1000
1500
2000
361
158
125

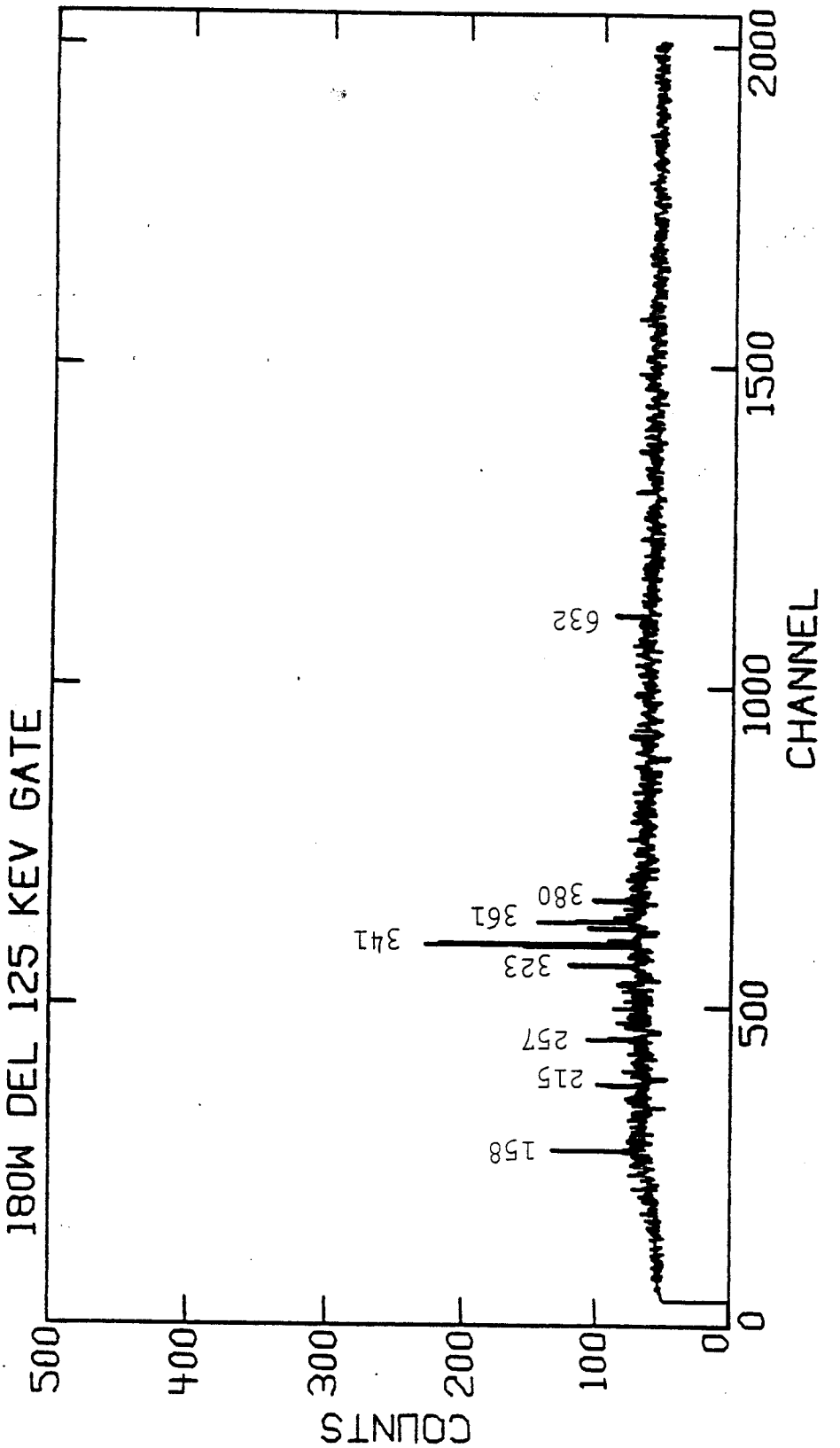
180W DEL 125 KEV GATE
COUNTS
CHANNEL
0
100
200
300
400
500
500
1000
1500
2000
158
215
257
323
341
361
380
632

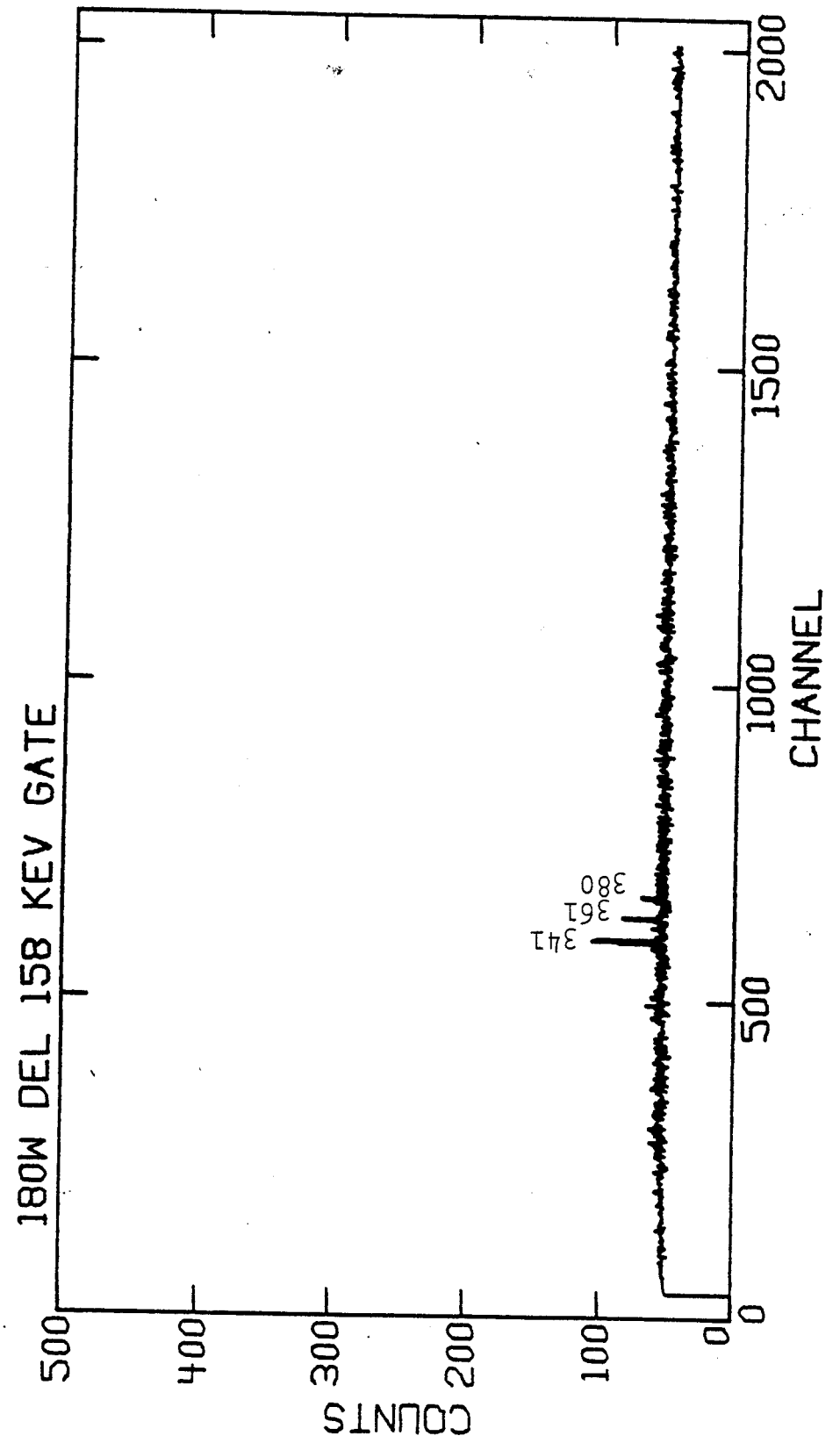
180W DEL 158 KEV GATE
COUNTS
CHANNEL
500
400
300
200
100
0
0
500
1000
1500
2000
341
361
380